Journal of Materials Science & Technology 52 (2020) 29–62

Contents lists available at ScienceDirect

Journal of Materials Science & Technology

journal homepage: www.jmst.org

Invited Review

Recent progresses on designing and manufacturing of bulk refractory alloys with high performances based on controlling interfaces

T. Zhang[a,*], H.W. Deng[b], Z.M. Xie[b,*], R. Liu[b], J.F. Yang[b], C.S. Liu[b], X.P. Wang[b], Q.F. Fang[b], Y. Xiong[c]

[a] School of Physics and Electronic Engineering, Guangzhou University, GuangZhou 510006, China
[b] Key Laboratory of Materials Physics, Institute of Solid State Physics, Chinese Academy of Sciences, Hefei 230031, China
[c] State Key Laboratory of Environment Friendly Energy Materials, West South University of Sciences and Technology, MianYang 621010, China

ARTICLE INFO

Article history:
Received 20 December 2019
Received in revised form 1 February 2020
Accepted 4 February 2020
Available online 25 April 2020

Keywords:
Interface controlling
Designing and manufacturing
Refractory alloys
Structure and performance

ABSTRACT

Refractory alloys such as tungsten and molybdenum based alloys with high strength, thermal/electrical conductivity, low coefficient of thermal expansion and excellent creep resistances are highly desirable for applications in nuclear facilities, critical components in aerospace and defense components. However, the serious embrittlement limits the engineering usability of some refractory alloys. A lot of research results indicate that the performances of refractory alloys are closely related to the physical/chemical status, such as the interface dimension, interface type, interface composition of their grain boundaries (GBs), phase boundaries (PBs) and other interface features.

This paper reviewed the recent progress of simulations and experiments on interface design strategies that achieve high performance refractory alloys. These strategies include GB interface purifying/strengthening, PB interface strengthening and PB/GB synergistic strengthening. Great details are provided on the design/fabrication strategy such as GB interface controlling, PB interface controlling and synergistic control of multi-scaled interfaces. The corresponding performances such as the mechanical property, thermal conductivity, thermal load resistance, thermal stability, irradiation resistance, and oxidation resistance are reviewed in the aspect to the effect of interfaces. In addition, the relationships between these interfaces and material properties are discussed. Finally, future developments and potential new research directions for refractory alloys are proposed.

Contents

* Corresponding authors.
E-mail addresses: zhangtao@gzhu.edu.cn (T. Zhang), zmxie@issp.ac.cn (Z.M. Xie).

https://doi.org/10.1016/j.jmst.2020.02.046
1005-0302/

1. Introduction

Refractory metals and alloys, here targeting tungsten (W), molybdenum (Mo), niobium (Nb), tantalum (Ta), vanadium (V) and their alloys, with the melting temperature above 2000 °C are candidates for applications in aerospace, cladding and structural materials for fission reactors, and first wall blanket and divertor materials for fusion reactors. These refractory metals have high melting temperatures, superior high-temperature strength and especially high void swelling resistance and good thermal creep resistance [1–5]. However, the serious embrittlement and instability in several regimes, i.e., low-temperature embrittlement, recrystallization embrittlement and radiation embrittlement, as well as the poor oxidation resistance at moderate temperatures, limit the usability of above mentioned refractory metals for engineering applications [6–11].

Over recent years, numerous researches have been done to improve the strength and ductility of refractory alloys. As we know that the incorporation of structural defects into crystalline lattices provides an effective approach to the control of metal characteristics. The interfaces including the grain boundary (GB) interface, phase boundary (PB) interface, contact interface and surface are also a kind of defects. The physical and chemical status of these interfaces play a very important role in determining the performance of materials [12–23]. Because interfaces are very important for properties as mentioned above, out of the various possible defects like point defects and dislocations, interfaces attract much more attentions. As the structural units such as grains or phase domains etc., the shrink in dimension to nanoscale, the number density of interfaces increases and their influences could be amplified to the point that some material properties are essentially determined by the nature of interfaces [21,22]. For example, the strength of metals with nanometer-sized grains can be an order of magnitude higher than that of their coarse-grained counterparts, owing to the extremely high density of GBs [24,25]. But at the same time, the increased number density of GBs will enhance the interface scattering of electrons and thus decrease the electrical conductivity [16]. In addition, for nuclear application, the performances such as irradiation resistance, hydrogen retention, thermal stability, etc., are closely related to the interface status [26–32]. For example, interfaces can improve the irradiation resistance by absorbing and annihilating irradiation induced defects, but on the other hand they increase the hydrogen retention [33–36]. Therefore, interfaces play a very important role in determining the properties of metals. In practice, we could decorate the interface to make the best use of advantages and bypass the disadvantages.

Since the physical properties of materials are to a great extent controlled by their internal interfaces, including GBs, PBs, twin boundaries and lamella boundaries [37]. Therefore, recently, several approaches are developed to construct interfaces to modulate material performances such as strength, ductility, fracture toughness, irradiation resistance, corrosion resistance and thermal load resistance of refractory alloys. These approaches include i) strengthening GB interface by alloying with other alloying elements [38–43], producing twin boundaries and low-angle or high-angle GB interfaces [37,44–46], as shown in Fig. 1a, ii) increasing number density of GB interface by refining grains [46–49], iii) constructing nanosized PBs with coherent or incoherent interfaces by adding nanosized oxide/carbide particles which have different combining strength with the matrix, as shown in Fig. 1b and c [37,50–57] and iv) building multi-layer immiscible nano phase boundary interfaces by up-down or bottom-up methods and so on, as shown in Fig. 1d [58–65]. There is no doubt that these strategies significantly improved the performance of refractory metals and alloys, suggesting that internal interfaces can be designed to produce superior performances. Additionally, the external interface such as the surface also affects the properties of materials.

In this review, we discuss the recent developments in the improving performances of refractory alloys by means of interfacial architectures. Several interfaces in refractory alloys are analyzed to identify the effects of their quantity, structure and distribution on the global performance of materials.

2. Grain boundary interface controlling

As well known that tungsten and molybdenum are brittle at low temperatures because of two primary factors: the shortage of dislocation slip planes and the poor cohesion of GB interfaces [66]. The former is a typical feature in the body-centered cubic (BCC) metals and alloys. As a typical BCC metal, the plastic deformation of tungsten or molybdenum depends on the mobility of non-planar ½<111> screw dislocations [67]. The dislocation cores spread into three {110} planes with the <111> zone and leads to a very high Peierls stress [68,69]. Thus the spread of a ½<111> dislocation core makes a three-dimensional structure which is hard to move [70]. This basic factor in tungsten and molybdenum is the main reason for their brittle behavior [66]. In addition to the shortage of operable slip planes, tungsten also suffers from poor GB cohesion. Intergranular fracture has been shown as the most prominent failure mode of tungsten and molybdenum [66]. Up to 95.9 % of fracture surfaces are intergranular in pure tungsten samples [69]. It is understood that non-metallic impurities (e.g. N, O, P) segregating at the GBs would reduce their cohesion [72–74], resulting in a raising brittlement and a high ductile to brittle transition temperature (DBTT), which has been clearly confirmed by the evolution of DBTT with the content of impurities, as shown in Fig. 2a [56,75]. Fig. 2b and c show a detailed information that most of N, O and P impurities distribute at GBs of Mo and W [71,76,77]. The DBTT rapidly increases with increasing O or O/N contents.

Therefore, decreasing the level of segregating impurities at the GBs, more ductile materials can be expected. Impurities like O, P or C generally cover high angle GBs because of their limited solubility in tungsten matrix (lattice). Refining grain size could increase the density of GB interfaces and thus decrease the impurity concentration. Gludovatz et al. [71] found that the shear deformation during severe plastic deformation (SPD) process distributes the impurities at the newly increased high angle GBs and as a result the concentration of impurities per GB interface area were decreased. On the other hand, the oxygen content can be reduced as low as possible by hydrogen reduction during high temperature sintering, but it is still inevitable that the free oxygen exists at GBs. Another effective method is adding some trace nano compounds or alloy elements to absorb free oxygen by forming more stable compounds like oxides [39,54,78–89]. For example, trace ZrH_2 was added into W matrix and stable ZrO_2 nanoparticles located at GBs were formed, which came from the reaction between the dehydrogenized Zr and O during sintering [78,89,90]. Zhang et al. added trace nanosized carbides such as ZrC and HfC nanoparticles into the tungsten matrix to absorb impurities of O and to form stabled Zr(Hf)-C-O particles pining GBs. This method not only significantly eliminate the intergranular embrittlement by reducing O segregation at GBs, but also provides an effective pining effect by the forming nano particles [78–89,91], which achieve an one-stone-two-birds effect: purifying and strengthening the GBs.

Similarly, Saage et al. [39] found that the addition of Zr to Mo-1.5at. %Si alloy could also control the GB interface, resulting in not only refined grain sizes and an extremely high bend strength, but also detectable bending ductility at room temperature. Stress–strain curves of this Mo based alloys tested at room temperature and at 538 °C are presented in Fig. 3 [39]. The Mo-

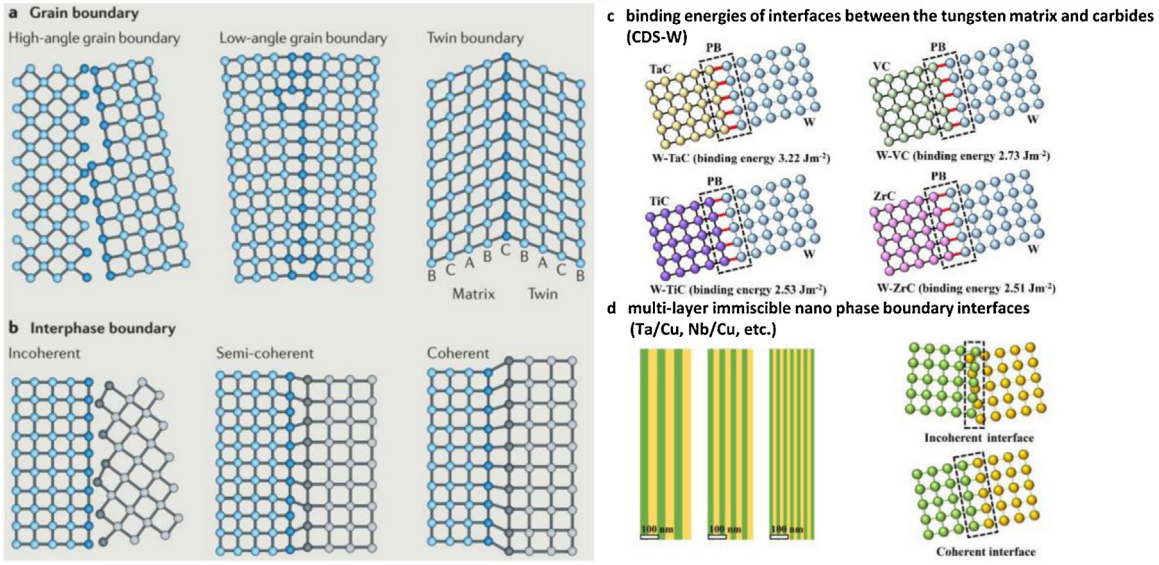

Fig. 1. Sketch of interface structures [37].

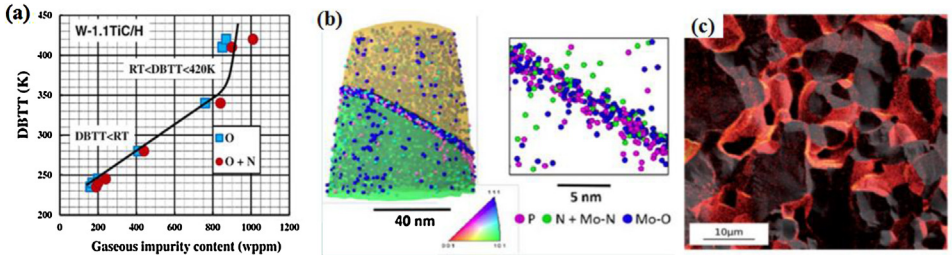

Fig. 2. a) Effects of oxygen and nitrogen impurity contents on DBTT measured by three-point bending at 5×10^{-3} mm s^{-1} for TFGR W-1.1TiC/H with oxygen contents ranging from 160 to 870 wt. ppm [75]; b) APM-reconstruction of a measured atom probe sample with a GB of 45° rotation angle and detailed view on the GB [76]; c) Fracture surface of W_{hipped} with an overlaying O mapping showing O covering most grain boundaries [71].

1.5at. %Si and Mo-1.5at. %Si-Y_2O_3 alloys are brittle at temperatures up to 538 °C. In contrast, the alloy with Zr addition already exhibits detectable plastic strain at room temperature with a very high strength level of about 2 GPa. Zr additions are regarded to be beneficial for the following reasons: i) refining the grains of the Mo based alloy, ii) diminishing detrimental oxygen by forming stable ZrO_2 particles, which in turn helps to pin the GBs, iii) reducing the concentration of Si at the GBs, which is thought to strengthen the GBs [39].

For the issue of the lack of slip planes, alloying W or Mo with rhenium (Re) can increase slip planes and enhance the mobility of dislocations, and meanwhile trap impurities (particularly oxygen) in the lattice, reduce GB segregation and embrittlement and thus improve GB cohesion [17,66]. Alloying W with Re can also lower the Peierls stress, resulting in an effect termed "solid solution softening", which clearly increases the toughness especially at high Re concentrations close to the solubility limitation [43,92]. Even for trace Re addition to tungsten matrix, this solid solution softening process is active and leads to toughening and ductilization [93].

In addition to Re, other transition metals such as Ir, Rh, Ru, and Os might reduce the Peierls barrier [94]. Setyawan et al. conducted a series of computational studies on the effects of transition metals on the interface cohesion of tungsten GBs [95]. As a typical model, a $\Sigma 27 < 110 > \{525\}$ symmetrical tilt GB was employed to calculate the cleavage energy of the GB upon substituting of W atoms at different positions with Rh, Ru, Os, Re or Ir atoms, as shown in Fig. 4. The plotted energy embodying the Griffith ideal cleavage energy with the fracture plane is denoted by a dashed line in Fig. 4b. All elements located at position A or E strengthen the GB, on the contrary weaken at B, C, or D sites. The Os element has the largest strengthening effect. The calculated cleavage energy without impurities was 4160 mJ/m^2. Formation energies could reflect the stability for different transition metals at GBs, which are defined as the energy needed to swap an impurity atom at a bulk position with a W atom at a GB site. Different sites correspond to the different formation energy, the strengthening sites of A and E also correspond to highest formation energies (i.e. the most stable positions) [95]. In addition, the higher the cleavage energy, the more stable the GB site. A stable substitution at GB sites can enhance the intergranular interface cohesion, but at the same time, strong GB segregation should be avoided so that enough alloying atoms can be dissolved in the bulk to reduce the Peierls stress. Especially, segregation at decohesion sites B, C, and D should be avoided [95]. Considering these requirements, Re, Os and Ru are more suitable for improving the intrinsic ductility as well as increasing interfacial cohesion [93]. Moreover, the strengthened GB interface and suppression of diffusion of W atoms by Re addition raise the recrystallization temperature of W–Re alloys [93]. Exceptionally, Ta can increase the cohesion of the $\Sigma 27$ GB when it locates at site D, at which, Ta is energetically stable. At other sites, it is counterproductive and Ta decreases the cohesion. In addition to Ta, other lower-valence solutes, such as Hf, could also increase the cohesion at different sites of GB interfaces [95]. These results emphasize the importance for choosing alloying elements to strengthen W based alloys, which suggest that ternary alloys applying a synergistic effect of lower- (Hf, Ta) and higher- (Re, Os and Ru) valence elements may be better than binary alloys

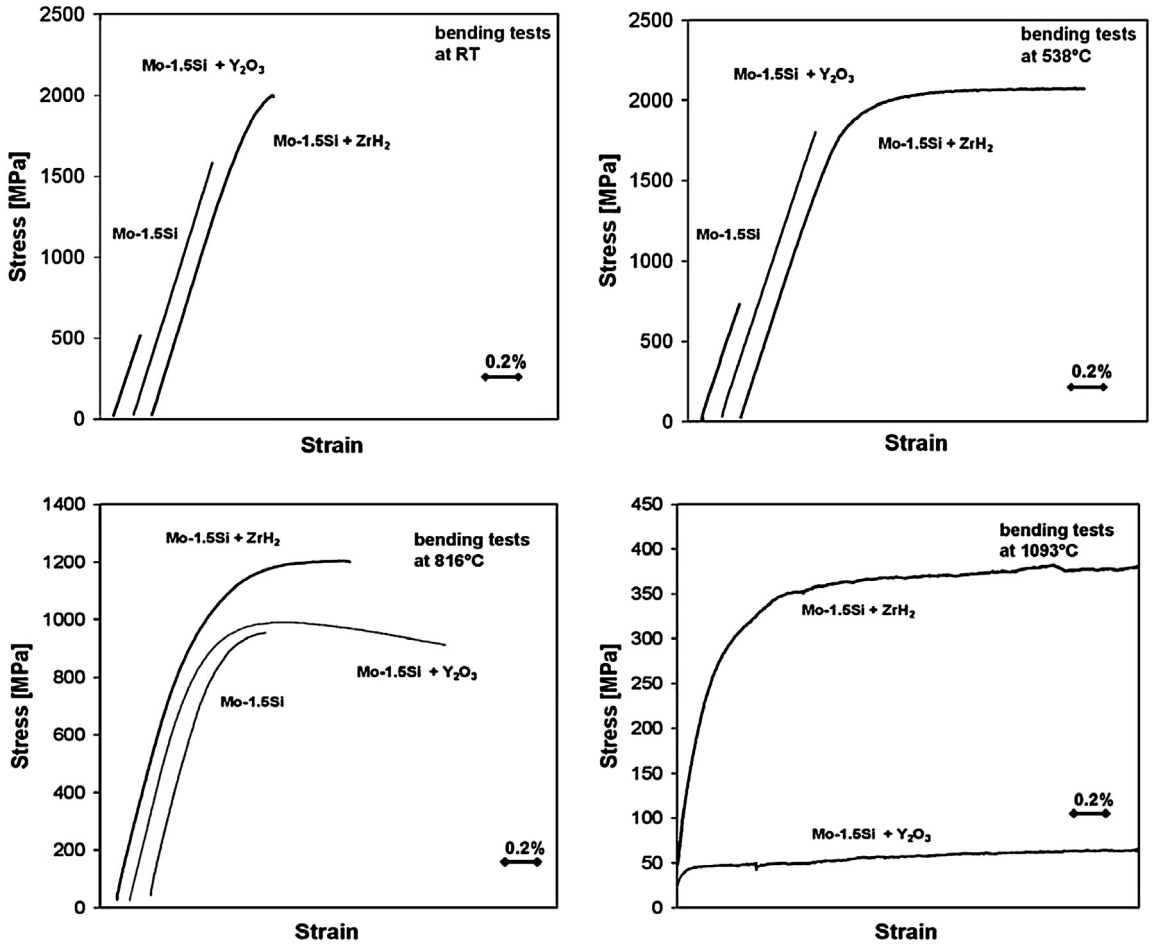

Fig. 3. Stress–strain curves (outer fibre) of pure Mo-1.5Si and Mo-1.5Si with Y_2O_3 and ZrH_2 addition at (a) room temperature and at (b) 538 °C (c) 816 °C and (d) 1093 °C [39].

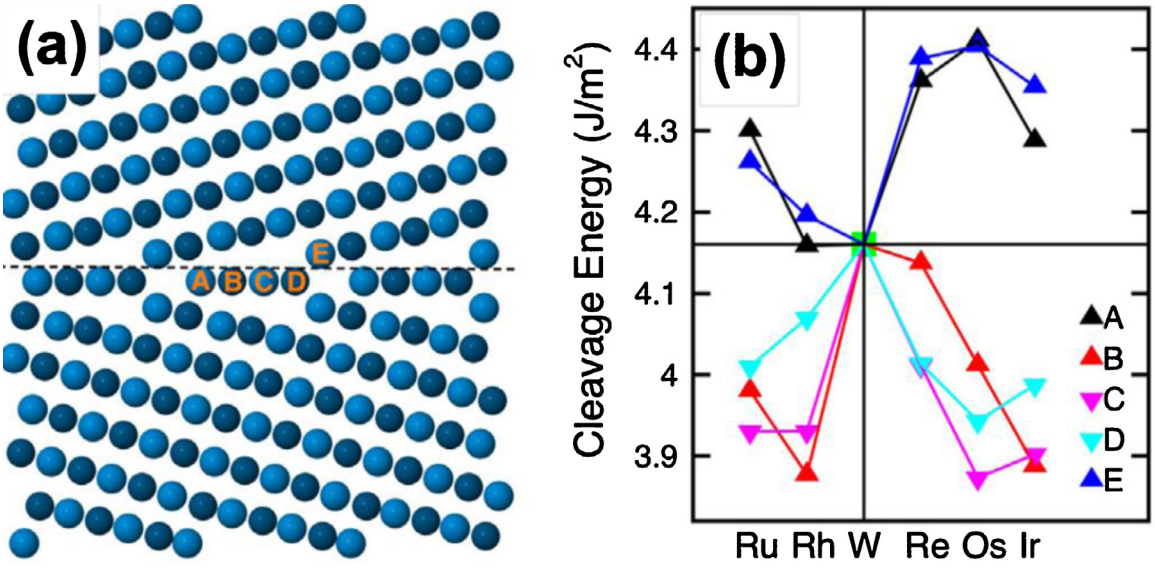

Fig. 4. (a) Model structure of the W Σ27 < 110> {525} general twin GB as viewed from the <110> direction. The dashed line denotes the position of the GB cleavage plane. Different colors represent different coordinates along the <110> direction. (b) Cleavage energy as a function of substitutional elements at different positions [95].

in the aspect of improving ductility by enhancing the GB interface cohesion [93].

Tran et al. [96] investigated the segregation and strengthening/embrittling effects of 29 metallic dopants at the Σ5(310) tilt and Σ5(100) twist Mo GBs by employing density functional theory calculations and empirical continuum models. They found that dopants can be classified into three zones of interest, as shown in Fig. 5. These dopants that have the positive segregation energy

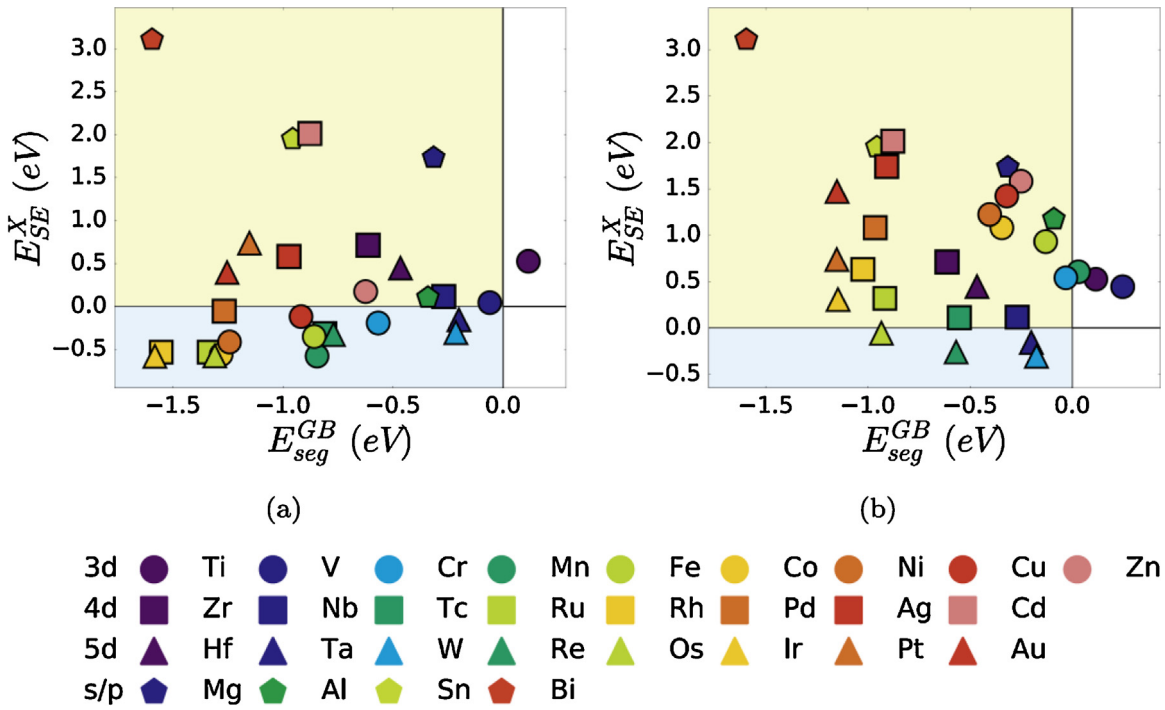

Fig. 5. Plots of the strengthening energy E^X_{SE} versus segregation energy E^X_{seg} for the 29 dopants in the Σ 5(310) tilt GB. (a) based on lowest energy dopant site in GB and free surface (l-to-l approach); (b) based on Site 0 (m-to-s approach). Dopants in the white region (positiveE^X_{seg}) prefer to stay in the bulk. For dopants that segregate, those with negativeE^X_{SE} (blue region) tend to strengthen the GB [96].

E^X_{seg} (white region) would prefer to stay in the bulk, and hence would have no effect on GB strength. For dopants that segregate at GBs, those with negative strengthening energy E^X_{SE} (blue region) tend to strengthen the GB, while those with positive strengthening energy E^X_{SE} (yellow region) tend to decrease the cohesion of GB. The dopant site preference and strain effects have a significant influence on the strengthening energy. Assuming a fast cleavage model for fracture, only Re, Ta, Os and W are predicted to have a weak strengthening effect on Mo for the Σ5(310) tilt GB, and Fe, Mn, Nb and Co are predicted to have reasonable strengthening effects for the Σ5(100) twist GB [96]. These above results indicate that GB interfaces critically affect their mechanical properties by acting as centers of dopant segregation and system stabilization. Therefore, the chemical states of GB interfaces could determine the performance of afore-mentioned refractory materials.

Except for the chemical states, the physical states of the GB interface are also important factors to determine the performance of refractory metals and alloys. It's known that increasing GB interface densities and controlling GB types (i.e. high-angle GB and low-angle GB) are also effective route to modulate the performances of refractory metals. Ultrafine grained (UFG) and Nanocrystalline (NC) metals have been proposed as radiation tolerant materials due to their high density of GB interface areas [97,98]. The GBs have been indicated working act as particularly efficient defect sinks to increase the radiation tolerance [99–101]. Furthermore, recent works have suggested that GBs can facilitate recombination and annihilation of the Frenkel pairs [102]. The use of UFG and NC tungsten with extensive GBs is an effective way to heal helium-induced radiation damage [103]. In addition, GBs in tungsten can trap helium atoms during irradiation [101] and thus reduce the helium accumulation within the grains [104]. Therefore, the interface engineering with increasing the GB density could be a vital tool for enhancing the radiation tolerance. Additionally, increasing GB interface density can also improve mechanical properties, especially the strength according to the Hall-Petch relationship, compared to commercial coarse-grained materials [105,106]. The UFG and NC tungsten materials could be prepared through several severe plastic deformation (SPD) techniques [105–109] and alloying methods [110–112]. Hao et al. [107] used an equal channel angular pressing (ECAP) processing at 800 °C and 950 °C to refine tungsten grains from several ten micrometers to the ultrafine-grained level, and found a simultaneous improvement in both the strength and ductility/toughness: the microhardness increased from about 510 HV in as-received state to about 560 HV after ECAP extrusion and the DBTT decreased from 483 °C to 322 °C after the 950 °C ECAP processing. It was indicated that a number of low-angle GBs consisting of edge dislocations in the specimen after 950 °C extrusion lead to the microstructure and performance optimization [107], as shown in Fig. 6.

Levin et al. [109] fabricated W specimens with elongated microstructures by an equal channel angular extrusion (ECAE) at ~ 300 °C through a 90° angle die. The mechanical behaviors of both unprocessed and processed materials were tested by a three-point bending method at temperatures ranging from 24 °C to 320 °C, as shown in Fig. 7. The results indicate that a single pass of ECAE (strain ~1.15) reduces the flexural toughness of the material and increases the DBTT, while two and four passes significantly increase the flexural toughness compared to that of the referenced material. The flexural toughness of the material after four-pass extrusion (strains exceeding 4.5) is more than 50 times greater than that of the original one at ambient temperature. This is mainly due to elongated GB interfaces that increase the resistance to intergranular fractures, enhance plastic dissipation, and activate relatively high fracture toughness crack systems for transgranular fractures, as presented in Fig. 7a and b. The results indicate that substantially elongated grains formed by deformation processing at a temperature near the DBTT are effective for improving the ambient temperature ductility and toughness of bulk polycrystalline tungsten materials.

In addition to W material, the nanostructured Ta was also fabricated by using ECAE from precursor powders [108]. Consolidation by ECAE was conducted through extruding the encapsulated powder through four extrusion passes by three different routes: A (no

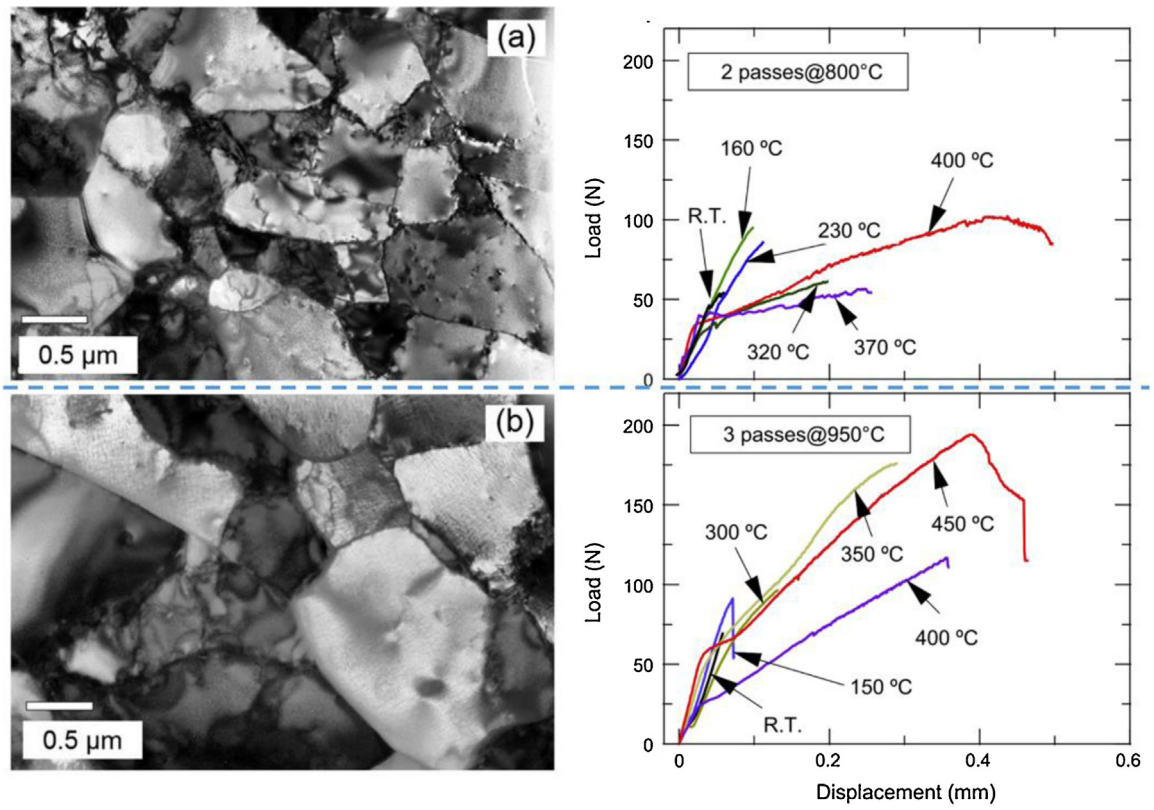

Fig. 6. TEM micrographs of the specimens after two extrusion passes at 800 °C (a) and three extrusion passes at 950 °C (b); The load–displacement curves at different testing temperatures for the ECAP-strained specimens [107].

rotation of the billet between ECAE passes); B (±90° rotation after successive passes); and E (a rotation schedule of 180°, −90°, 180°). The temperature of extrusion was either 900 °C or 1200 °C. Tantalum consolidated through the route 4A (4 passes at 900 °C) exhibits the finest structure with elongated flat features aligned along a direction close to the extrusion direction (ED), as shown in Fig. 8c and d. The structure of the specimens (from route 4B, 4 passes at 900 °C) also has aligned grain regions (prior particles) but they are shorter than those in the route A case and oriented at a modest angle to the horizontal ED. In the route 4E (4 passes at 900 °C) case, the GBs are not elongated as in the route 4A and 4B cases, but having a rough interlocking surface with adjacent grains, as shown in Fig. 8e and f. In addition, these grains are aligned at an angle of ~25–30° along with the extrusion direction for the route 4E case. The microstructure of the route 4A 1200 °C case is similar to that of the 4A 900 °C case with elongated interlocking grains and an aspect ratio, length/width, of ~15. The 4B 900 °C material has a grain aspect ratio of 10, and the 4E 900 °C case possesses the smallest aspect ratio of ~8 [108].

Consolidated Ta by ECAE exhibits a much higher strength (with an UTS from 531 MPa to 618 MPa) than that of as-received wrought materials (178 MPa), while keeping a comparable good ductility (with failure strain from 19 % to 24 %), which indicated that the special GB interface structure in ECAE processed Ta resulted in a greater toughness [108]. The large increase in both strength and toughness of ECAE consolidated Ta comes likely form the complex grain morphologies. These include grain aspect ratio and grain or sub-grain size, which all affect the dislocation mean free path. Crack propagation is hindered by the different substructures in these ECAE consolidated Ta materials. For example, in the case of 4E processed specimens, the special interlocking GB structures effectively prevent cracks from spreading along prior GBs while cause other effective modes of deformation [108]. The different treat technology leads to various interfaces including GB interfaces and defect interfaces, which results in the different mechanical properties of the processed Ta materials.

Another SPD method for fabricating nano grains to increase the GB interface density is the high-pressure torsion (HPT), in which the produced GBs are most of high-angle types in a non-equilibrium and high-energy state [47,105,106]. HPT induced edge dislocations within the grains, combined with a depleted impurity concentration along pre-existing GB interfaces, lead to the enhancement of the ductility in nanocrystalline-W (NC-W) [105]. Under dynamic compression, the specimen exhibits localized shearing followed by cracking and subsequent failure, similar to their UFG counterparts processed by ECAP plus cold rolling. The width of shear bands in the HPT-processed NC-W is much smaller than that of other UFG counterparts [105]. In other words, the extensive nanograins in the NC-W lead to more adiabatic shear properties than that of bulk W with coarse grains, so the NC-W is more suitable for the armor piercing bullet.

Mechanical testing under uniaxial dynamic loading indicated that UFG and NC-W materials exhibit the long-sought-after localized shearing, rather than uniform plastic deformation and/or axial cracking [105,113]. This result highlights that nanoengineering is opening a new area for tungsten, especially for its application in anti-armor kinetic energy penetrators. However, the nanograins in HTP and ECAP materials are elongated, which lead to obvious anisotropy, as shown in Fig. 9. The bright-field TEM micrograph indicates that grains all have the elongated shape. Many grains are heavily dislocated and break-ups of the elongated grains are apparent. In fact, the deformed structures with a high density of dislocations and GBs will lead to the thermal instability. In addition, although these SPD techniques can fabricate high-quality samples for important fundamental studies to gain improved understanding of physical phenomena in these materials, their use on industrial

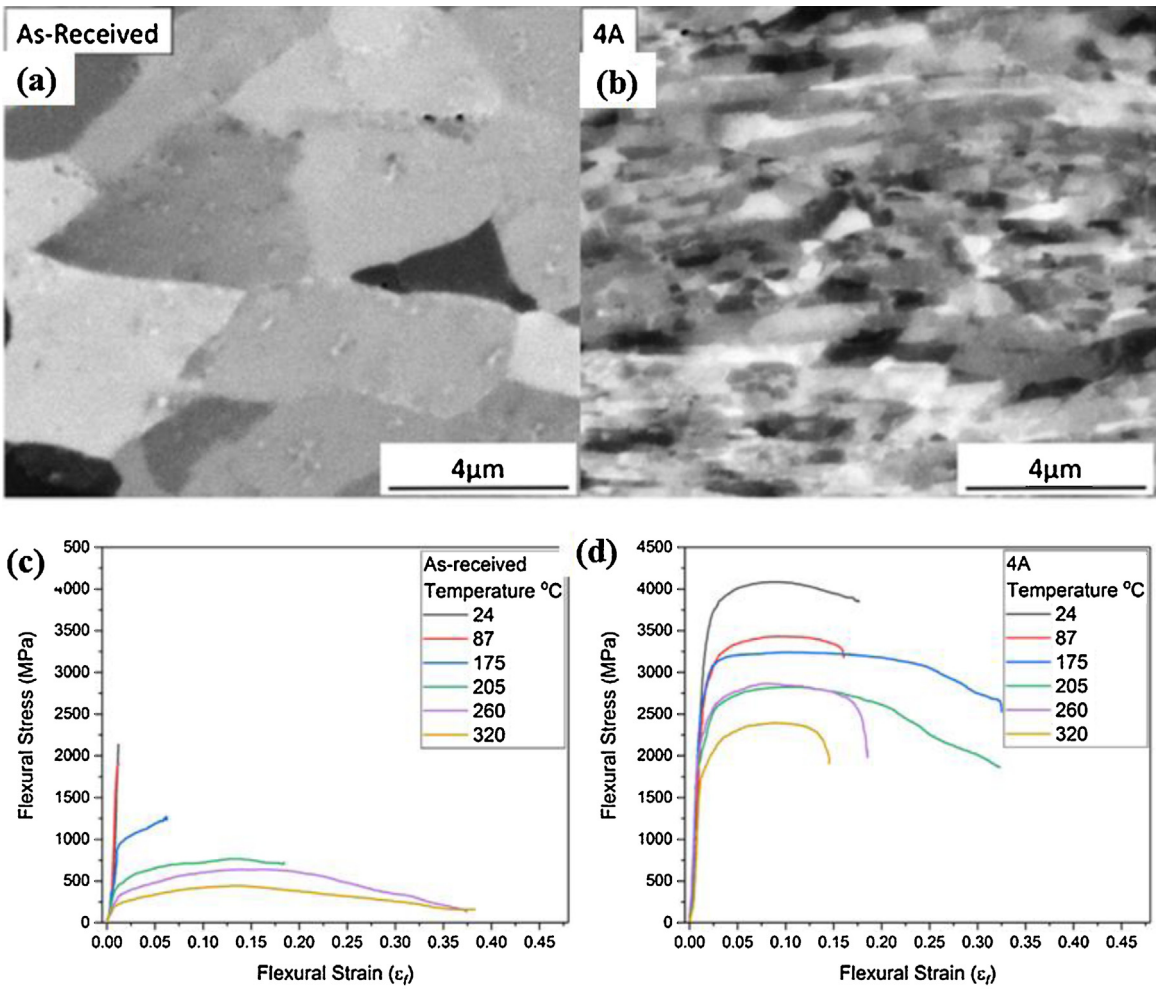

Fig. 7. SEM-BSE images showing the microstructure of the as-received polycrystalline tungsten (a) and ECAE processed (4A) polycrystalline tungsten (b); Flexural stress-strain curves of (c) the as-received and (d) the ECAE processed (4A) polycrystalline tungsten at various test temperatures [109].

scales remains a challenge due to limitations on the achievable throughput using current manufacturing technologies.

Surface mechanical attrition treatment (SMAT) technique also can modulate the GB interface by producing gradient grain size from surface to inside [114,115]. After the SMAT process, nanostructures were obtained in the surface layer of a commercial pure W due to the multi directional repetitive loading and the large strain rate [115]: SMAT induced dense dislocations and dislocation tangles in grains transformed into nanosized sub-boundaries with low-angle GBs and finally to high-angle GBs. The strain range in SMATed W can reach up to a depth of 220 μm from the top surface. As a result, the bending strength of commercial W could be improved from 825 MPa to 1850 MPa by SMAT process. It's indicated that the high density of dislocations in the nanograins lead to the synergetic improvement of ductility and bending strength of tungsten. The residual compressive stresses in the top surface of the W plates with and without SMATed processing are about 881 MPa and 234 MPa, respectively [115]. The improvement of toughness (lower the DBTT) of SMATed W may also be the synergistic effect of the residual compressive stress, improvement of dislocation density and grain size refinement induced by SMAT processing. That's to say, the SMAT processing is a complementary method to further increase the mechanical properties like increasing the strength and decreasing the DBTT value of tungsten-based materials.

All of the above approaches are top-down methods which are often complicated and costive. Hereinafter, the bottom-up strategy will be introduced, which uses powder metallurgy techniques, involving synthesis of nanosized powders followed by a consolidation process. Wei et al. prepared nano crystalline vanadium with an average grain size of 100 nm by high energy ball milling followed by two-step consolidation: i) a room temperature compaction of the as milled powder at a pressure of ~1 GPa for 24 h was conducted, and then ii) hot consolidation was performed by applying a pressure of 850 MPa for 3 h at 600 °C [116]. The mechanical testing results indicate the shear localization was promoted in the nano crystalline vanadium compared to the coarse-grained vanadium [116]. However, because of the high melt temperature (3400 °C) of tungsten, it is tough to prepare nanocrystalline pure tungsten by the powder metallurgy method. Kurishita et al. [8,46,117–120] developed ultrafine grained W-0.5 wt%TiC compacts (hereafter designated as UFGR-WTiC) in a recrystallized state by using mechanical alloying (MA) and hot isostatic pressing (HIP) techniques from the starting powders of W and TiC. There is a key factor for preparing this UFGR-WTiC that high purity raw powders and thorough prevention of contamination of oxygen and nitrogen are needed. During the fabrication, powder treatments were conducted in a well degassed glove box filled with the purified Ar, and then W-0.5TiC were consolidated in a purified H_2 or Ar atmosphere (termed W-0.5TiC-H_2 or W-0.5TiC-Ar, respectively). The W-0.5TiC-H_2 specimens exhibit superplastic behavior at 1973 K, as shown in Fig. 10(a), where the specimen was elongated to ~160 %. And the W-0.5TiC-Ar was fractured abruptly at the elongation of 55 % at 1973 K without necking,

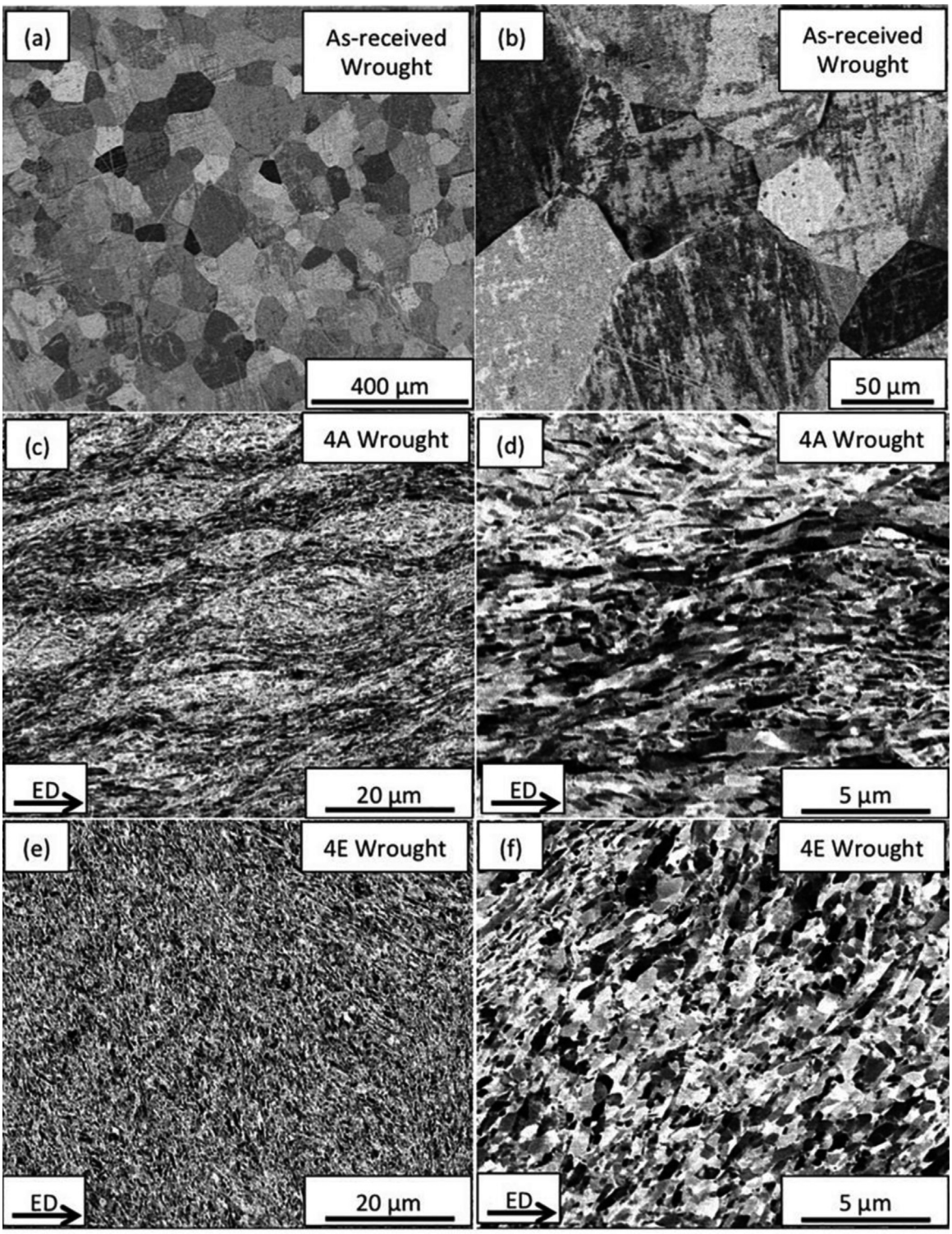

Fig. 8. Back scattered electron SEM images taken on the flow plane of the wrought tantalum: a) as-received low magnification, b) as-received high magnification, c) 4A wrought low magnification, d) 4A wrought high magnification, e) 4E wrought low magnification, f) 4E wrought high magnification. 4A and 4E wrought material processed at room temperature [108].

as shown in Fig. 10(b) [120]. The microstructures of the as-HIPed W-0.5TiC-H_2 and W-0.5TiC-Ar are presented in Fig. 11. Lots of grains have the size larger than 100 nm, beyond the scope of a real nanocrystalline (< 100 nm). The average grain sizes for W-0.5TiC-Ar and W-0.5TiC-H_2 are 69 and 106 nm, respectively [120]. This strategy provides an effective method to fabricate ultrafine grained W alloys, but it does not achieve real nanograined (<100 nm) one.

In 2013, Schuh et al. developed a theoretical framework to design stable nanostructure GB interface in tungsten alloys based on a thermodynamic model [110,121], as shown in Fig. 12. They found that relatively low segregation enthalpy and mixing enthalpy of alloying elements in W matrix would lead to a stable nanostructure in tungsten based binary alloys. The calculation results indicated that the Gibbs free energy of a W-Ti/W-Cr binary alloy

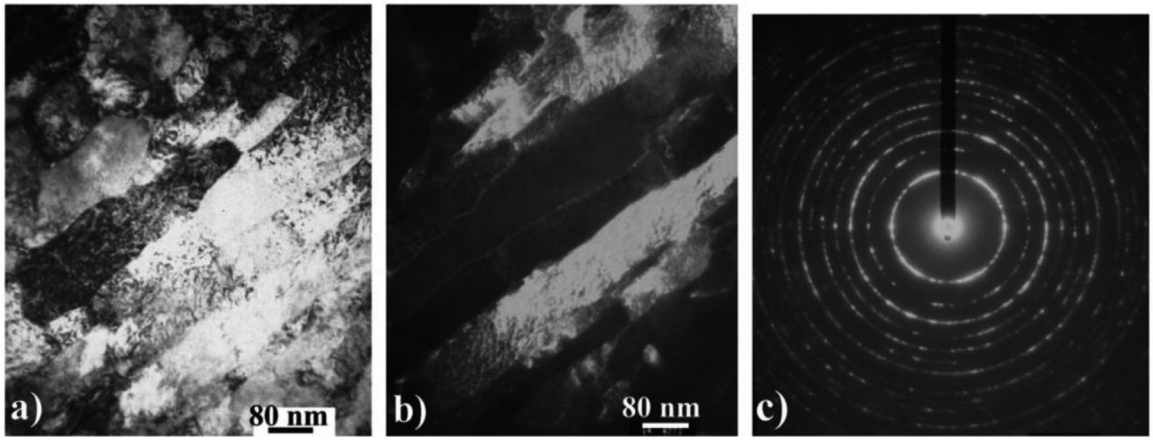

Fig. 9. Bright-field (a), dark-field (b) images and SAED (c) from HPT-W. Notice the high density of defects in the grains, and break-ups in the elongated grains. The SAED shows nearly continuous rings, with no obvious intensity concentration along the rings, indicating large-angle GBs [105].

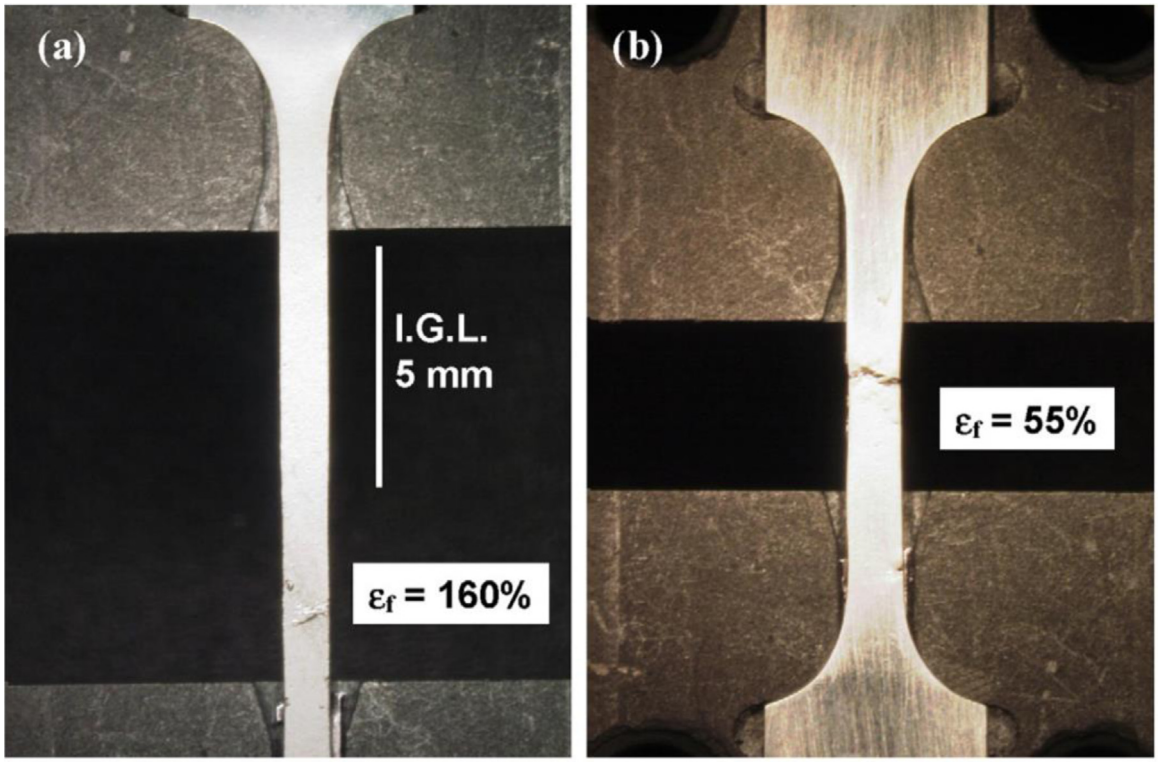

Fig. 10. Tensile specimens of (a) W-0.5TiC-H_2 elongated to approximately 160 % and (b) W-0.5TiC-Ar elongated to approximately 55 % at 1973 K and at the initial strain rate of 5×10^{-4} s^{-1}. For the W-0.5TiC-H_2 the crosshead was arrested on the way of deformation. W-0.5TiC-Ar is elongated uniformly but fractures abruptly at the elongation of 55 % without necking [120].

is very low in several alloying elements, and the nanostructure is presumed to be thermally stable [110,121]. Based on this model, a W-20 at. % Ti alloy powder with an average grain size around 20 nm was produced by high energy ball milling. After one week annealing at 1100 °C, the grain size keeps constant, which demonstrates substantially enhanced stability for the high-temperature and long-duration conditions, as shown in Fig. 12.

Fig. 13 shows that this nanostructured W-Ti alloy processes a heterogeneous chemical distribution: where Ti and W are heterogeneously distributed on the nanoscale with a polycrystalline body-centered cubic structure, with no signatures of any amorphous content [110,121]. However, this stable nanocrystalline W-Ti alloy only appears in the alloyed powder, and not the bulk materials. Although sintering is a common processing method for manufacturing bulk materials, however, the fabrication of bulk nanocrystalline refractory alloys with fully densified compacts is still difficult because full densification often requires a long-time high temperature sintering. During the high temperature process the contact and immigration of GBs would lead to significant grain growth. So, it is a challenge to use enough thermal cycles to remove porosities without also seeing large changes in grain sizes. Encouragingly, this thermodynamic model open a gate to fabricate real nanocrystalline W alloy in large scale.

And then in 2015, based on an accelerated sintering in a nano phase-separating model, Schuh et al. designed a W-Cr alloy and found that the nanoscale Cr-rich phase separation is favorable of accelerating sintering at relative low temperature [122]. They employed a high energy ball technique to prepared W-15 %Cr super

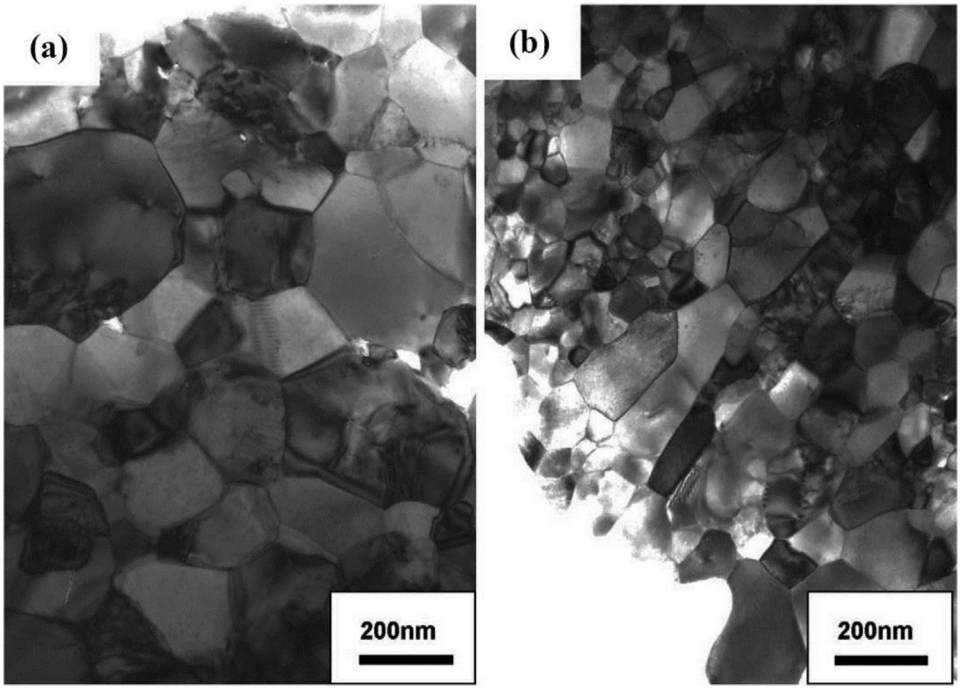

Fig. 11. TEM bright-field images showing grain structures for (a) W-0.5TiC-H_2 and (b) W-0.5TiC-Ar, Size distribution of grains in W-0.5TiC-H_2 and W-0.5TiC-Ar [120].

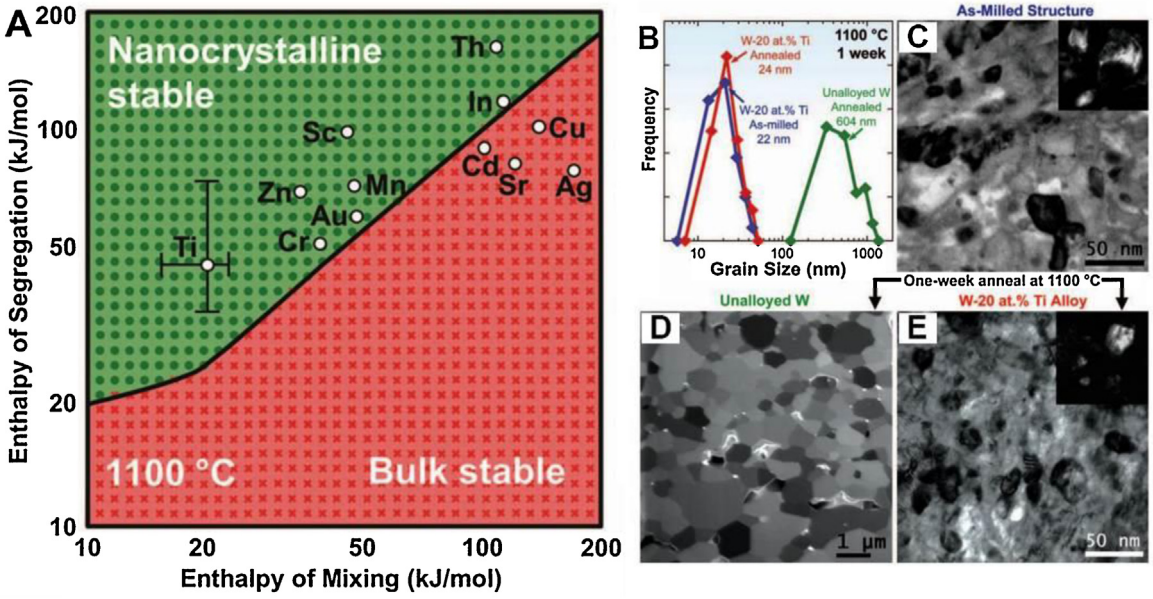

Fig. 12. (A) The nanostructure stability map for tungsten based alloys at 1100 °C. Pre- and post-annealing structures of tungsten powders after one week at 1100 °C. (B) The grain size histograms reveal only a minor change in the W–20 at. % Ti alloy after prolonged annealing and an almost two-orders-of-magnitude coarsening in unalloyed W. (C) The bright-field transmission electron microscopy (TEM) image shows a uniform distribution of nanometer-sized grains in the as-milled structure of the W–20 at. % Ti alloy, with the dark-field TEM image (inset) showing different diffracting crystallites. The post annealing structures vary with alloying: (D) a coarsened grain structure in unalloyed W, presented in a focused ion beam image, and (E) a retained nanocrystalline structure in W–20 at. % Ti, shown in a bright-field TEM image with a dark-field TEM (inset) [110].

saturation alloy powders with an average grain size of 13 nm. This supersaturated solution is thus poised to phase separate on heating. From the as-milled powder, cylindrical compacts were formed by cold uniaxial pressing, and pressureless sintering was conducted. They found that the compact began to noticeably densify (achieving a relatively density of 95 %) at ~950 °C, lower than the ~1100–1200 °C at which liquid phase or conventional activated sintering generally sets on in tungsten, and even lower than the normal sintering onset for pure chromium. Usually, the sintering temperature for pure W is up to 2200 °C without pressure. The rapid sintering in this W–Cr alloy can be attributed to the phase separation, particle surface decoration and interparticle necks, which provide new and more rapid diffusional transport pathways, as shown in Fig. 14, thus sintering may be expected to be accelerated [122,123].

This methodology lends itself naturally to the production of fine-grained materials, for example, W alloy sintering achieves much smaller grain sizes at comparable densities as compared with the other methods. Basing on this accelerating sintering method, Schuh

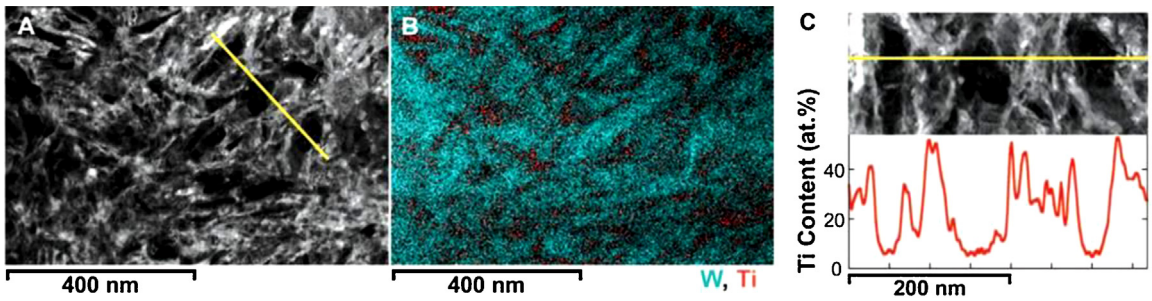

Fig. 13. Chemical analysis of the annealed W-20 at. % Ti alloy. (A) Scanning TEM imaging shows the darker contrast from a heavier element and the brighter contrast from a lighter element. (B) The W-Ti elemental map confirms a nanoscale heterogeneous structure instead of a more homogeneous solute distribution expected from bulk thermodynamics. (C) The Ti compositional line scan across the three larger W-rich regions indicated by the yellow line in (A) further illustrates Ti atoms being depleted at the W-rich grain centers. The entire volume is apparently polycrystalline BCC structure, although with nanoscale composition gradients [110].

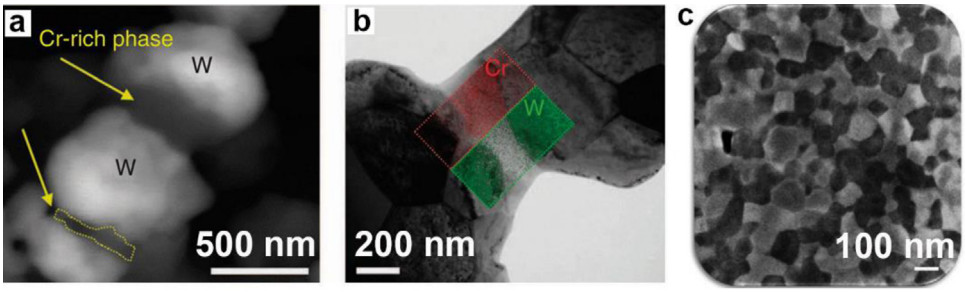

Fig. 14. (a) SEM in backscatter mode reveals a chromium-rich phase forming necks between the compact particles on heating up to 1200 °C (scale bar, 500 nm). (b) A direct visualization of a Cr-rich neck adjacent to W-rich particles is shown in the bright-field TEM image with W and Cr elemental maps (superimposed on the micrograph) using scanning TEM with energy dispersive spectroscopy (STEM-EDS) (scale bar, 200 nm), (c) SEM image of a bulk (6 × 4 mm right cylinder) nanocrystalline W–Ti–Cr alloy shows a grain size of about 100 nm at nearly full density (scale bar, 100 nm) [122].

et al. fabricated W-35Ti-10Cr (at. %) with a nearly full density and an average grain size of 100 nm, as presented in Fig. 14 [122]. In this alloy system, Cr is added to accelerate sintering and Ti is added to promote stabilization of the nano grain structure. However, as shown in Fig. 14, the grain sizes of this bulk W alloy are still near or above 100 nm which is almost beyond the scope of a real nanocrystalline (< 100 nm). The above works provide a possible effective strategy to fabricated nanocrystalline tungsten alloys with both full density and fine grains in a bulk state through a "bottom-up" pressureless sintering of alloy powders.

In order to further increase the GB interface number density in bulk tungsten alloys, basing on the above interface strategy of GB separation and alloying, recently, Wang et al. [124] introduced a promising method with the synergistic effects of solute-drag and second phase nanoparticle pinning in W matrix with trace Ti and Y_2O_3 addition. A high dense nanocrystalline W bulk alloy was prepared via a dissolution-precipitation process by a combination of high-energy ball milling and the subsequent spark plasma sintering. In this bulk W-Ti-Y_2O_3 alloy, the average size of W grains is 67 nm and the average particle sizes in grain interior and at GBs are 8.5 nm and 16.4 nm, respectively. The $Y_2Ti_2O_7$ particles were precipitated during the SPS process, resulting in the refinement of both W grains and dispersed nanosized oxide particles. The Vickers microhardness of this nanostructured W alloy is as high as 1441 HV, which is 2–3 times higher than that of the previously reported ODS-W alloys [124] (see Fig. 15). For example, in bulk ultrafine grained W-Y_2O_3 materials with high relative densities, the Vickers microhardness is about 700 HV [125,126]. The W-1 %Ti-0.5 %Y_2O_3 alloy prepared by SPS has a hardness of 750 HV [127]. Similarly, a bulk W-2 %Ti-1.2 %$Y_2Ti_2O_7$ alloy has a hardness of 780 HV [128]. For the deformed ODS-W materials including the hot rolled W-La_2O_3, W-Y_2O_3 and swaged W-Y_2O_3, the Vickers microhardness is in the range from 500 HV to 600 HV [129]. The extremely high microhardness of the nanostructured W-Ti-Y_2O_3 alloy can be ascribed to the synergistic effect of aboundant GB interfaces and PB interface induced by both nanoscale W grains and uniformly dispersed nanoscale oxide particles. This result indicates that only the GB interface stabilization alone by alloy elements is to some extent not enough to produce a stabled bulk nanocrystalline W alloy, it is still necessary to introduce some other stabilizer interfaces like the PBs. More importantly, if these interfaces are in low energy states, i.e. coherent or semi-coherent PB interfaces, the stabilization would be better.

In addition to the modulation of thermal stability and mechanical properties by GB interface controlling. Some theoretical studies [101,130] have demonstrated the improved radiation resistance of materials with increasing GB interface. Recently, Bai et al. [98] demonstrated the GBs could work as defect sinks: GBs absorb interstitial defects and could then annihilate nearby vacancies by re-emitting the interstitial atoms back into the grain interior. Sefta et al. [130] demonstrate that the introduction of a single GB was shown to result in the trapping of more helium than a single crystal of tungsten. Valles et al. [48] investigated the influence of GB density on helium retention in tungsten by simulating 625 keV He ion irradiation in monocrystalline and nanocrystalline tungsten materials. The result shown that in nanocrystalline one, around 50 % of the incoming He ions are retained at the GBs and the other 50 % in the interior. In the case of larger grains, the amount of He retention at the GBs decreases (~30 %) and increases in the grain interior, revealing a high dependence of GB density on the mechanisms of He retention. The amount and distribution of pure vacancy clusters (V_m) are similar in both the monocrystalline and nanocrystalline tungsten materials. Mixed He_nV_m clusters are concentrated in a small "damaged volume" at about 1000 nm. The size and number density of He atoms inside the mixed He_nV_m clusters is different in the interior of a grain in nanocrystalline and monocrystalline ones. The trend is clear: mixed He_nV_m clusters are larger and their He/V ratio is lower in nanocrystalline. Therefore, mixed He_nV_m clusters

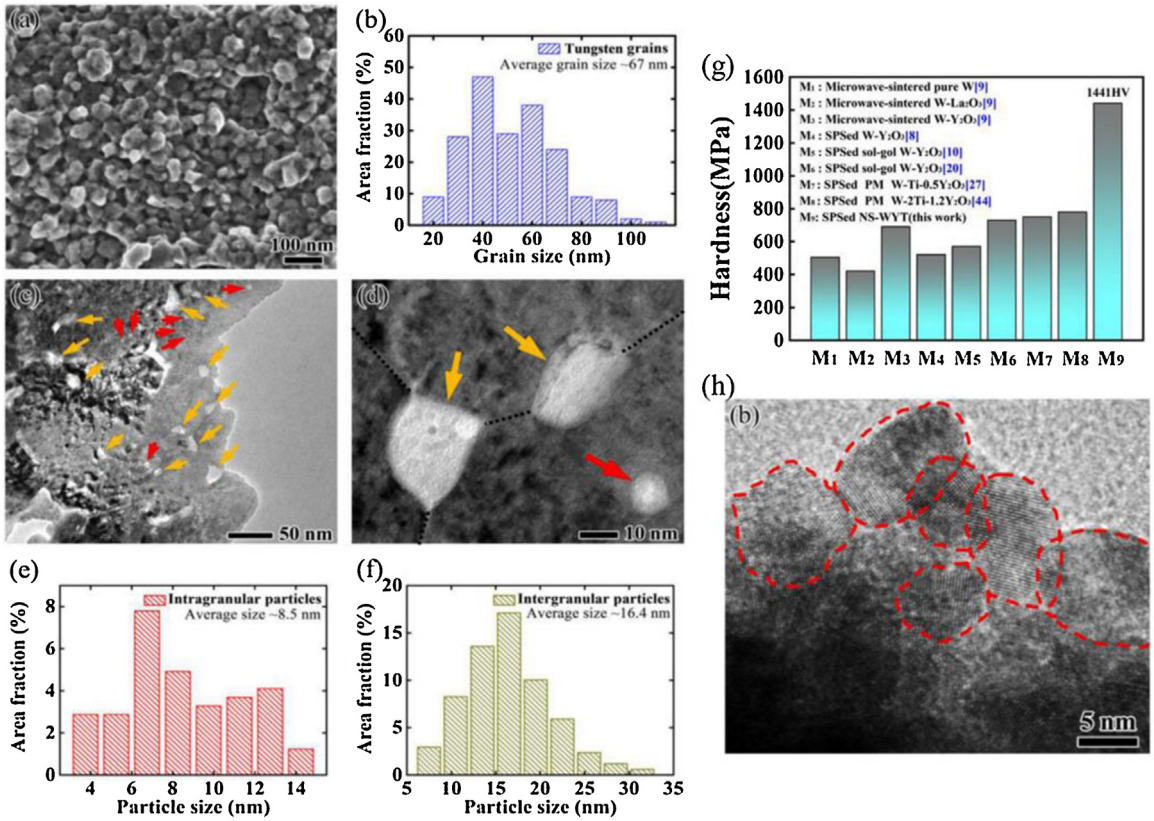

Fig. 15. (a) SEM image showing the fracture surface of high dense bulk nano structured WYT, (b) the size distribution in this nano structured WYT, (c)-(d) TEM images showing the size and distribution of nano particles in this WYT, and (e)-(f) histograms showing the size distributions of intragranular and intergranular nano particles, respectively. (g) Hardness of the present nano structured WYT, and comparison with other reported W-based alloys; (h) High resolution TEM image showing the nanocrystalline in W5Y5T after high energy ball milling [124].

are less pressurized in the interior of a grain in nanocrystalline. The value of the elastic strain energy is lower in the interior of the grain in nanocrystalline than that in monocrystalline. Moreover, in monocrystalline a significant increase in the elastic strain energy is observed, and in nanocrystalline it remains almost constant. Therefore, nanocrystalline with the high GB interface density would have better resistances to the deleterious effects of irradiation than that of the monocrystalline [48]. In experiment, Zhu et al. [131] studied helium irradiation behavior of coarse-grained tungsten (CGW) and nanocrystalline tungsten (NCW) fabricated by HPT. The result indicates that the degradation mechanisms of CGW and NCW are remarkably different. Blister occurs on the surface of CGW when the irradiation dose increases to $5.0 \times 10^{21}/m^2$. However, no blister is formed on the surface of NCW even when the irradiation dose increases up to $1.0 \times 10^{23}/m^2$. Instead in NCW, crack formation along GBs is the major degradation mechanism during helium irradiation. This explains the unprecedented irradiation tolerance of NCW in terms of blistering. Molecular dynamics results also show that GBs and helium clusters play an important role during the propagation of a crack. GBs play decisive roles in the irradiation resistance of nanostructured materials. It is thus suggested that excellent irradiation resistance can be achieved by a meticulous design of GBs based on an interface engineering. El-Atwani et al. [132] investigated the behaviors of the helium ion irradiation on UFG and nanocrystalline tungsten. They found that under helium irradiation at a low energy (70 eV), bubbles were uniformly distributed with no preferential bubble formation on GBs. It is known that 70 eV helium irradiation does not cause atomic displacements in tungsten. At higher energies that can cause displacements, bubbles were preferentially formed at the GBs only at high temperatures where vacancy migration occurs. Under these conditions (displacements and a high temperature), large facetted bubbles with dimensions less than 60 nm were observed at GBs in nanocrystalline tungsten due to the vacancies enhancing bubble growth by increasing the mobility of helium through the matrix in the form of helium–vacancy complexes. In this case, both the vacancies and helium are able to migrate and agglomerate to form bubbles [132]. However, in the absence of an irradiation-induced vacancy, helium atoms reaching a GB can only become immobilized in a pre-existing region of low electron-density on the boundary, combining with a thermal vacancy or continuing to migrate on the boundary until they reach a surface and escape. Therefore, increasing GB interface density can enhance the irradiation tolerance, but too small grain size will lead to large helium bubbles, resulting in damage of GBs and disappearance of the GB self-healing ability, as shown in Fig. 16

[132]. So the GB interface density should be meticulously controlled.

The above simulation and experiment results shown that the GB interface controlling is an effective way to improve the mechanical properties and irradiation resistance of tungsten or molybdenum-based materials.

3. Phase boundary interface controlling

In addition to GB interfaces, PB interfaces also can give rise to unprecedented properties such as high creep strength, excellent creep resistance, oxidation resistance and irradiation resistance.

It is known that Nb-based alloys have the potential for future aerospace as well as gas turbine applications because of its relatively low density, 1000 K higher melting temperature than those of Ni-based superalloys, and attractive high temperature strength

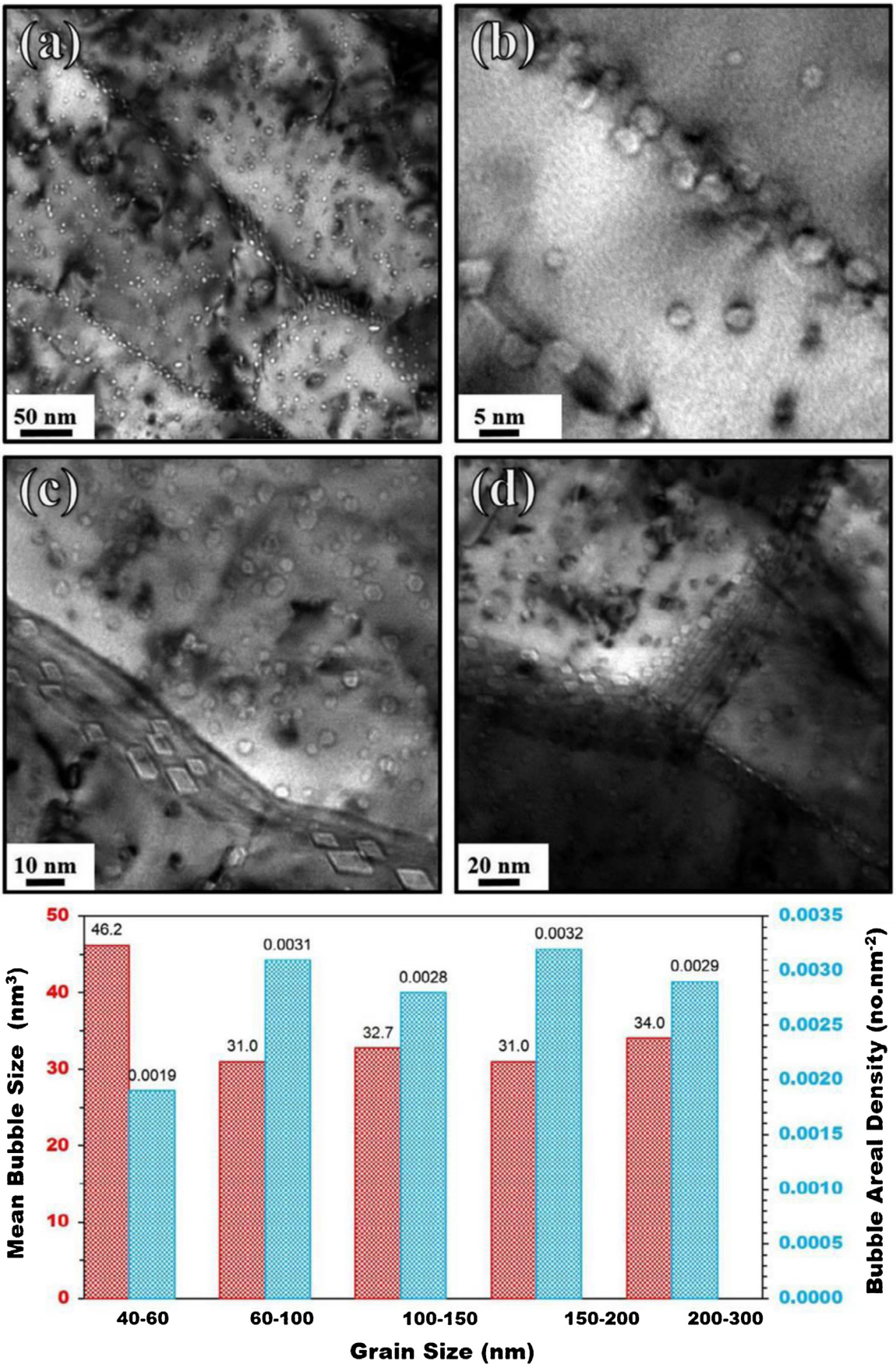

Fig. 16. (left) Bright-field TEM micrographs of UFG and NC tungsten irradiated with 2 keV helium ions (flux of 3.3×10^{16} ions m^{-2} s^{-1}) at 1223 K demonstrating: (a) overview of sample with bubbles decorating GBs at a fluence of 3.6×10^{19} ions m^{-2}; (b) nanocrystalline grain with large facetted bubbles/voids on GBs and few bubbles in the grain

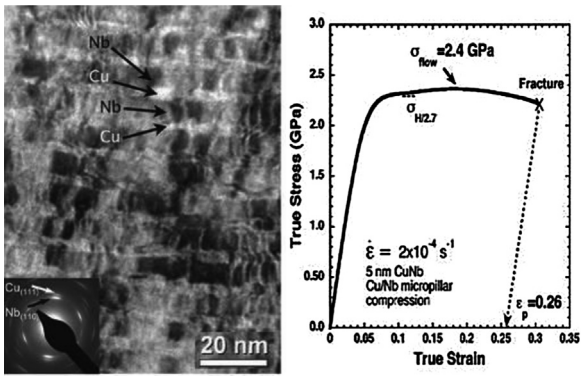

Fig. 17. TEM bright-field micrograph of as-deposited 40 nm Cu/40 nm Nb. Note selected area diffraction pattern showing {111}Cu//{110}Nb interface texture. Compression curves for 5 nm Cu/Nb multilayers. Note the high rate of work hardening up to a maximum flow stress of 2.4 GPa, followed by apparent work softening to failure at 26 % true plastic strain [138].

properties combined with moderate room temperature ductilities [133]. However, the poor oxidation resistance at high temperatures limits its practical application. In addition, continuous disastrous oxidation caused by oxygen embrittlement takes place even at 600 °C for pure Nb [133]. It is indicated that the oxidation resistance can be improved by addition of solution elements of Ti, Si, Al, Cr or Hf and secondary compound phases (such as (Nb, Zr)C [134], Nb_3Al [135] and Nb_5Si_3 [136]). In addition, these dispersing compound phases introduce a high density of PBs in the Nb matrix, which could effectively increase the creep strength and excellent creep resistance of Nb-based alloys. For example, Fujikura et al. [137] found that the Nb_5Si_3-reinforced Nb-Si-Mo-W-Hf alloys demonstrated an unprecedentedly excellent creep resistance and also a creep rupture strength exceeding the target strength (450 MPa) of 150 MPa and above at 1773 K for 100 h. The fractographic and TEM observations indicated that the Nb solid-solution/Nb_5Si_3 PB interface play an important role in the increase of creep resistance [137].

The high density of PB interfaces also can increase the mechanical properties and irradiation resistances of the Nb, Ta and V based composites. For example, Mara et al. found that the 5 nm Cu/Nb nanolayered composites developed by sputter deposition exhibit extremely high flow strength of 2.4 GPa, and significant ductility with more than 25 % true strain [138], as shown in Fig. 17. The strengthening mechanism is the single dislocation deformation mechanism where individual dislocations cross the nanolayered Cu/Nb interfaces. The PB interface plays a very dominant role for the excellent mechanical properties. Furthermore, nanomaterials with nearly perfect, atomically ordered low-energy PB interfaces have been found to possess extraordinary thermal stability and radiation tolerance [21,30,62,139–142]. Recent studies show that immiscible Cu/Nb (Cu/V, Cu/Mo) metallic nanolayer films with very large phase interfacial areas, particularly those with a layer thickness of a few nanometer, are extremely resistant against He ion irradiation [141,143–146]. Irradiated at the same condition, a major difference in Cu/V 50 nm nanolayer and Cu/V 2.5 nm is that the peak He bubble density in the Cu/V 50 nm nanolayer is three times larger than that of the Cu/V 2.5 nm specimen. On the other hand, the peak bubble density of irradiated Cu/V 50 nm nanolayer specimens is lower than that of single layer polycrystalline Cu films, suggesting the extraordinary capability of Cu/V interface in reducing point defect concentration compared to their single-phase bulk counterparts. The magnitude of swelling in nanolayers clearly decreases with decreasing the layer thickness [143]. The swelling in irradiated Cu/V 2.5 nm nanolayer is approximately two times lower than that in Cu/V 50 nm nanolayers. Furthermore, swelling in all irradiated Cu/V nanolayers is less than rule-of-mixture swelling in irradiated single layer Cu and V films, as shown by the horizontal dash line in Fig. 18 [143]. In V/Ag multlayers, the irradiation results further certified the retardation of bubble growth and irradiated swelling by V-Ag interfaces [147,148]. Another representative composite with the combination of metal and nonmetal is the V-graphene nanolayer material fabricated by combing physical sputtering with chemical vapor deposition, which exhibits ultra-high strength and excellent radiation tolerance as compared with pure V [149] (see Fig. 19). The V-graphene nanolayers had reduced formations of radiation induced crystalline defects compared with pure V, which was confirmed by the reduction in radiation induced hardening and suppression of brittle failure [149]. *In-situ* SEM compression tests showed that V-graphene interfaces can hinder the crack propagation thus helping to suppress the brittle failure. In addition, the He bubble formation was shown to be significantly reduced in V-graphene nano-layers due to the impermeability of He through the graphene layer that prevents agglomeration of He gas into large bubbles. Therefore, nano-layer PB interfaces can not only induce initially high strength materials, but also the interface can self-heal the crystalline defects introduced by irradiation as well as terminate migration of He bubbles to lead to radiation tolerance materials.

It is notable that in these nano-layer films, the two materials should be immiscible, otherwise, the intersoluble element would produce new phase. However, the above nano-layers are fabricated by using physical sputtering, which is very limited for preparing bulk materials in large scales. In addition, nanomaterials with disordered, high-energy interfaces are not stable in extreme conditions. Therefore, the ordered and low-energy PB interfaces are desired to be developed for improving performances.

In 2015, Beyerlein et al. discovered that a top-down bulk metal-working technique of the accumulative roll bonding (ARB) which imposes extreme amounts of plastic strains can give rise to a preferred bimetal interface with perfect atomic order [150]. Cu-Nb nano-layered materials in bulk form were fabricated with an ARB process including multiple cycles of rolling, cutting and stacking [150]. The interfaces with an atomic level order emerge ubiquitously in this large-scale layered Cu-Nb nanocomposite. In addition, these ordered interfaces are shown to be stable with respect to further straining, high-temperature exposure, and irradiation, giving the nanomaterial extraordinary tolerances in extreme conditions. As shown in Fig. 20A, the initial layer dimension h is about 20 nm. After annealing at 500 °C for 1 h, the interface structure and parent nanostructure of the h = 20 nm are retained, (Fig. 20B), indicating the good thermal stability. Under He-ion irradiation the interface does not develop damaging voids like ordinary GBs in Cu, as shown in Fig. 20C [150]. In addition, the bulk Cu/Nb nano-layered sheets exhibit excellent shock resistance and ultra-high strength [151–153]. The detailed information of Cu/Nb interface shows that a stable interface is observed with two configurations slightly misoriented by ~7°, as shown in Fig. 20D. The atomic

matrix at a fluence of 3.6 × 10^{19} ions m^{-2}; and (c) GB and (d) GB triple-junction decorated by facetted bubbles with different sizes inside ultrafine grains at fluence of 4.0 × 10^{20} ions m^{-2}. Bubble areal density (right columns) and average bubble size (left columns) versus grain size for 2 keV helium ions irradiation at 1223 K and a fluence of 3.6 × 10^{19} ions m^{-2}. Bubbles located on GBs were not counted. A total of 18 neighboring grains were analyzed in order to ensure maximum consistency in ion fluence, sample thickness and irradiation temperature [132].

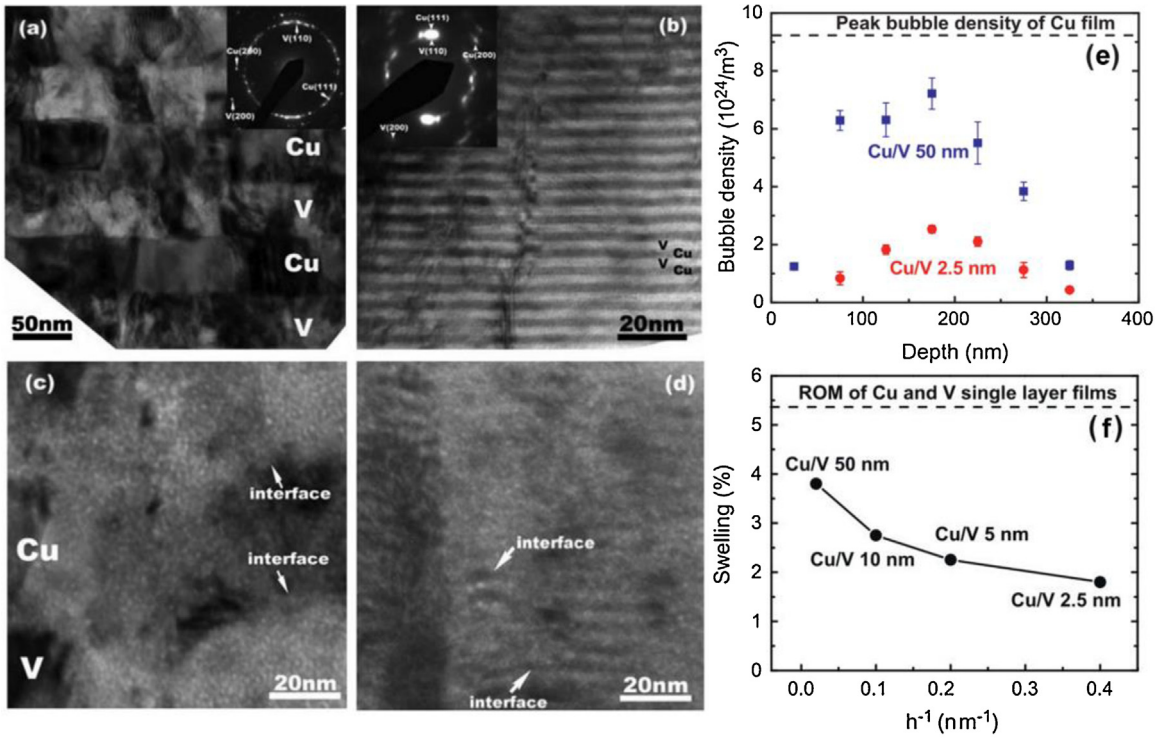

Fig. 18. Cross section TEM (XTEM) images of as-deposited (a) Cu/V 50 nm, and (b) Cu/V 2.5 nm nanolayers. Films with smaller individual layer thickness (h) have a stronger Cu{111} and V{110} fiber texture. (c) and (d) Peak damage regions of irradiated Cu/V 50 nm and Cu/V 2.5 nm nanolayers, respectively. He bubbles are observed in both Cu and V. (e) Comparison of He bubble density distributions along film normal direction underneath the surface in ion irradiated Cu/V 2.5 nm and Cu/V 50 nm nanolayers. Peak He bubble density is reduced by a factor of ~3 in Cu/V 2.5 nm,compared to that in Cu/V 50 nm specimens. (f) Swelling vs. 1/h in ion irradiated Cu/V nanolayers, where h is individual layer thickness, shows a continuous swelling reduction with decreasing layer thickness [143].

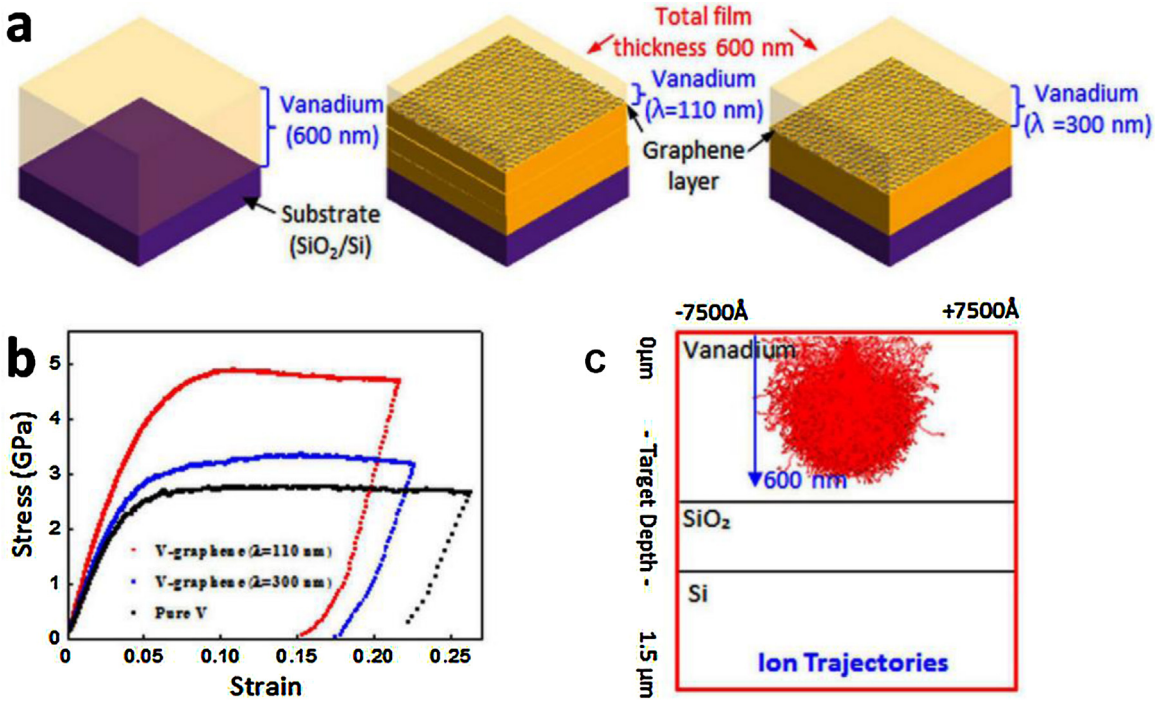

Fig. 19. (a) Schematic for pure V and V-graphene nanolayers with repeat layer spacing (λ) of 110 nm and 300 nm. (b) Stress-strain curve determined from nanopillar compression testing of pure V, and V-graphene nanolayers with 110 nm and 300 nm repeated layer spacings. (c) SRIM ion trajectories of He^+ irradiation on V thin film under condition of 120 keV [149].

level ordered interfaces have a low formation energy, which is a strong criterion for interface stability. Meanwhile, the high density of the low-energy Cu/Nb interfaces and the low density of accumulated high-energy defects in the layers also contribute to the above excellent performances [154]. The forecasted lifetimes of these bulk nanomaterials, dense with naturally selected interfaces

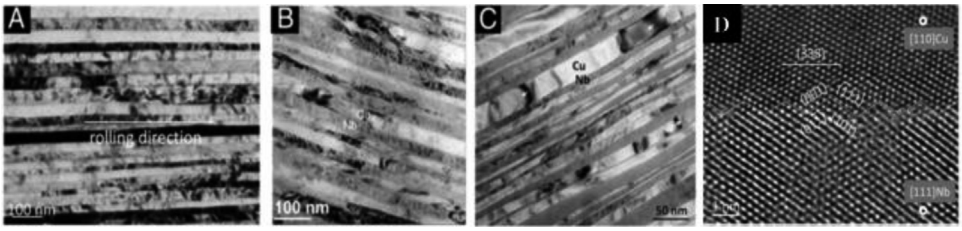

Fig. 20. Transmission electron microcopy micrographs displaying the planar Cu–Nb interfaces after (A) extreme plastic strains of ~12, which produces an h = 20 nm composite, (B) elevated temperatures of 500 °C, which is 0.45 times the melting temperature of Cu (32), and (C) helium-ion irradiation, showing no voids in the layer or in the interfaces in an h = 20 nm composite, (D) the high-resolution transmission electron microscopy micrographs of the preferred Cu–Nb interface [150].

would, therefore, significantly exceed those of their constituents. This work opens up an alternative route for fabricating the ordered and stable PB interfaces with low-energy states.

In the ARB multilayered composites, the shear bands occur frequently due to the different strength and work hardening abilities between constituent layers [155,156]. The plastic instabilities during the ARB process is an obstacle for fabricating nanolamellar multilayers with higher strength such as Cu/Ta [157]. In addition, the appearance of edge cracks at higher ARB cycles also prevent a further refinement of the layer thickness. Based on ARB methods, Zeng et al. [62,141] developed a cross accumulative rolling bonding (CARB) method combined with an intermediate annealing process to eliminate plastic instabilities and the formation of edge cracks. The detailed sketch map is shown in Fig. 21 [62]. The bulk Cu/Ta (Cu/V) nanolamellar multilayers with an individual layer thickness from several micrometers down to 50 nm were successfully fabricated, as shown in Fig. 22 [62]. With decreasing h from 430 nm to 50 nm, the tensile strength increases from 500 MPa to 950 MPa (see Fig. 23a). The average hardness variation trend is consistent with the Hall-Petch behavior that the values increase with decreasing the layer thickness h (see Fig. 23b), indicating that the Cu/Ta PB interfaces act as barriers against dislocation motion. The hardness reached an ultra-high value of 3.48 GPa for h =50 nm. The high hardness of the CARB Cu/Ta nanolamellar multilayers is attributed to the large amount of deformation and the interface structure. The nanosized PB interfaces were indicated having the semi-coherent structures which play an important role in achieving the high strength and hardness. In addition, the CARB process introduced a high density of dislocations, non-equilibrium GBs and lead to a strong grain refinement. The refined grains and the high defect densities result in a much higher strength and a reduced ductility compared with the coarse grained counterparts. Fig. 23c presents the thermal stability of the Cu/Ta nanolamellar multilayers through the evolution of hardness. The hardness of the un-annealed multilayers sample is 3.48 GPa. After annealing at 500 °C for 1 h, the hardness keeps at a constant value of 3.48 GPa. When further increasing the annealing temperature up to 600 °C, the hardness just gradually decreases to 93 % of the initial value. After 800 °C annealing for 1 h, the hardness decreases to 75 %. Even so, this composite still has a higher hardness than the pure Cu and Ta samples after annealing at 800 °C [62]. This outstanding thermal stability is attributed to the atomically flat bimetal PB interfaces and decreasing amount of unstable homophase GBs.

Based on the Cu/Ta preparation, Zeng et al. [141] developed anthor PB interface dominant bulk Cu/V nanolamellar composites with different layer thickness by CARB. These composites have individual layer thicknesses h ranging from 300 μm down to 25 nm. Fig. 24 shows some examples of layer morphology of the CARB Cu/V nanolamellar composites after 3–6 rolling cycles, corresponding to an average layer thickness of 38.0, 19.0, 9.0 and 4.0 μm, respectively. A controlled and continuous layer structure has still been achieved in all samples despite the presence of a wavy and non-planar Cu/V interfaces. In CARB Cu/V multilayer composites, shear bands were not obvious, indicating that this CARB technique can indeed suppress the occurrence of shear bands in comparison with the normal ARB methods [141]. Cu/V nanolamellar composites with the layer thickness h =25 nm (see Fig. 25a) present that in each single layer thickness grains with an extremely high aspect-ratio are achieved, which implies the extremely increasing density of bimetal PB interfaces and the remarkably decreasing density of GBs after the multistep CARB process. This behavior is therefore different from the grain refinement caused by SPD, which leads to a high fraction of disordered GB interfaces with the high energy state. Typical HR-TEM image in Fig. 25b reveals that the Cu/V interface is atomically ordered and chemically sharp [141].

The hardness and thermal stability of the Cu/V nanolamellar composites are presented in Fig. 26 [141]. The hardness of the CARB Cu/V composite increases linearly with decreasing the layer thickness from sub-micrometer to nanometer, and reaches a maximum value of 3.68 GPa at h =25 nm. This result indicates that the abundant Cu/V heterophase interfaces in the nanocomposite can serve as pining points to hinder dislocation movement during deformation, and hence strengthen the material. The CARB Cu/V nanocomposite (h =25 nm) retains its hardness even after annealing at 600 °C, demonstrating a better thermal stability as compared to other nanocomposites prepared by SPD. After the 200 keV He ion irradiation with a fluence of 2×10^{21} ions/m^2 [144], the smooth, intact surface with continuous nano-layered structure is maintained, as shown in Fig. 27a, and there is a neglectable irradiation-induced hardening, suggesting that bulk nanolamellar Cu/V composite retains stable under high-energy He ion radiation. In contrast, under an irradiation fluence of 7×10^{22} ions/m^2, numerous notable He bubbles and GB grooving are observed. However, bubble-free zones (BFZs) with no signs of He bubbles are frequently observed near the Cu/V interfaces, as highlighted in Fig. 27b. It's indicated that the formation of BFZs is a consequence of the absorption and annihilation of irradiation-induced defects and the preferential trapping of He at Cu/V interfaces [21,31]. These results highlight that the Cu/V bimetal interfaces from immiscibility of Cu and V phases during the CARB deformation process stabilize the structure under high temperature and irradiation conditions.

To sum up, CARB processing is indeed an effective approach to construct stable PB interfaces with low-energy states. The low-energy stated PB interfaces could significantly increase the stabilities of nano structures under high temperature and irradiation conditions.

4. Synergistic effects of multi-scaled phase/GB interfaces

As described above, the modulation of GB interface or PB interface can effectively control the performance of refractory metals. Therefore, the synergistic effect of GB and PB interfaces should be more remarkable. The coexistence of decorated GB and PB interfaces can be achieved through adding second phase particles such as oxide, carbide or inter-metallic compounds into the matrix. The

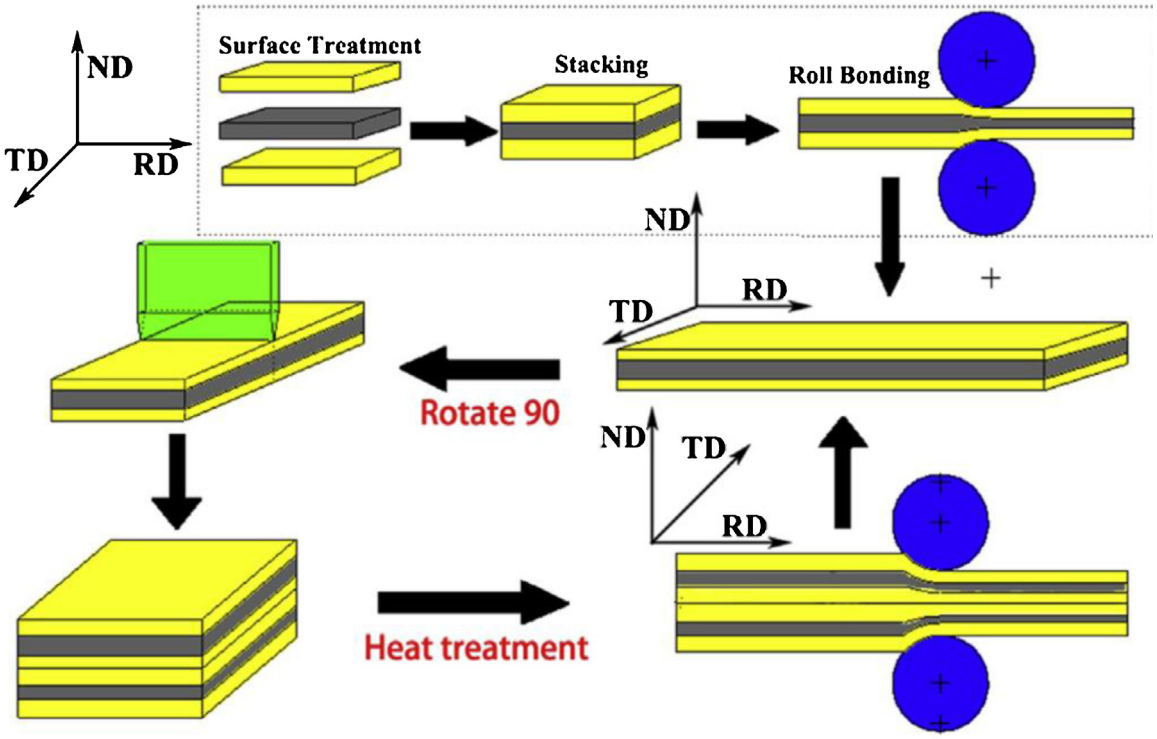

Fig. 21. Schematic illustration of the CARB process [62].

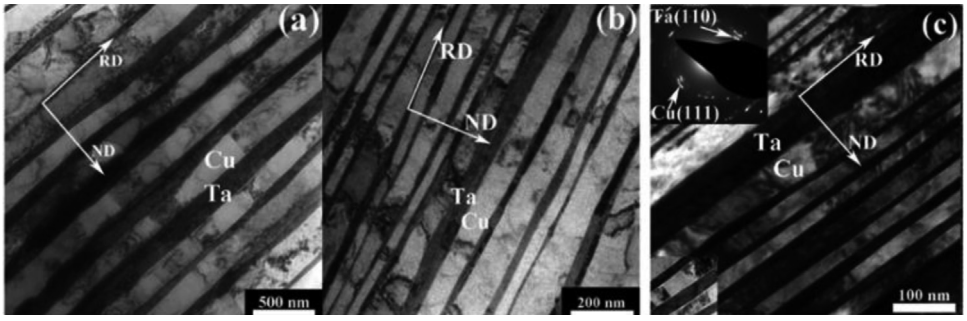

Fig. 22. Representative TEM images obtained for nanolamellar Cu/Ta multilayers prepared via CARB for different individual layer thicknesses *h*: (a) *h* =230 nm, (b) *h* = 110 nm, (c) *h* =50 nm [62].

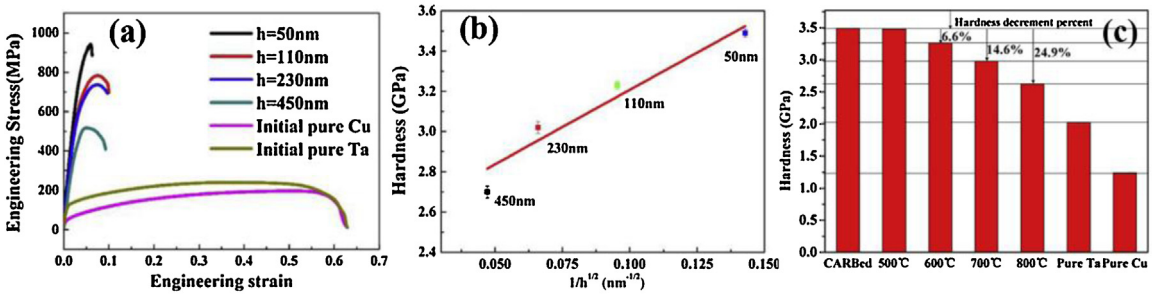

Fig. 23. (a) Bulk tensile stress-strain curves for the CARB Cu/Ta nanolamellar multilayers; (b)Average nanohardness versus 1/*h* 1/2 for the CARB Cu/Ta nanolamellar multilayers; (c) Variation of the nanohardness after an annealing at elevated temperatures for the sample with a layer thickness *h* =50 nm [62].

second phase particles could pin the migration of the GBs, hinder grain growth and thus refine grains. As discussed above, abundant GB areas can drive down the concentration of deleterious solutes in the lattice and the refined microstructure will result in an increase in strength. Meanwhile, the nanosized second phase particle can produce extensive PB interfaces between the particles and the matrix, which act as sinks for irradiation-induced point defects, and thus have potential in improving the irradiation resistance [158]. In addition, the dispersion particles are expected to stabilize the GBs in nano-grained materials upon thermal annealing and/or irradiation [90]. For oxide dispersion strengthened (ODS) molybdenum and molybdenum-titanium-zirconium (TZM) alloys, the fine grains

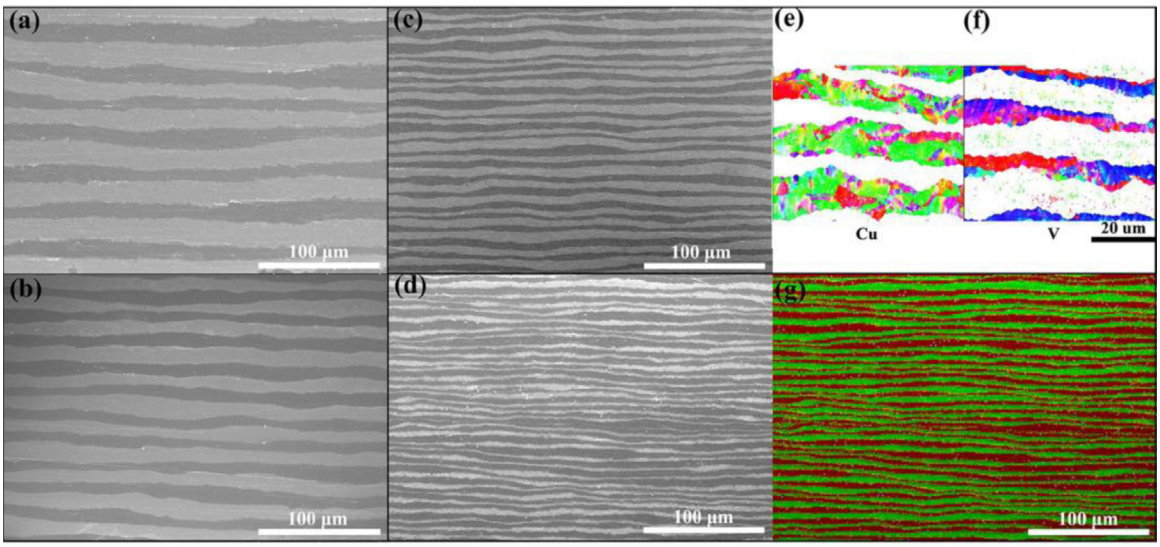

Fig. 24. SEM cross-sectioning images of the CARB Cu/V multilayer composite with controlled individual layer thickness *h*: (a) *h* =38.0 μm, (b) *h* =19.0 μm, (c) *h* =9.0 μm, and (d) *h* =4.0 μm. EBSD-based inverse pole figure (IPF) maps (*h* =9.0 μm) for (d) Cu layers and (e) V layers, respectively. (g) EDS-mapping image of layer thickness *h* =4.0 μm nanocomposites after 3-6 rolling cycles, corresponding to an average layer thickness of 38.0, 19.0, 9.0, and 4.0 μm, respectively [141].

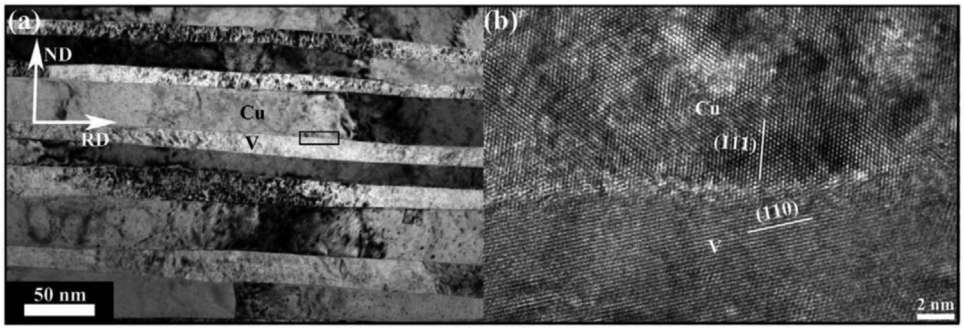

Fig. 25. A typical layer morphology and interface structure of Cu/V nanocomposite with individual layer thickness *h* =25 nm. (a) Typical bright field TEM image exhibiting single crystal layers with extremely high-aspect-ratio grains. (b) Representative HRTEM image of the predominant interface in the 25 nm CARB material, which is atomically ordered and sharp [141].

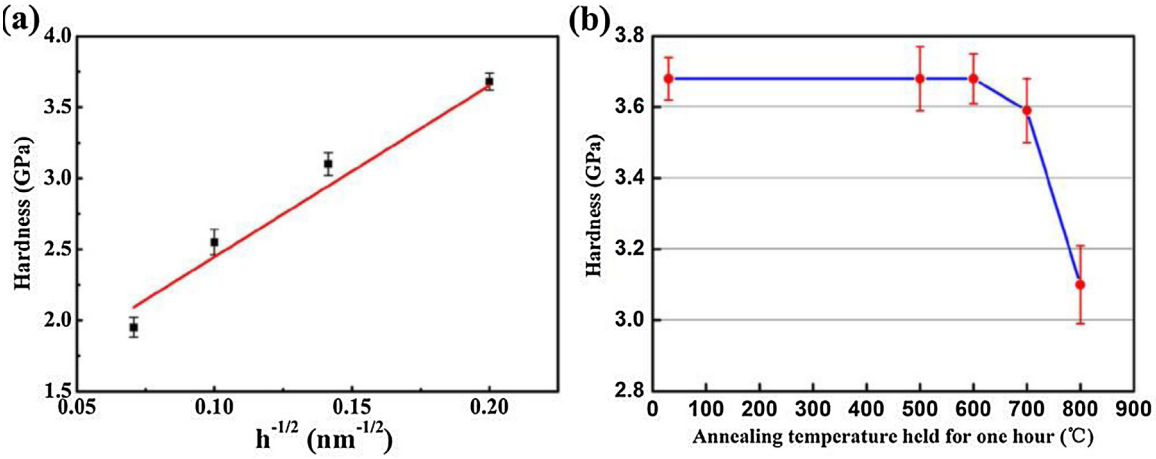

Fig. 26. High strength and thermal stability of the bulk Cu/V nanocomposite. (a) Average nanohardness versus $h^{-1/2}$, showing that strength increases with decreasing layer thickness by the Hall–Petch scaling law. (b) Hardness reduction as a function of annealing temperature exhibiting outstanding thermal stability of CARB Cu/V nanolamellar nanocomposite [141].

induced the high density of GB interfaces and nanosized oxides produced extensive PB interfaces, which synergistically raise the tensile and creep strength [159,160]. The addition of second phase particles can be done by the following traditional approaches: i) powder blends of solid refractory metal (i.e. W and Mo) based powders with solid oxide powders (a S–S doping route [161,162]) and ii) mixed with a liquid rare-earth solution (S-L doping) [163,164]. In Mo–xLa_2O_3 (x = 0, 0.5, 1.0, 1.5 and 2.0 wt. %) alloys prepared

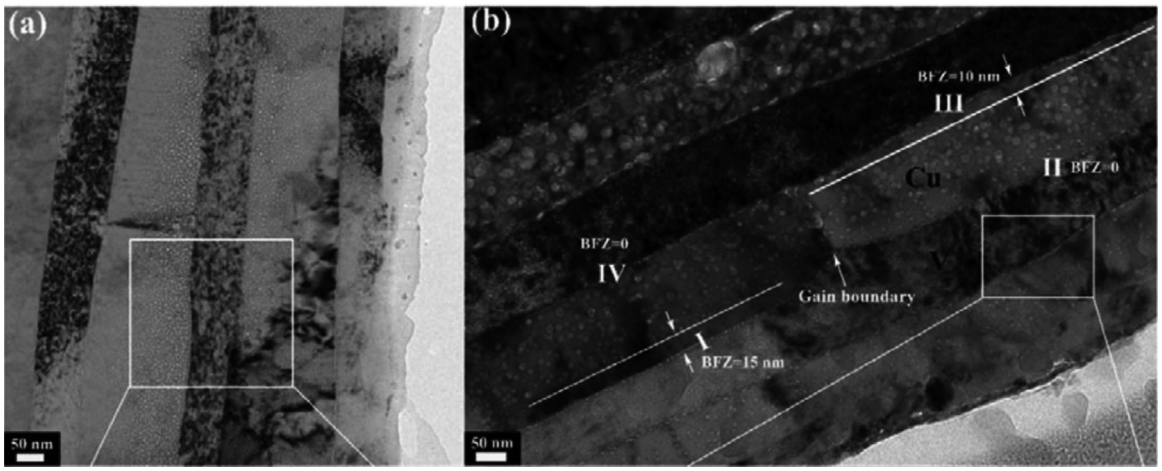

Fig. 27. High magnification TEM images of an He implantation zone with depth ranging from surface to 600 nm: (a) microstructure with small size He bubbles and limited damage region after He implantation with fluence of 2×10^{21} ions/m^2, (b) microstructure with large size He bubbles accompanied with grain boundary grooving after He implantation with fluence of 7×10^{22} ions/m^2 [144].

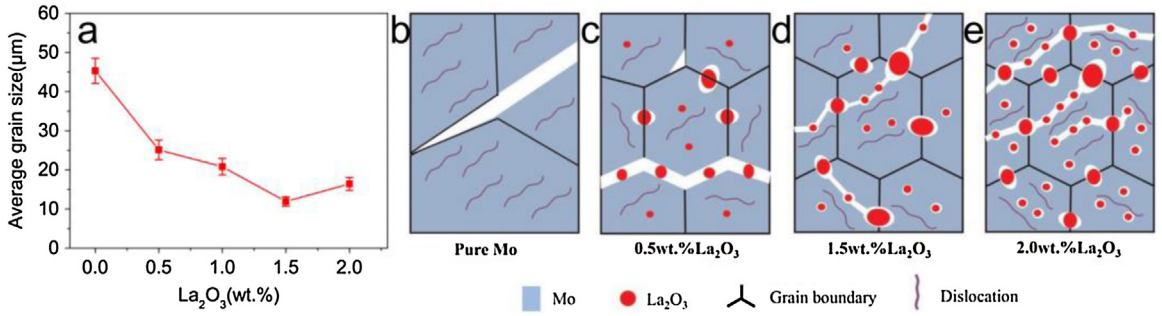

Fig. 28. (a) Grain size in the pure Mo, Mo-0.5 wt. %La_2O_3, Mo-1.5 wt. %La_2O_3 and Mo-2.0 wt. %La_2O_3, and (b)-(e) Sketches illustrating the fracture process of the pure Mo, Mo-0.5 wt. %La_2O_3, Mo-1.5 wt. %La_2O_3 and Mo-2.0 wt. %La_2O_3 [161].

by using the S–S doping method, the addition of La_2O_3 particles effectively refines the grains and significantly elevates the recrystallization temperature of the Mo alloys. The average grain size decreases from 45 μm to 15 μm with increasing La_2O_3 content from 0 to 2.0 wt. %, as shown in Fig. 28. At the same time, the increasing La_2O_3 content not only changed the GB interface state with reducing the grain size, but also increased the PB interfaces. The nano La_2O_3 particles located at the GBs could strengthen the GBs, resulting in intragranular fractures and an obvious enhancement of the ductility. The low cycle fatigue testing results revealed that the pure Mo experienced cyclic hardening behaviors, while the ODS-Mo alloys exhibited cyclic softening behaviors because the ODS-Mo possessed a higher fatigue ductility and longer fatigue life than that of the pure Mo [162]. In addition, the high density of PB interfaces in ODS Mo could introduce a higher concentration of denuded zones along GBs and improved ductile-laminate toughening that results in improved resistance to irradiation embrittlement [165]. However, in S-S or S-L mixing processing route, the oxide particles tend to coarsen at the GBs, and these coarse hard particles introduce stress concentrations at the GBs and tend to localize strains and cracking near them, as shown in Fig. 28 [161]. The key to prolonged ductility is to split these oxide particles into nanosized ones (nanosized PBs) and spread them into the grain interior, rather than leaving them coarsened and concentrated at the GBs, which not only can alleviate the stress concentration behaviour, but also encourage dislocation trapping by the particles in the grain interior, which would help sustain work hardening and uniform elongation. The liquid-liquid (L-L) mixing process can achieve this goal to construct a harmonious microstructure with nanosized La_2O_3 particles (nanosized PBs) homogeneously dispersing in the Mo grain interior [166], as shown in Fig. 29. The L-L process ensures mixing on the molecular level, and encourages heterogeneous nucleation to form core-shell structures. The outcome is a nanostructured Mo alloy with nanoscaled La_2O_3 particles mostly distributed inside the interior of ultra-fine grained Mo. This nanostructured Mo alloy exhibits an unprecedented combination of strength and ductility: the yield strength is ~820 MPa and the total tensile elongation to failure is as large as 38 % at RT, as shown in Fig. 29. At the same time, the fracture toughness and DBTT are also obviously improved. This strategy helps guiding endeavours to design other dispersion-strengthened alloys to simultaneously achieve high strength and good ductility by controlling the size and distribution of the PB interfaces. For example, a similar nano-structuring strategy is indicated to be effective for the tungsten-based alloys.

The performance of tungsten based alloys and composites can also be controlled by GB/PB interfaces by adding thermally stable fine particles, which are usually oxides (e.g., La_2O_3 and Y_2O_3) or carbides (e.g., ZrC, HfC and TiC), forming the oxide or carbide dispersion-strengthened (ODS or CDS) tungsten alloys [54,78,167–174]. Recently, various ODS-W or CDS-W materials with improved performances have been fabricated [78,79,175]. ODS-W such as W-La_2O_3 and W-Y_2O_3 showed higher strength, higher recrystallization temperatures and higher thermal shock resistance than that of pure W [27,53,172,175]. For instance, W–(0.3, 1.0, 2.0)Y_2O_3 materials produced by mechanical alloying (MA) and hot isostatic pressing (HIPing) or microwave sintering have fine grains with the grain sizes ranging from 20 to 500 nm and contain a high density ($5.4–6.9 \times 10^{22}$ m^{-3}) of nanosized Y_2O_3

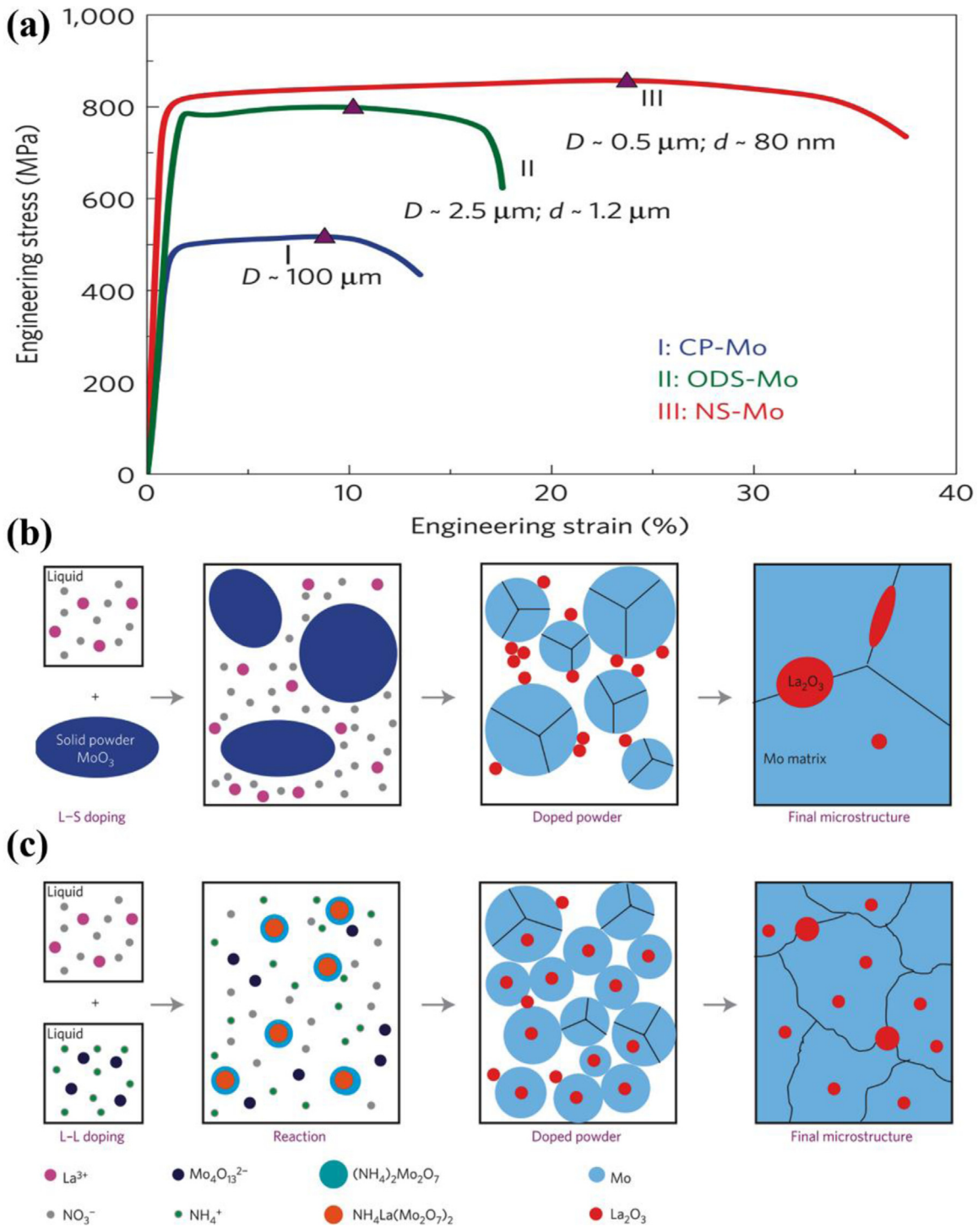

Fig. 29. (a) Comparison of room-temperature tensile behaviour for three different types of Mo alloys: tensile engineering stress–strain curves of CP-Mo with grain size D ~100 μm, ODS-Mo alloy with grain size D ~2.5 μm and oxide particle size d~1.2 μm, and NS-Mo alloy with grain size D ~0.5 μm and oxide particle size d ~80 nm Comparison of (L-L) mixing and liquid-solid (L-S) mixing processes and resulting microstructures: (b) Schematics showing the microstructural development in the L–S mixing/doping (c) and L-L mixing/doping processes that produced the ODS-Mo and NS-Mo alloys, respectively [166].

particles with sizes between 1 and 50 nm [176,177]. These refined grains and nanosized particles produce high densities of GB/PB interfaces, which generate high strength and a promising radiation resistance. The influences of different sintering and post treatment on GB/PB interfaces and performances of W-Y_2O_3 materials are obvious [178–181]. Several different W-Y_2O_3 materials were manufactured by spark plasma sintering (SPS) and high temperature sintering in combination with hot rolling or forging deformations, respectively. They were investigated as potential plasma facing materials with respect to thermal physical properties, mechanical properties, and thermal shock responses. For the SPSed W-Y_2O_3, the tungsten grains exhibit an isotropic microstructure with an average grain size of 3.2 μm and the average size of Y_2O_3 particles is about 80 nm [177,180]. For the sintered W-Y_2O_3 in flowing H_2, the average grain size of tungsten is about 3 μm and Y_2O_3 particles are located at the GBs with a typical bimodal size distribution

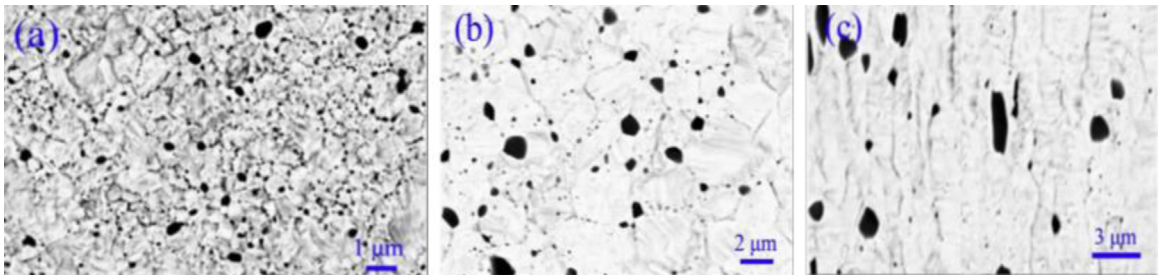

Fig. 30. SEM images and size distribution histograms for visible dark Y_2O_3 particles of (a) SPSed W-Y_2O_3, (b) sintered W-Y_2O_3 in flowing H_2 and (c) deformed W-Y_2O_3 [178].

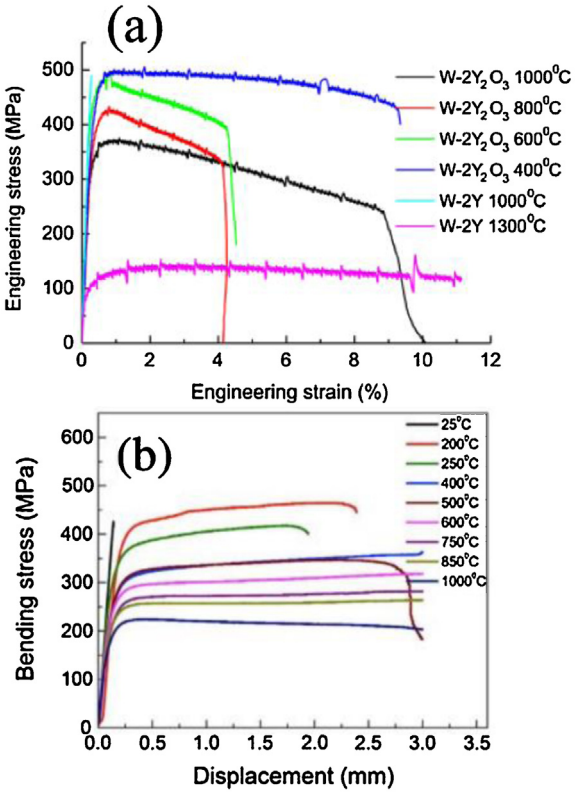

Fig. 31. Temperature-dependent tensile stress-strain curves of (a) sintered and (b) hot-forged W-$2Y_2O_3$ [180,181].

(~0.68 and 1.1–1.7 μm, respectively), as shown in Fig. 30a [178]. After hot rolling, the size and shape of both W grains and Y_2O_3 particles have been changed: the grain size increasing along the rolling direction, in other words the PB/GB interface becoming elongated, leading to the anisotropy [181]. The thermal conductivity of deformed W-Y_2O_3 showed nearly 35 % and 17 % higher values than that of SPSed W-Y_2O_3 at RT and at 1473 K, respectively, due to the increased relative density and decreased PB/GB interface scattering of electrons [181]. Three point bending tests at RT and tensile tests at elevated temperatures showed that the rolled W-Y_2O_3 had a better mechanical strength and toughness than that of the sintered one, as presented in Fig. 31. The tensile tests showed that the sintered W-Y_2O_3 is fully ductile in the temperature range of 673–1273 K: the total elongation is between 4% and 10 % (Fig. 31a). As the testing temperature increased from 473 K to 1273 K, the ultimate tensile strength of the rolled W-Y_2O_3 decreased from 841 MPa to 532 MPa, as shown in Fig. 31b. As compared to ultra-high-purity tungsten, the rolled W-Y_2O_3 performed a higher strength at elevated temperatures [180,181]. The thermal shock response result revealed a superior thermal shock resistance of the rolled W-Y_2O_3: no cracks but only surface roughening was found on the loaded surface after 100 shots at an absorbed power density of 0.6 GW/m^2 for a pulse duration of 1 ms at RT, as shown in Fig. 32 [178]. Besides, the thermal loading induced melting and recrystallization behaviors of deformed W-Y_2O_3 were less obvious than those of SPSed W-Y_2O_3 [178]. The discrepancy in thermal shock response between the two materials and in particular the superiority of deformed W-Y_2O_3 agrees well with the results that the better thermo physical and mechanical properties the better thermal shock resistances.

The high-energy-rate forging may significantly improve mechanical properties by changing the PB/GB interfaces [179]. It is indicated that grains with the size range from a few to more than 50 μm (bimodal distribution) were formed in forged W-Y_2O_3. A detectable plastic deformation (a total elongation (TE) of 2.9 %) associated with work-hardening occurs at 100 °C, and the ultimate tensile strength (UTS) of this forged W-Y_2O_3 material increases drastically to 1040 MPa. Pronounced tensile ductility is observed in the forged W-Y_2O_3 at 200 °C with a plastic strain as large as TE = 5.5 %.

For the swaging deformed W-Y_2O_3, tungsten grains are round-bar shape with an approximately circular shape along with the cross section and elongated shape in the swaging direction, as shown in Fig. 33 [129]. The average length and diameter of tungsten grains in swaged W-Y_2O_3 are 26.7 and 4.6 μm, respectively, corresponding to an aspect ratio of about 6:1 [129]. The tensile results shown that it is brittle until above 250 °C, and its strength is also smaller than that of the high-energy-rate forged ones [129], which implies that bimodal interfaces (in forged ones) may be more in favor of strength and ductility. Therefore, it emphasizes again that the microstructure design (decorating the GBs) through different deformation processed is important.

Although the addition of Y_2O_3 can produce PB interface and control GB interface, but it cannot reduce the detrimental impurities of oxygen. Xie et al. [27] added Zr element into W-Y_2O_3 to absorb free oxygen at GBs to form Y-Zr-O particles. The particle size of Y-Zr-O can be further reduced compared to the Y_2O_3 particles, as shown in Fig. 34. Because the improved PB/GB interfaces by Zr, the strength and plasticity of this W-Zr-Y_2O_3 increases further on the base of W-Y_2O_3.

However, the above mentioned ODS-W still exhibits a relatively high DBTT and poor low-temperature ductility, which resulted from the coarsening oxide particles that tend to segregate at GBs, and thus introduce stress concentration at the GBs and lead to weak GBs [90,166,182]. To solve this problem, some wet-chemical synthesis routes (L-L processes) offering molecular-level mixing have been developed, and shown some potential in inhibiting the particle coarsening and fabricating nano-structured ODS-W [87,122,158,183–187]. For example, a nanostructured W-Y_2O_3 composite were prepared by an improved bottom-up wet chemical method and consolidated using the SPS technique [186,187]. It is found that the average grain size is about 0.76 μm and the oxide particle sizes are significantly reduced to about 2−10 nm and these nanoparticles are dispersed uniformly in the tungsten matrix, as shown in Fig. 35 [186]. Due to the ultrafine grains and uniformly

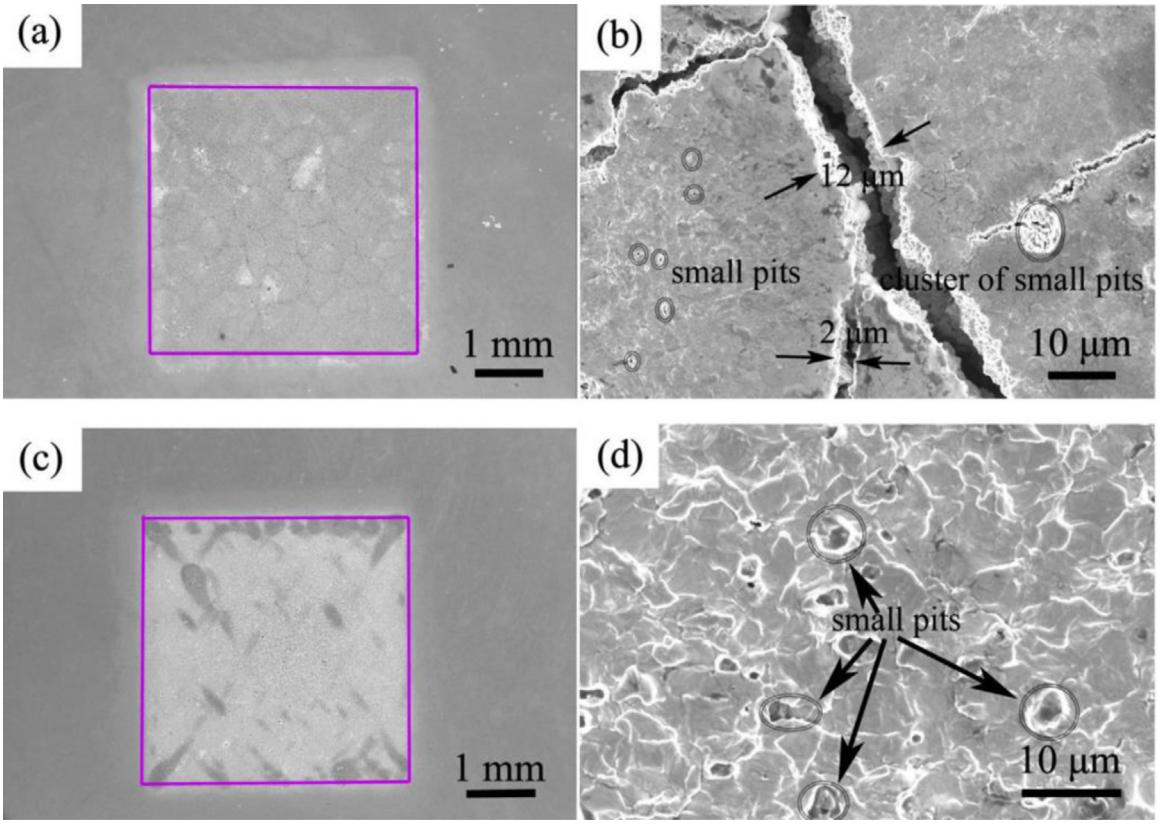

Fig. 32. Damage characteristics of the investigated materials after thermal loading with 100 pulses at 0.6 GW/m^2 for 1 ms at RT. (a) the loaded surface of SPSed W-Y_2O_3, (b) the magnification of (a), (c) the loaded surface of deformed W-Y_2O_3, (d) the magnification of (c). The loaded areas are indicated by a red square (4 × 4 mm^2) for the electron beam loading [178].

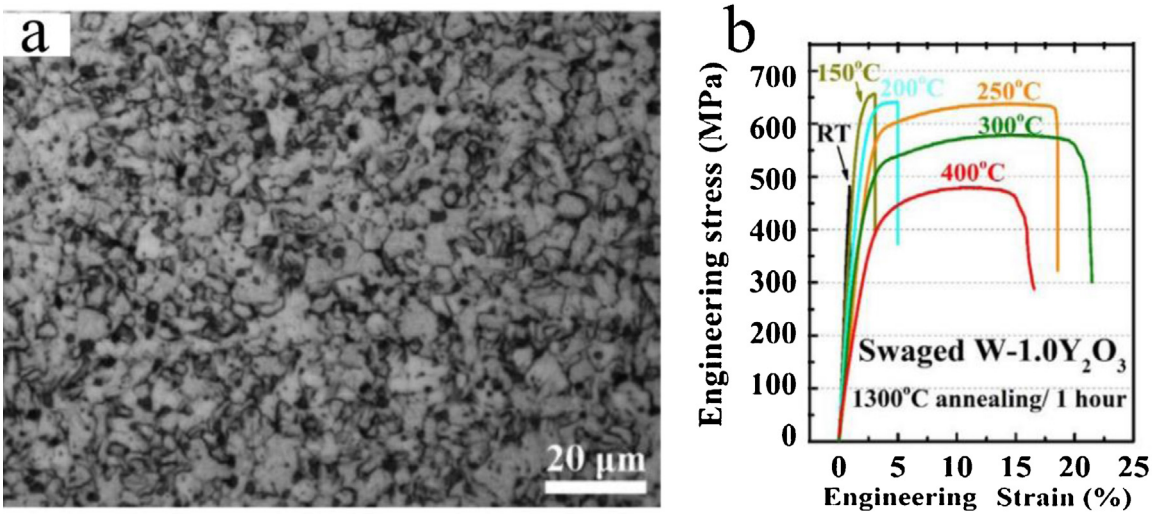

Fig. 33. (a) Optical micrograph of R direction of swaged W-1.0Y_2O_3; (b) Tensile behavior of swaged W-1.0Y_2O_3 at various testing temperatures [129].

distributed oxide nanoparticles, the Vickers microhardness of this nanostructured W-Y_2O_3 alloy reaches up to 598 HV.

As compared with the oxide strengthening phases, some carbides such as ZrC, TiC, TaC and HfC have much higher melting temperatures. Some carbides can form coherent PB interfaces between the nanosized carbide and the W matrix, which may lead to excellent comprehensive performances. Kurishita et al. reported an UFG W-1.1 %TiC, which exhibited very high bending fracture strength of about 4.4 GPa and an appreciable ductility at RT [56]. These favorable properties imply the potential of other carbides in the tungsten based materials with fine microstructures.

Among these carbide strengthen phases, ZrC and TaC have high melting temperatures (3540 °C and 3900 °C, respectively) which are much higher than that of TiC (3160 °C) and VC (2810 °C). Meanwhile, ZrC has the near equal lattice parameter of $d_{(200)ZrC} \approx d_{(110)W} \approx 0.221$ nm, which might introduce coherent PB interface between W matrix and ZrC phase and significantly increase the PB cohesion. In addition, ZrC can react with oxygen to form stable Zr-C-O or ZrO_2 particles at GBs, purifying GB interfaces, and

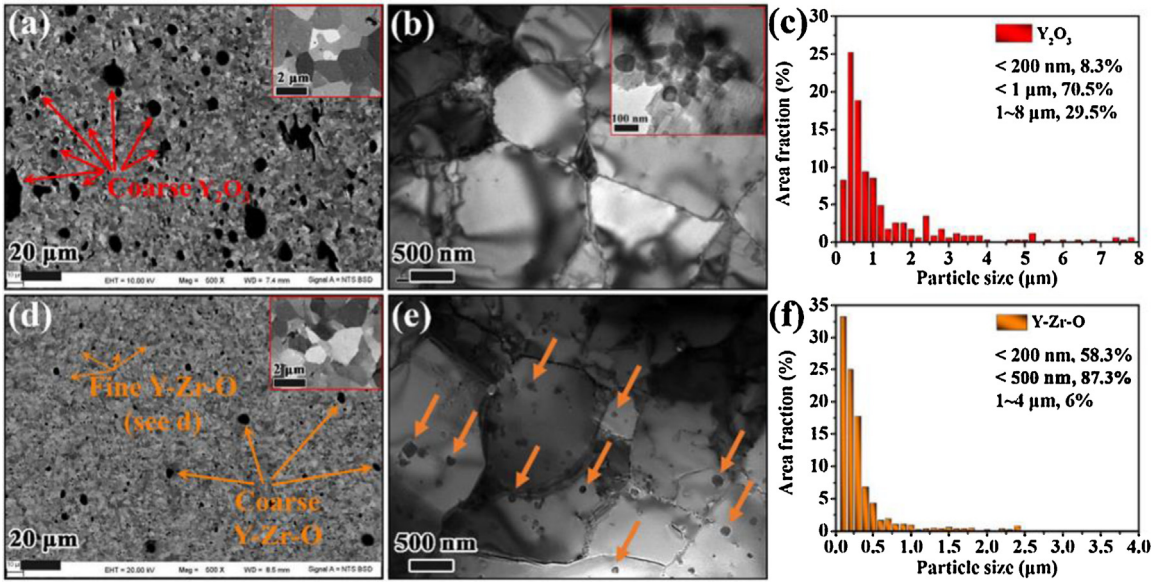

Fig. 34. Distribution of the grain/particle sizes and microstructures of the rolled W-Y_2O_3 (a-c) and W-Zr-Y_2O_3 (d-f) alloys: SEM images of rolled W-Y_2O_3 (a) and rolled W-Zr-Y_2O_3 (d) and insets of high magnification results; TEM images showing the fine tungsten grains in rolled W-Y_2O_3 (b) and rolled W-Zr-Y_2O_3 (e), second phase particles size distributions in rolled W-Y_2O_3 (c) and rolled W-Zr-Y_2O_3 (f). Tensile behaviors of the rolled W-Y_2O_3 and W-Zr-Y_2O_3 at different temperatures [27].

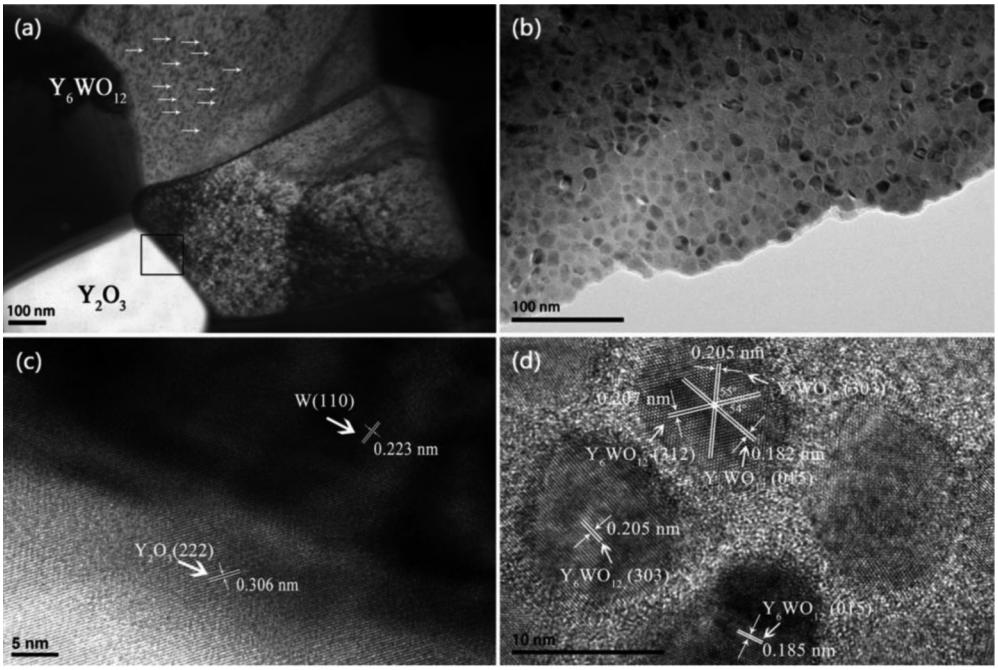

Fig. 35. Low magnification TEM image of the W-Y2O3 alloy prepared by wet chemical method and subsequent SPS, (b) high magnification TEM image showing the oxide particles within W grain, (c) HRTEM image of black square region in panel a, (d) HRTEM image of oxide particles within W grain [186].

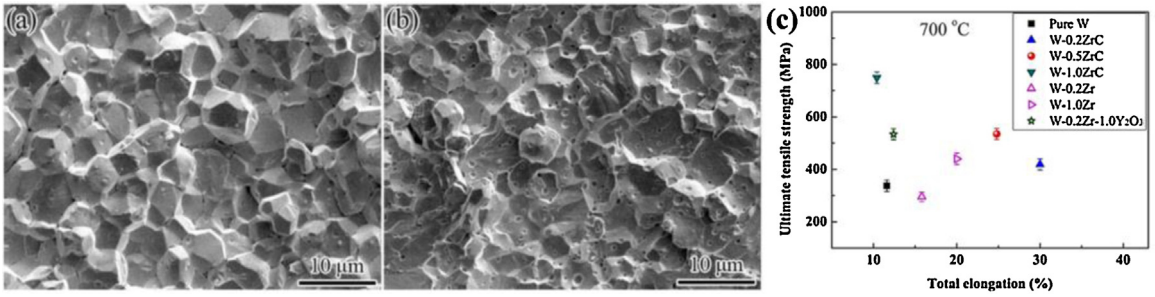

Fig. 36. SEM images showing the representative fracture surfaces of (a) SPS W and (b) SPS W-0.5ZrC after tensile test at RT; (c) Comparison of tensile properties of SPS pure W, W-ZrC, W-Y_2O_3, W-Zr and W-Zr-Y_2O_3 materials tested at 700 °C [79,189].

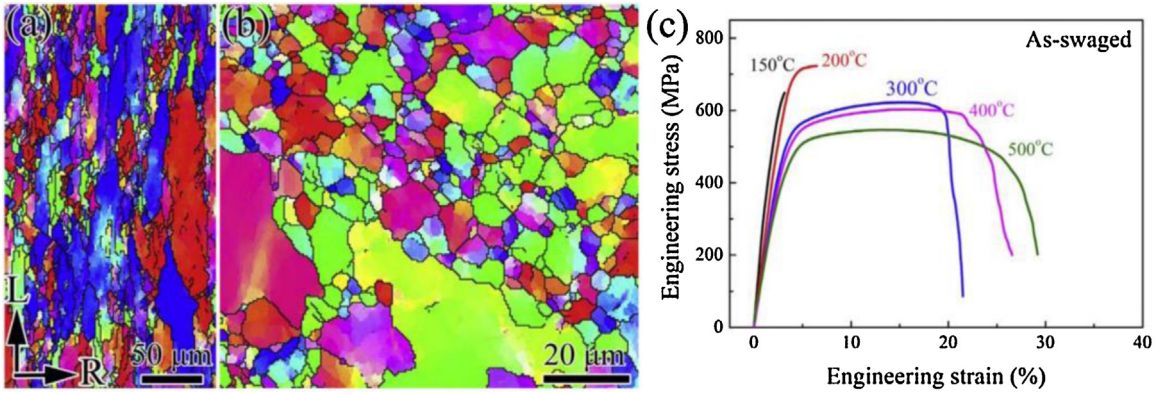

Fig. 37. EBSD images of swaged W-0.5ZrC in the planes (a) parallel to and (b) perpendicular to the longitudinal direction; (c) Tensile engineering stress-strain curves of swaged W-0.5ZrC [190].

thus is beneficial to improve the GB cohesion. Xie et al. fabricated a series of W-(0, 0.2, 0.5, 1.0) %ZrC with average grain size ranging from 2.7 μm to 4.2 μm by using mechanical alloy and SPS sintering [188,189]. At 700 °C, the UTS of SPS pure W and W-(0.2, 0.5, 1.0) % ZrC are 337 MPa, 419 MPa, 535 MPa and 749 MPa, respectively, suggesting enhancements in strength by a small amount of ZrC nano-particle addition. The strength of the SPSed W-0.5ZrC is over 50 % higher than that of SPSed pure W. Meanwhile, the toughness could also be improved by the ZrC addition. The fracture surface of the SPSed pure W is dominated by intergranular fracture (Fig. 36a), implying its weak cohesion strength of GBs. While in the SPSed W-0.5ZrC, both transgranular and intergranular fracture were observed (Fig. 37b), suggesting the enhanced GB cohesion by the addition of ZrC nano-particles. In this SPSed W-0.5ZrC alloy, most of the nano-sized particles were distributed in tungsten grain interior, and a few particles were found at the GBs [79,189]. The average size of these intragranular ZrC particles is smaller than 50 nm. While particles bound to or near the GBs have larger size (> 100 nm) and been indexed to be Zr-C-O or ZrO_2 phase particles, which were formed from ZrC capturing trace impurity oxygen in tungsten during the high-temperature sintering [189]. This purification process would diminish the detrimental effects of oxygen and enhance the GB cohesion through a positive pining effect from the Zr-C-O or ZrO_2 particles. Thus significant enhancements in both strength and ductility were achieved by improving the PB/GB interface structure through adding trace ZrC nano-particles into tungsten.

As described above, thermomechanical treatments (e.g., forging, swaging and rolling) can further optimize the PB/GB interface structure, improve the relative density and enhance low-temperature ductility of tungsten materials. The microstructure of the swaged W-0.5ZrC rod indicates that most GB interface are elongated along the swaging direction (L-direction, Fig. 37a), while the grains in cross section (R-direction) are nearly equiaxed (Fig. 37b). The average grain size of the as-swaged W-0.5ZrC is about 35 μm in swaging direction and 7 μm in cross section, corresponding to an aspect ratio of about 5:1. This kind of GB interfaces will lead to better tensile properties along L direction [190], as shown in Fig. 37c. The as-swaged W-0.5ZrC is brittle at 150 °C and exhibited obvious ductility at 200 °C with a total elongation (TE) of 4.2 %. This result suggests that the DBTT of the as-swaged W-0.5ZrC is about 200 °C, which is about 400 °C lower than that SPSed W-0.5ZrC [190]. With increasing the testing temperature to 500 °C, the UTS of the as-swaged W-0.5ZrC is as high as 547 MPa and the TE is about 28 %.

Compared with the hot swaging, the hot-rolling introduces more homogeneous deformation, which is a better kind of thermomechanical route for fabricating bulk refractory metals through a controllable way for interface decoration. The multistep orthogonal hot-rolling with large deformation of 94 % reduction make more homogeneously prolonged interfaces along rolling direction (RD) and transverse direction (TD), as shown in Fig. 38(a) and (b) [50]. This thin W-0.5ZrC plate has better mechanical properties as compared with that of swaged W-0.5ZrC, as presented in Fig. 39c. For example, the DBTT of this thin W-0.5ZrC plate is about 50–80 °C, much lower than that of the swaged one (150–200 °C) [190]. The corresponding UTS is also improved significantly.

On the base of swaged rods and rolled thin plates, Xie et al. [54,79] fabricated the thick W-0.5ZrC plate (WZC05) with thickness of 8.5 mm, which is suitable for engineering application. The detailed microstructures indicate that there is the coexistence of multiscale interfaces in this rolled thick WZC05 plate. From outer to inner space, in the first layer along the rolling direction, the average length of mother grains is about 10 μm and the width is about 1∼3 μm, which is the micron sized GB interface, as shown in Fig. 39(a). Prolonged mother grains come from the multistep rolling deformation. In the second layer, there are equiaxed sub-grains in the matrix with an average size of about 1 μm, as shown in Fig. 40(a) and (b), which could be considered as the sub-micrometer scale GB interfaces. These sub-grains can be attributed to the deformation and dynamic recrystallization from the precise control of hot rolling processes [54]. For the third layer, the nano-scaled particles, most of them dispersed in tungsten grain interior (Fig. 39c). The second phase particles locating in W grains have an average size of 51 nm (with the fraction of 79 %) covering a range from 29 to 200 nm, as shown in Fig. 40c. While parts of particles (21 %) at W GBs have bimodal distribution which contains relatively small particles with an average particle size of 60 nm ranging from 40 to 200 nm (see Fig. 40d), and a small fraction of large particles with an average particle size of 385 nm ranging from 250 to 400 nm (see Fig. 40d) [54]. The small particles in tungsten grain interior and at GBs are dominantly ZrC, while the large particles are W-Zr-C-O complexes. Therefore, the third layer PB interface is the nanoscale or sub-micrometer scale interface.

The intuitive HRTEM of PB interface shown in Fig. 41(a–e) exhibits a perfect coherent structure between W matrix and ZrC dispersoids, indicating an atomic ordered interface. This coherent PB was further confirmed by simulation results [54]. These coherent PB interfaces can generate, pin down and thus accumulate dislocations within the grains during the deformation process, which effectively raise the strength and simultaneously improve the ductility of alloys. In addition, some particles tightly bounding to the GBs could impede GB sliding. For example, a clubbed ZrC particle locates across two tungsten grains' boundaries, just like a deadbolt tightly locking the two tungsten grains as shown in Fig. 41f, which could obstruct the GB sliding and thus significantly increase the GB cohesion [54].

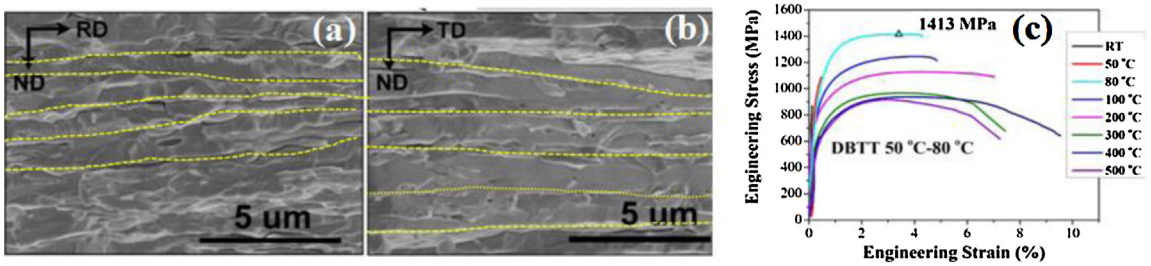

Fig. 38. SEM micrographs of the W-0.5 wt. %ZrC thin plate in normal direction (ND) and transverse direction (TD); Engineering stress-strain curves of W-0.5 wt. %ZrC thin plate specimens tested at different temperatures [50].

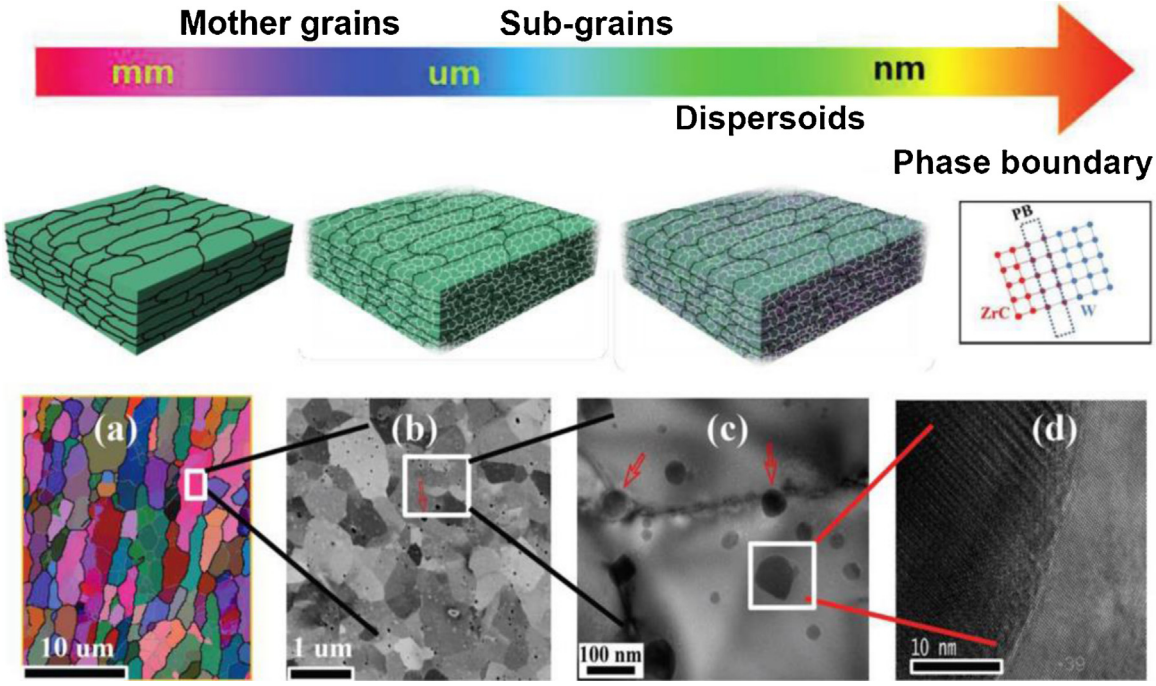

Fig. 39. The microstructure image and sketch of the thick W-0.5 wt. %ZrC plate.

The multi scale interface structure synergistically improves the performance of this WZC05 alloy. The WZC05 exhibits obvious plasticity with a flexural strain of 3% and a fracture stress up to 2.5 GPa at RT, as shown in Fig. 42. At 100 °C, the flexural strain of this WZC05 increases to 5.0 %. That's to say, the DBTT of this WZC05 is about 100 °C, which is lower than the reported value in bulk W and W alloys including hot/cold rolled and HIPed pure W, ODS W and W-Re alloys [180,191–193]. The coherent interfaces between W matrix and the ZrC dispersoids induce the enhanced ductility/strength of this WZC05 alloy. Intuitively, the nanosized PB interfaces in tungsten grain interior can pin and accumulate dislocations, which effectively improve the strength of the alloy. Moreover, there is a channel for the gliding of dislocations along coherent structure between particle and matrix interfaces [194], which would help sustain work hardening and uniform elongation and thus enhance the ability to accommodate plastic deformation.

On the other hand, if the internal boundaries were introduced by addition of some unsuitable dispersion particles, which forbodes the forming of PB interfaces in unstable high-energy states. These unstable PB interfaces would spontaneously coarsen to release the energy under some moderate thermal conditions, which consequently become preferential sites for stress concentration and crack initiation during loading and have serious deterioration of the ductility.

The high strength and good ductility/plasticity lead to an unprecedented thermal shock resistance in this WZC05 alloy. No cracks or melting were observed on the samples even after the thermal bombardment test at an absorbed energy density of ~ 3.3 MJ/m^2, as shown in Fig. 43. The strength of this WZC05 is high enough to resist the stress induced by thermal shocks, and thus to prohibit the formation of cracks. In addition, the good plasticity/ductility can consume the stress energy by deformation to avoid the occurrence of cracking [54].

The multi-scaled interface structure is in favor of irradiation resistance and decreasing the hydrogen retention in this WZC05 alloy. Firstly, the prolonged mother grains can provide an escape channel for the hydrogen in the W matrix and thus decrease the retention, as shown in Fig. 44. After the same irradiation under a high fluence of high flux and low energy deuterium (D) plasma, the retention of D in WZC05 is 9 times lower than that of ITER grade W [79]. At the same time, the fine sub-grains and nanosized particles increase the density of GB and PB interfaces, respectively, which can absorb interstitial defects and annihilate nearby vacancies by re-emitting the interstitial atoms back into the matrix, and then improve the ability of irradiation resistance of this WZC05 alloy. Fig. 45 shows the surface morphologies of different tungsten materials after irradiation under a high fluence of high flux and low energy He plasma: (a) rolled pure W, (b) CVD-pure W and

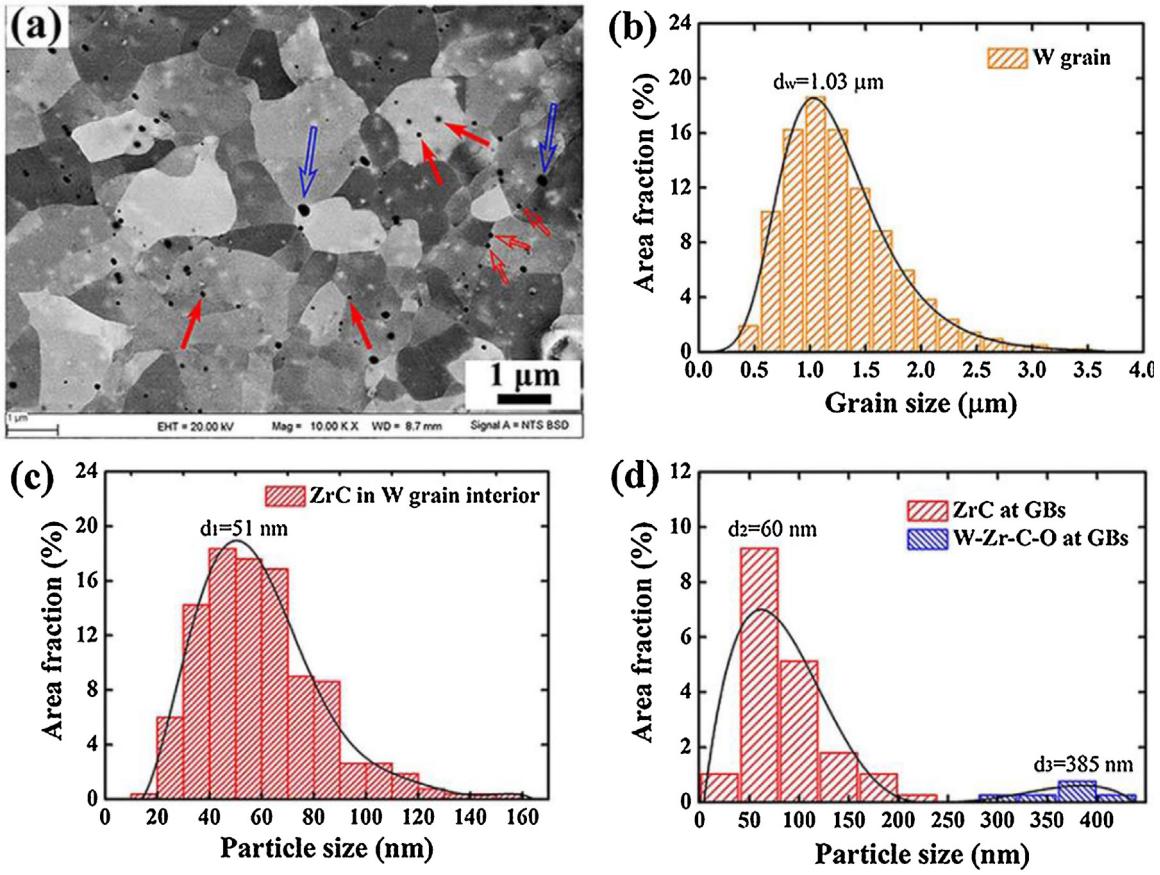

Fig. 40. Distribution of grain/particle sizes and microstructures of WZC05. (a) High magnification BSESEM image showing the tungsten grains possess equiaxed structure. The black contrast dots correspond to the second phase particles. (b) Grain size distribution. (c, d) ZrC and W-Zr-Cx-Oy particles size distribution [54].

(c) W-1 %Y_2O_3 irradiated by 220 eV helium plasma to a dose of 10^{26} atoms/m^2, and (d) rolled pure W, (e) CVD-pure W and (f) W-0.5ZrC (WZC05) irradiated by 620 eV helium plasma to the same dose, and the insets of (a)-(f) show the corresponding cross-section morphologies of irradiation-modified layer in each sample. For the tungsten materials irradiated by 220 eV He ions at 900 °C, surface modifications of all the samples, including the rolled pure W, CVD-pure W, W-1 %Y_2O_3 and WZC05, showed the pin-hole feature, while in the case of 620 eV He ion irradiation at 1000 °C, the pin-hole surface evolved into the coral-like feature except for the WZC05 alloy which remains the pin-hole feature [195]. This result implies the good resistance of WZC05 alloy to high fluence He irradiation. The large amount of GBs and PBs in fine-grained WZC05 alloy provide more nucleation sites for He atom aggregation, resulting in smaller He bubbles, and mitigate the evolution of pin-hole to coral-like structures. The thickness of modified layers on sample surfaces were measured and plotted in Fig. 46. The thickness of modified layers on WZC05 is much lower than that of the pure W, W-1 wt. %La_2O_3, W-1 wt. %Y_2O_3 and W-1 vol. %Y_2O_3, further implying its better resistance to plasma irradiation and erosion.

In addition to ZrC/TiC, nanosized HfC [83,196], TaC [86], SiC [197] and K bubbles [198] can also be used to construct GB/PB interfaces. Miao et al. [86] fabricated the W-0.5 wt. %TaC plate through the same preparation technology with that of the above mentioned thick WZC05 plate. Due to the relatively larger TaC particle size, the produced PB interface density is lower than that of WZC05, resulting in a relatively low pining ability of GBs and an obviously larger grain size in W-0.5 wt. %TaC [86]. In addition, the coarse micron sized Ta-C-O compounds at GBs lead to the stress concentration and then degrade the strength/ductility. Therefore, both the tensile strength and ductility are lower than that of the WZC05 plate. For example, the DBTT of this W-0.5 wt. %TaC plate is about 200 °C and the UTS is about 717 MPa at 250 °C. To solve this problem of particle coarsening, Miao et al. used a special powder preparation route termed "dissolution and re-precipitation" by adding nanosize Ta powder and C powder to form W-Ta-C solid solution and finally to form W-TaC composites, which significantly decreases the particle and grain sizes and increase the interface density [81]. Wang [83] and Zhang et al. [196] employed HfC particles, which has a higher melting temperature, to prepare W-HfC alloys. Because of the high thermal stable interface between the W matrix and the HfC, the W-0.5 wt. %HfC has the best thermal stability (without obvious grain or particle coarsening after high temperature annealing) among W-0.5 wt. %TaC, W-0.5 wt. %HfC and W-0.5 wt. %ZrC plates, as shown in Fig. 47 [87]. But due to the large particles and grains, there are low densities of GB and PB interfaces which offer limited capture sites for irradiation defects in this W-0.5 wt. %HfC. Naturally, the self-heal ability is relative weak, which results in low irradiation resistance as compared with the WZC05 plate [79]. For example, at the same irradiation parameters of D ions, there is a high density of D bubbles on the surface of W-0.5 wt. %HfC with the bubble size of ~1 μm, while in the case of the WZC05 there is just a low density of nanosized D bubbles [79]. Huang et al. prepared a W-K alloy with the intra- and inter-potassium nano-bubble modifying GB interfaces by using an industrially applicable process combining aluminum-potassium-silicon doping and spark plasma sintering, which exhibits desirable strength and remarkable toughness, as well as high thermal-shock resistance [198].

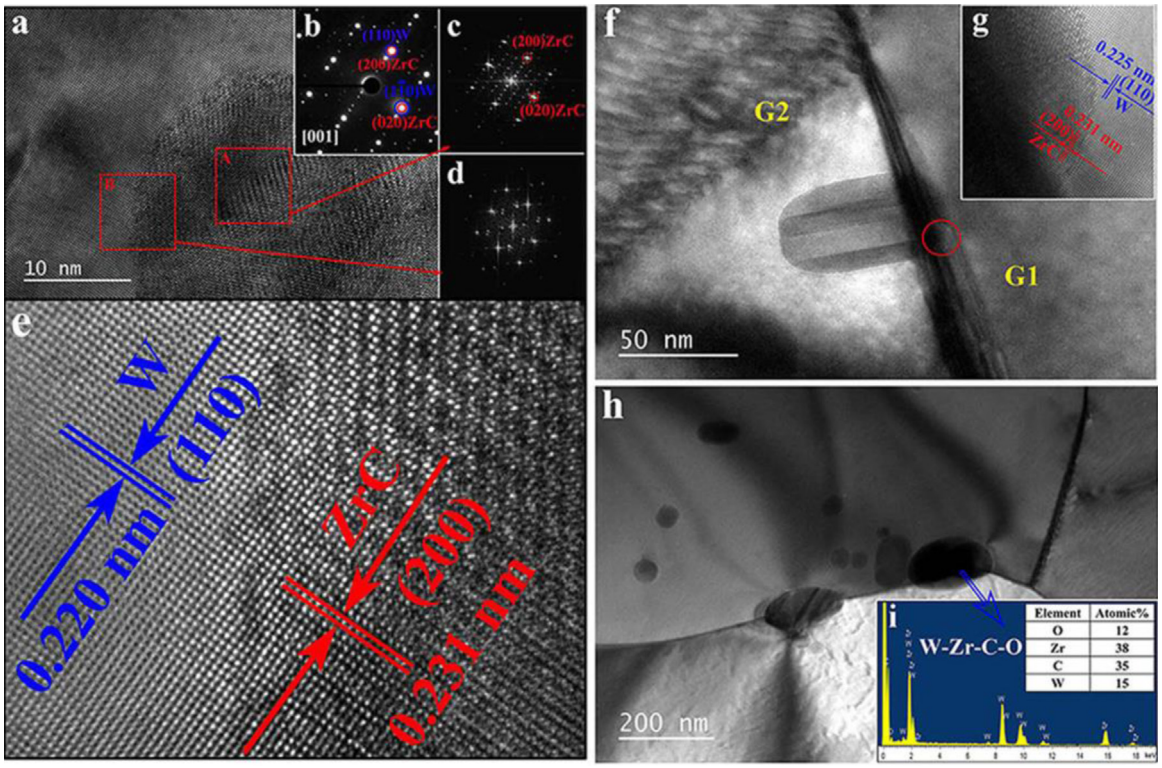

Fig. 41. Detailed analysis of the interface structure between W matrix and second phase particlesin WZC. (a) HRTEM image of W matrix and ZrC phase (intragranular) as viewed along [001]. (b) The SAEDP revealing the particle with a face centered cubic structure. (c) Fast Fourier transform (FFT) pattern of selected red square area A on ZrC. (d) FFT pattern of selected red square area B at interface area between W and ZrC. It is clear that the particle-matrix PBs have coherent structure like showing in high magnification (e). (f) TEM image showing a deadbolt shaped ZrC particle (intergranular) tightly locking two tungsten grains (G1 represents the right one and G2 represents the left one). (g) Semi-coherent structure appears between the ZrC dispersoid and G2. (h) Some relatively large particles locating at GBs oftungsten contain W, Zr, C and O elements through (i) EDX analysis [54].

5. Other interfaces

In addition to the above mentioned grain refinement, alloying, doping and dispersion strengthening processes to control the interfaces of refractory alloys, since a decade, a promising method of toughening refractory metals, such as carbon nano-tubes (CNTs) doped tungsten alloys [199,200], and tungsten fiber reinforcement tungsten composites termed tungsten fiber-reinforced tungsten (W_f /W) [201–213], has been actively pursued. Tungsten fibers are embedded in a tungsten matrix where a proper interface has to be introduced to prevent chemical reaction between tungsten fibers and the matrix, because in the bared W_f /W the interface cohesion is weak and the interfacial debonding often occurs under tensile stress, as shown in Fig. 48 [203,213]. The increase in toughness is achieved through a couple of non-plastic energy dissipation mechanisms such as matrix cracking and interfacial debonding followed by frictional sliding/pull-out of the fibers while the primary crack is bridged by mostly deforming fibers [210,211]. To maximize the energy dissipation, the interfaces need to be engineered by coating which can withstand thermal exposure during service. Du et al. investigated the effects of different coated interfaces for W_f/W composite: Cu/W multilayer, ZrO_x/Zr multilayer, Er/W multilayer, ZrO_x/W bilayer and C/W dual layer [210]. These coatings were effective in utilizing energy dissipation by controlled interfacial debonding and sliding to achieve apparent toughness. The results indicated that the ZrO_x/W bilayer interface is the best choice for W_f/W composite. In addition, the fiber configuration (actually the interface configuration) also plays an important role in W_f /W composites. The single direction of W fibers can enhance the fracture energy of tungsten matrix once the extrinsic toughening mechanisms of fiber pullout and plastic deformation were triggered, but they will lead to the obvious anisotropy of mechanical properties [206]. Woven tungsten wire meshes as reinforcement in the composites could avoid the anisotropy. The W_f/W composites with tungsten wire meshes coated by zirconia film (ZrO_x) were fabricated using spark plasma sintering method at different temperatures [212]. Fig. 49a and c shows the SEM results of the W_f /W composite specimen after the SPS processes at 1400 °C and 1700 °C, respectively. The zirconia coating remained indeed mostly undamaged after 1400 °C sintering as shown in Fig. 49b. In contrast, the coating thickness was considerably reduced (from 1 μm to 0.7 μm in average) after sintering at 1700 °C as shown in Fig. 49d. After the high heat flux loading with the intense hydrogen bombardment, a discernible damage of the matrix surface is observed due to the significant erosion of the GBs. On the contrary, zirconia coating seems to have survived the heat loads without any notable damage or overall cracking but slight erosion. Therefore, under the extreme environment, the zirconia coating interfaces are stable, which is favor of reinforcing the W_f/W composites [213,214]. In addition, nanoporous also can increase the interfaces and then modify the performance of refractory metals, for example, the structure of nanoporous tungsten has a high activation energy for surface diffusion, which contributes to its extremely high thermal stability [215].

Recently, refractory high-entropy alloys (RHEAs) with multi-principle elements and refractory metals were first reported in 2010 [216], such as WNbMoTa and WNbMoTaV alloys exhibiting high yield strength at temperatures up to 1600 °C and the strong resistance to high temperature softening, as compared to the superalloys [216,217]. Although RHEAs have excellent strength at high temperatures, disadvantages such as poor room temperature ductility, poor oxidation resistance and the relatively high density are

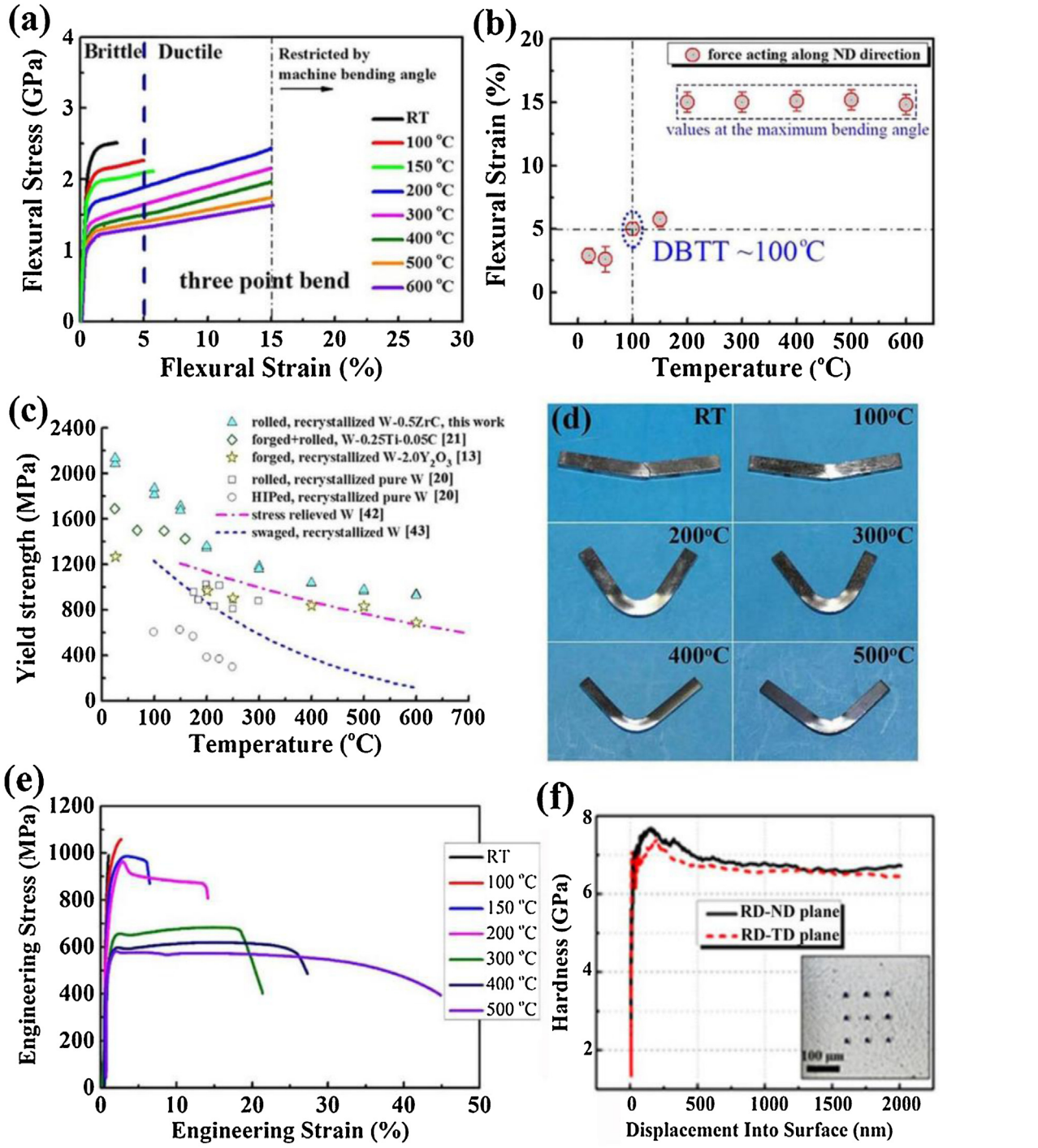

Fig. 42. Mechanical behaviors of WZC05. (a) Flexural stress-strain curves of WZC05 tested at different temperatures, note that values larger than a flexural strain of 15 % are not accurate because of the limited bending angle of the machine. (b) Flexural strain of the tested samples versus temperature, DBTT is about 100 °C. (c) Temperature dependence of the yield strength (YS) of the WZC05 plate in comparison with available literature data. The YS of WZC05 is the highest among the all reported bulk W alloys. (d) Optical images of WZC05 samples after tests. (e) Tensile engineering stress-strain curves of WZC05 tested at various temperatures [54].

also inherited. Senkov et al. reported that [218,219] replacement of heavier W, Mo, and V with lighter Hf, Zr, and Ti allowed the formulation of a new refractory alloy, TaNbHfZrTi, with a reduced density of ρ =9.94 g/cm^3 and excellent compression ductility at room temperature. The good ductility of this TaNbHfZrTi alloy is probably due to the twin GB interfaces, which effectively reduce stress localization along grain boundaries. Schuh et al. found that [220] a nanocrystalline TaNbHfZrTi alloy with high density GB interfaces produced by High-pressure torsion shows significant increase in tensile strength (1900 MPa) and remain fairly ductile with a total elongation to failure of 7.9 %. Therefore, it can be concluded that the mechanical performance of the new type of RHEAs can also be tailored by controlling their interface structures.

6. Future development and research

The interface is a unique lattice defect with many possible structures and energy states, which plays a very important role

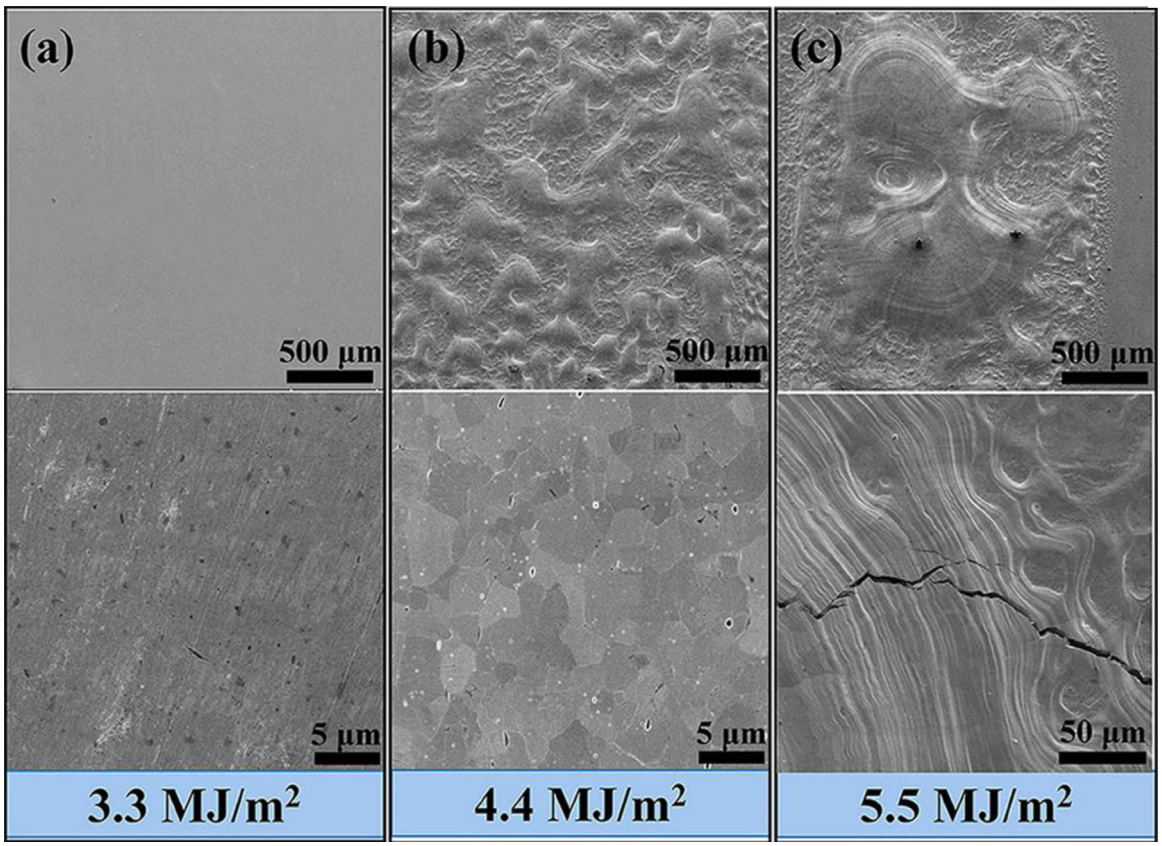

Fig. 43. SEM images showing the thermal shock resistance properties of WZC. (a) No cracks were detected on the samples with absorbed energy density (AED) ~ 3.3 MJ/m^2. (b) There is still no crack with AED ~ 4.4 MJ/m^2 despite the surface melting, which should benefit from the extraordinary plasticity and high strength. (c) Melting and cracks appear simultaneously with AED ~ 5.5 MJ/m^2 and the wave-like stripes along with the crack illustrate the good ductility and plasticity of WZC alloy from other side [54].

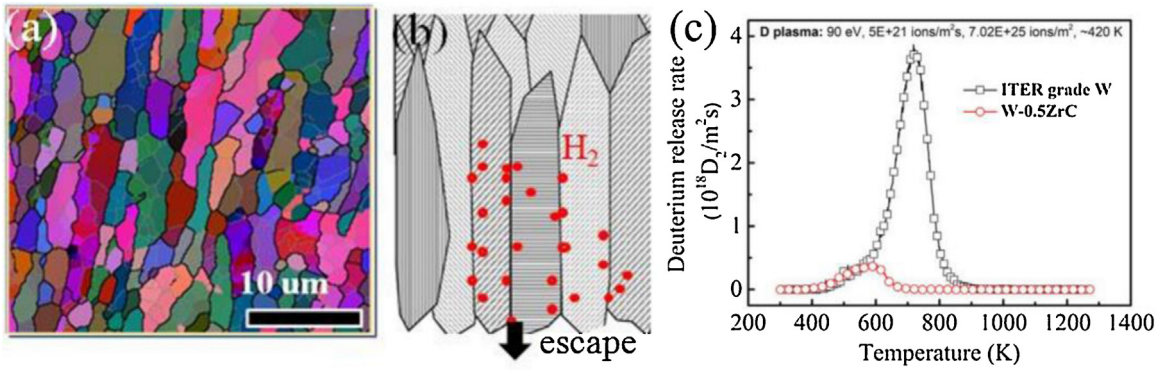

Fig. 44. The mother grain structure (a); the state of H in columnar grain structure (sktech) (b); the thermal desorption spectrometry of deuterium in ITER grade W and W-0.5ZrC specimen (c). The irradiation temperature is 420 K [79].

in determining the performance of materials. With the increasing awareness of interface effects on material performances, the processing-structure-performance relationships will be upgraded with the addition of the interface structures, of which there are numerous variants [16]. Research in the design, fabrication, microstructures and properties of interfaces at the different scales provides new challenges and opportunities for experimental, analytical and simulation studies. During the recent decades, the improvement of performance of refractory metals and alloys by controlling the interfaces have enriched the knowledge base and helped to show the way to high performance refractory metals and alloys for various potential applications. The properties and performances of refractory materials are determined not only by the number of interfaces but also by their physical and chemical states such as the structure, distribution and composition as well as their synergistic effects. From the above results, it can be concluded that the formation of elaborately decorated interfaces is a key to enhance performances of materials. These performances include the physical and chemical properties such as mechanical, thermal properties and irradiation and corrosion resistance.

Although the performances of refractory metals have been significantly improved by controlling interfaces, there are still lots of open questions needing to be further discussed, analyzed, debated and explored. These questions focused on the following issues: i) interface types and features (i.e., the high angle GBs, low angle GBs, twin boundaries and coherent/semi-coherent/incoherent GB/PB interfaces), ii) how to to judge an interface and how to deter-

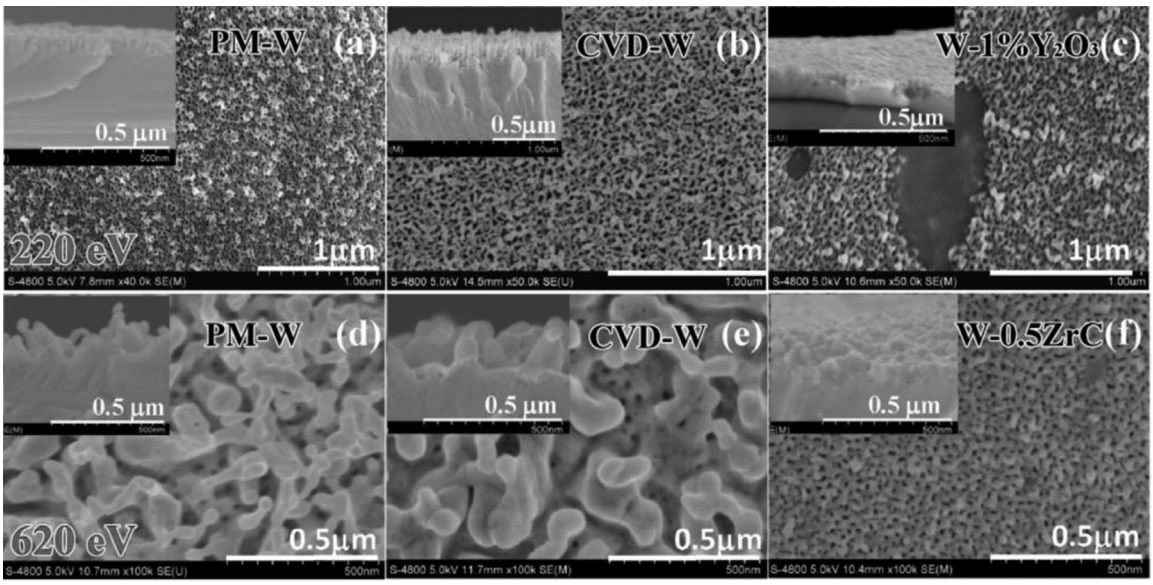

Fig. 45. The surface morphologies of (a) pure W, (b) CVD-W, (c) W-1.0 % Y_2O_3 irradiated by 220 eV He^+ at about 900 °C, and (d) pure W, (e) CVD W and (f) W-0.5ZrC irradiated by 620 eV He^+ at 1000 °C to a same fluence of 1×10^{26} atoms/m^2 [195].

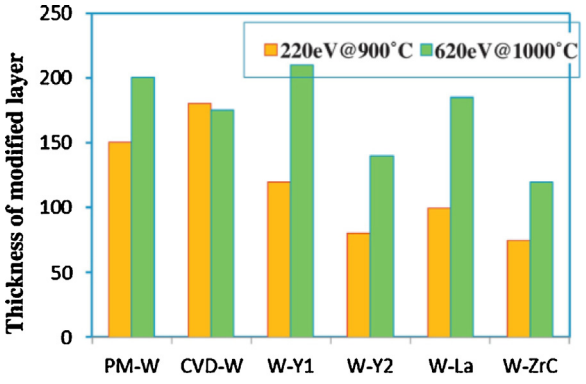

Fig. 46. Thickness of modified layers in various tungsten materials under the He^+ irradiation of 220 eV at 900 °C and 620 eV at 1000 °C [195].

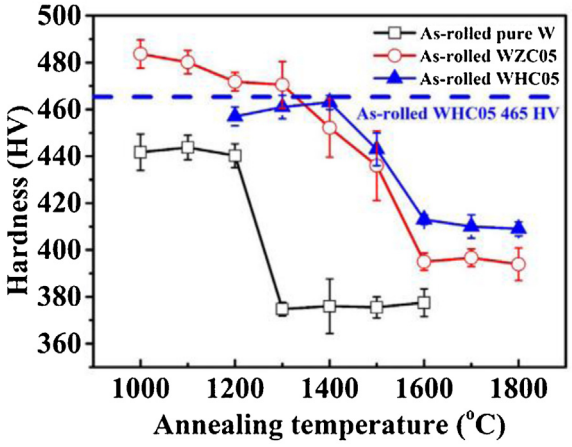

Fig. 47. The annealing temperature dependence of hardness of hot rolled pure W, W-ZrC and W-HfC plates [87].

mine what makes one interface better than another, in other words, how to build different types of interfaces according to needs, iii) the correlation and mutual influence between different types of interfaces and iv) the quantitative relationship between special interfaces and the material performances. As a matter of course, further innovation in processing techniques for tailoring the interfaces is crucial for the future development of refractory metals and alloys with high performances, especially for advancing the fundamental understanding of relationships between the interface structures/states and performances. The construction of low-energy ordered interfaces through a "top-down" route using extreme deformation treatments on single

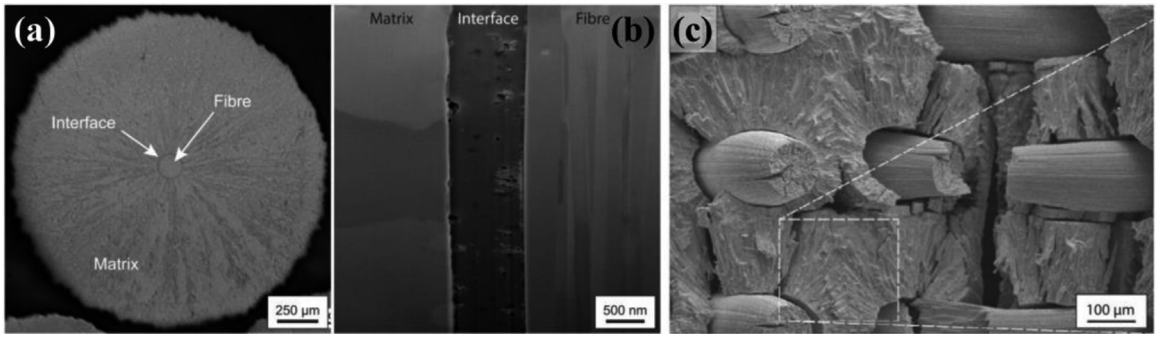

Fig. 48. (a) Metallographic cross-sections of a single-fibre W_f/W composite consisting of a single coated tungsten wire which is embedded in a tungsten matrix formed by chemical vapour deposition. (b) Cross-section of the whole sample: a longitudinal section along the fibre axis showing the interface between fibre and matrix in detail [203]. (c) The fracture surface of the W_f/W composite (with the tungsten fibre array) [213].

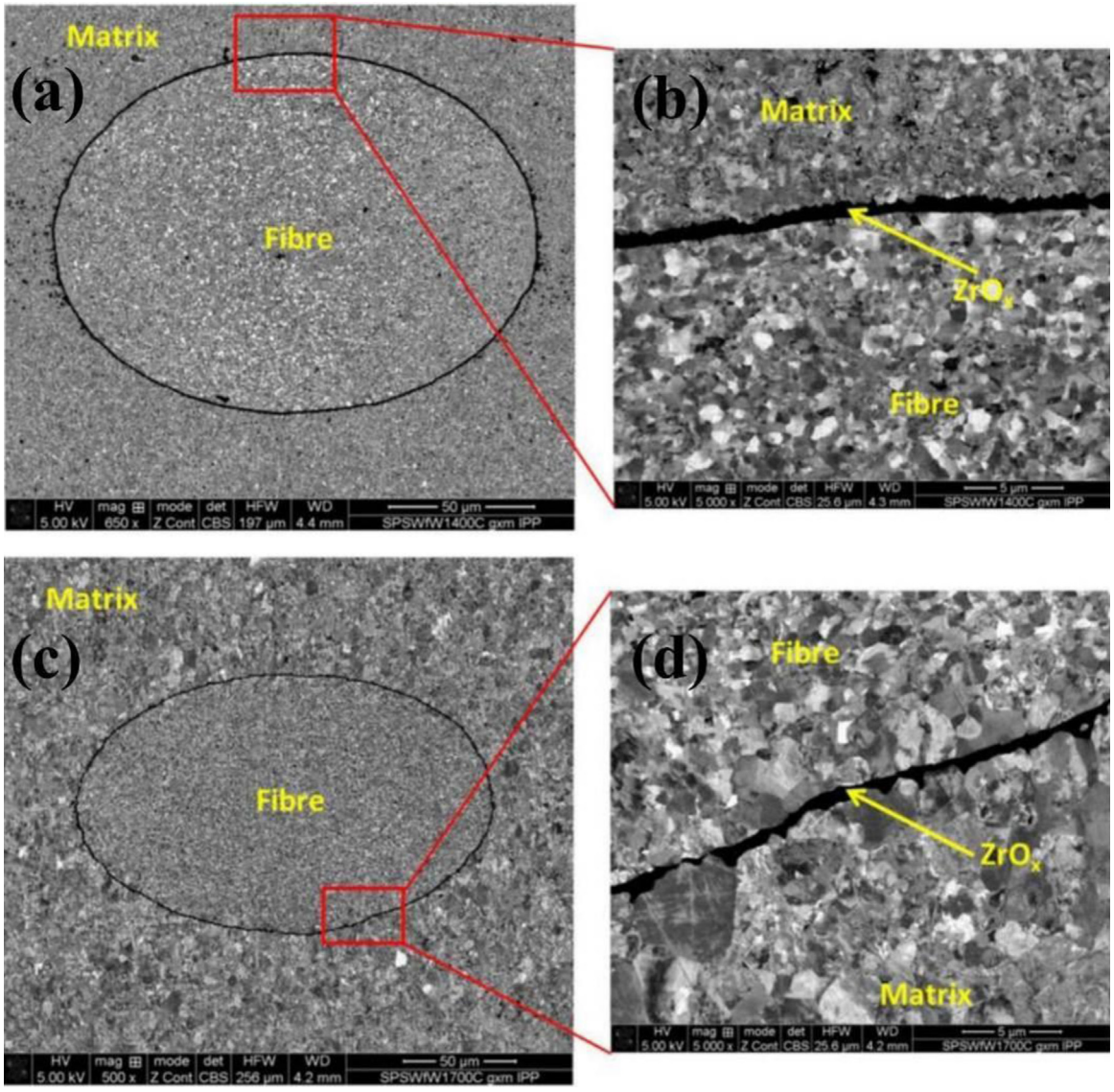

Fig. 49. SEM microstructural image of the Wf/W composite specimen after SPS process at (a), (b) 1400 °C and (c), (d) 1700 °C [212].

phase refractory metals or multi-phase refractory alloys could inspire the development of hybrid processing techniques with scale-up capability for refractory metal materials. For "bottom-up" method to fabricate bulk nanocrystalline refractory alloys with high thermal stabilities, it is the key to design and construct the low energy ordered GB/PB interfaces to synergistically stabilize the nanostructure, because the instability of interfaces is mainly responsible for structure and performance instabilities. This technique is promising for fabricating bulk nanograined refractory alloys.

For the traditional alloying principles in the interface architecture strategy of refractory alloys, especially for the second phase particle dispersion strengthened refractory materials, the density of GB/PB interfaces should be further increased. In current commercial refractory alloys such as the W-La_2O_3 alloys, the second phase particle size is relatively large (even in micron dimensions). If the second-phase particles could be refined to nanoscale, e.g., to 10 nm or even smaller, the mechanical properties and resistance to thermal loads and irradiation might be further improved due to the increased particle-matrix interfaces.

Acknowledgements

This work was financially supported by the National Natural Science Foundation of China (Grant Nos.: 51771184, 11735015, 51801203, 51771181), the Natural Science Foundation of Anhui Province (Grant No. 1808085QE132), the Open Project of State Key Laboratory of Environment friendly Energy Materials (18kfhg02), a fund from the Science and Technology on Surface Physics and Chemistry Laboratory (Grant No. JZX7Y201901SY00900103) and the Innovation Center of Nuclear Materials for National Defense Industry.

References

[1] H. Bolt, V. Barabash, W. Krauss, J. Linke, R. Neu, S. Suzuki, N. Yoshida, ASDEX Upgrade Team, J. Nucl. Mater. 329–333 (2004) 66–73.
[2] M. Kawai, M. Furusaka, K. Kikuchi, H. Kurishita, R. Watanabe, J. Li, K. Sugimoto, T. Yamamura, Y. Hiraoka, K. Abe, A. Hasegawa, M. Yoshiie, H. Takenaka, K. Mishima, Y. Kiyanagi, T. Tanabe, N. Yoshida, T. Igarashi, J. Nucl. Mater. 318 (2003) 38–55.
[3] J.H. Perepezko, Science 326 (2009) 1068.

[4] D.M. Dimiduk, J.H. Perepezko, MRS Bull. 28 (2003) 639–645.
[5] M.S. El-Genk, J.M. Tournier, J. Nucl. Mater. 340 (2005) 93–112.
[6] M.S. Wechsler, C. Lin, W.F. Sommer, L.L. Daemen, P.D. Ferguson, J. Nucl. Mater. 244 (1997) 177–184.
[7] Y. Nemoto, A. Hasegawa, M. Satou, K. Abe, J. Nucl. Mater. 283–287 (2000) 1144–1147.
[8] Y. Ishijima, H. Kurishita, H. Arakawa, M. Hasegawa, Y. Hiraoka, T. Takida, K. Takebe, Mater. Trans. 46 (2005) 568–574.
[9] J. Wadsworth, T.G. Nieh, J.J. Stephens, Int. Mater. Rev. 33 (1988) 131–150.
[10] D. Sturm, M. Heilmaier, J.H. Schneibel, P. Jéhanno, B. Skrotzki, H. Saage, Mater. Sci. Eng. A 463 (2007) 107–114.
[11] B.V. Cockeram, Metall. Mater. Trans. 40 (2009) 2843–2860.
[12] Z. Dong, N. Liu, W.Q. Hu, Z.Q. Ma, C. Li, C.X. Liu, Q.Y. Guo, Y.C. Liu, J. Mater. Sci. Technol. 36 (2020) 118–127.
[13] E. Botcharov, J. Freudenberger, L. Schultz, Acta Mater. 54 (2006) 3333–3341.
[14] C. Koch, R. Scattergood, K. Darling, J. Semones, J. Mater. Sci. 43 (2008) 7264–7272.
[15] Y. Chen, Y. Liu, F. Khatkhatay, C. Sun, H. Wang, X. Zhang, Scr. Mater. 67 (2012) 177–180.
[16] X.L. Ma, C.X. Huang, J. Moering, M. Ruppert, H.W. Hoppel, M. Goken, J. Narayan, Y.T. Zhu, Acta Mater. 116 (2016) 43–52.
[17] S. Wurster, N. Baluc, M. Battabyal, T. Crosby, J. Du, C. García-Rosales, A. Hasegawa, A. Hoffmann, A. Kimura, H. Kurishita, R.J. Kurtz, H. Li, S. Noh, J. Reiser, J. Riesch, M. Rieth, W. Setyawan, M. Walter, J.-H. You, R. Pippan, J. Nucl. Mater. 442 (2013) S181–S189.
[18] J. Luo, V.K. Gupt, D.H. Yoon,Appl. Phys. Lett. 87 (2005), 231902.
[19] V. Randle, Acta Mater. 52 (2004) 4067–4081.
[20] D.B. Bober, M. Kumar, T.J. Rupert, Acta Mater. 86 (2015) 43–54.
[21] M.E. Launey, R.O. Ritchie, Adv. Mater. 21 (20) (2009) 2103–2110.
[22] Z. Wang, A. Kulkarni, S. Deshpande, T. Nakamura, H. Herman, Acta Mater. 51 (2003) 5319–5334.
[23] H. Gleiter, Acta Mater. 48 (2000) 1–29.
[24] H. Gleiter, Prog. Mater. Sci. 33 (1989) 223–315.
[25] M.A. Meyers, A. Mishra, D.J. Benson, Prog. Mater. Sci. 51 (2006) 427–556.
[26] H. Fujita, K. Yuyama, X.C. Li, Y. Hatano, T. Toyama, M. Ohta, K. Ochiai, N. Yoshida, T. Chikada, Y. Oya,Phys. Scr. T167 (2016), 014068.
[27] Z.M. Xie, R. Liu, T. Zhang, Q.F. Fang, C.S. Liu, X. Liu, G.N. Luo, Mater. Des. 107 (2016) 144–152.
[28] T. Hirai, G. Pintsuk, J. Linke, M. Batilliot, J. Nucl. Mater. 390-391 (2009) 751–754.
[29] B.V. Cockeram, R.W. Smith, T.S. Byun, L.L. Snea, J. Nucl. Mater. 393 (2009) 12–21.
[30] E.G. Fu, A. Misra, H. Wang, L. Shao, X. Zhang, J. Nucl. Mater. 407 (2010) 178–188.
[31] W.Z. Han, M.J. Demkowicz, N.A. Mara, E.G. Fu, S. Sinha, A.D. Rollett, Y.Q. Wang, J.S. Carpenter, I.J. Beyerlein, A. Misra, Adv. Mater. 25 (2013) 6975–6979.
[32] S. Yao, Q.S. Jin, Y.H. Li, H.B. Zhou, Y. Zhang, G.H. Lu, Nucl. Instrum. Methods Phys. Res. B 393 (2017) 190.
[33] S.S. Pan, X. Zhang, W. Lu, S.F. Yu,Nanotechnology 30 (2019), 065605.
[34] X.Y. Li, G.H. Duan, Y.C. Xu, Y.G. Zhang, W. Liu, C.S. Liu, Y.F. Liang, J.L. Chen, G.N. Luo,Nucl. Fusion 57 (2017), 116055.
[35] C. González, M. Panizo-Laiz, N. Gordillo, C.L. Guerrero, E. Tejado, F. Munnik, P. Piaggi, E. Bringa, R. Iglesias, J.M. Perlado, R. González-Arrabal,Nucl. Fusion 55 (11) (2015), 113009.
[36] X.Y. Li, W. Liu, Y.C. Xu, C.S. Liu, Q.F. Fang, B.C. Pan, J.L. Chen, G.N. Luo, Z.G. Wang,Nucl. Fusion 53 (2013), 123014.
[37] K. Lu,Nat. Rev. Mater. 10 (2016), 160109.
[38] T. Nagasaka, T. Muroga, K. Fukumoto, H. Watanabe, M.L. Grossbeck, J.M. Chen, Nucl. Fusion 46 (2006) 618–625.
[39] H. Saage, M. Kruger, D. Sturm, M. Heilmaier, J.H. Schneibel, E. George, L. Heatherly, C. Somsen, G. Eggeler, Y. Yang, Acta Mater. 57 (2009) 3895–3901.
[40] T. Loewenhoff, A. Bürger, J. Linke, G. Pintsuk, A. Schmidt, L. Singheiser, C. Thomser,Phys. Scr. T145 (2011), 014057.
[41] J.W. Coenen, V. Philipps, S. Brezinsek, G. Pintsuk, I. Uytdenhouwen, M. Wirtz, A. Kreter, K. Sugiyama, H. Kurishita, Y. Torikai, Y. Ueda, U. Samm, The TEXTORTeam,Nucl. Fusion 51 (2011), 113020.
[42] S. Wurster, B. Gludovatz, A. Hoffmann, R. Pippan, J. Nucl. Mater. 413 (2011) 166.
[43] S. Wurster, B. Gludovatz, R. Pippan, Int. J. Refract. Metal. Hard Mater. 28 (2010) 692.
[44] B.B. Jiang, A.D. Tu, H. Wang, H.C. Duan, S.Y. He, H.Q. Ye, K. Du, Acta Mater. 155 (2018) 56–68.
[45] O. El-Atwani, S. Gonderman, M. Efe, G.D. Temmerman, T. Morgan, K. Bystrov, D. Klenosky, T. Qiu, J.P. Allain,Nucl. Fusion 54 (2014), 083013.
[46] H. Kurishita, H. Arakawa, S. Matsuo, T. Sakamoto, S. Kobayashi, K. Nakai, G. Pintsuk, J. Linke, S. Tsurekawa, V. Yardley, K. Tokunaga, T. Takida, M. Katoh, A. Ikegaya, Y. Ueda, M. Kawai, N. Yoshida, Mater. Trans. 54 (2013) 456.
[47] Q. Wei, Z.L. Pan, X.L. Wu, B.E. Schuster, L.J. Kecskes, R.Z. Valiev, Acta Mater. 59 (2011) 2423–2436.
[48] G. Valles, C. González, I. Martin-Bragado, R. Iglesias, J.M. Perlado, A. Rivera, J. Nucl. Mater. 457 (2015) 80–87.
[49] Z.M. Wu, J. Zhang, J. Zhang, J.C. Huang, Y. Fan, X.H. Xu, Y.B. Zhao, J.L. Zhu, C.Q. Jin, P. Wang, E.G. Fu,Nucl. Fusion 59 (10) (2019), 106050.
[50] H.L. Ding, Z.M. Xie, Q.F. Fang, T. Zhang, Z.J. Cheng, Z. Zhuang, X.P. Wang, C.S. Liu, Mater. Sci. Eng. A 716 (2018) 268–273.
[51] H.W. Deng, Z.M. Xie, Y.K. Wang, R. Liu, T. Zhang, X.P. Wang, Q.F. Fang, C.S. Liu, Mater. Sci. Eng. A 715 (2018) 117–125.
[52] G.M. Song, Y.J. Wang, Y. Zhou, Int. J. Refract. Metal. Hard Mater. 21 (2003) 1–12.
[53] M. Zibrov, M. Mayer, L. Gao, S. Elgeti, H. Kurishita, Yu. Gasparyan, A. Pisareva, J. Nucl. Mater. 463 (2015) 1045–1048.
[54] Z.M. Xie, R. Liu, S. Miao, X.D. Yang, T. Zhang, X.P. Wang, Q.F. Fang, C.S. Liu, G.N. Luo, Y.Y. Lian, X. Liu, Sci. Rep. 5 (2015) 16014.
[55] M.V. Aguirre, A. Martín, J.Y. Pastor, J. LLorca, M.A. Monge, R. Pareja, J. Nucl. Mater. 417 (2011) 516–519.
[56] H. Kurishita, S. Matsuo, H. Arakawa, T. Sakamoto, S. Kobayashi, K. Nakai, T. Takida, M. Kato, M. Kawai, N. Yoshida, J. Nucl. Mater. 398 (2010) 87–92.
[57] G. Pintsuk, H. Kurishita, J. Linke, H. Arakawa, S. Matsuo, T. Sakamoto, S. Kobayashi, K. Nakai,Phys. Scr. T145 (2011), 014060.
[58] R. Jamaati, M.R. Toroghinejad, Mater. Sci. Eng. A 527 (2010) 4146–4151.
[59] S.J. Zheng, S. Shao, J. Zhang, Y.Q. Wang, M.J. Demkowicz, I.J. Beyerlein, N.A. Mara,Appl. Phys. Lett. 105 (2014), 111901.
[60] W.Z. Han, M.J. Demkowicz, E.G. Fu, Y.Q. Wang, A. Misra, Acta Mater. 60 (2012) 6341–6351.
[61] J.S. Carpenter, S.J. Zheng, R.F. Zhang, S.C. Vogel, I.J. Beyerlein, N.A. Mara, Philos. Mag. 93 (2013) 718.
[62] L.F. Zeng, R. Gao, Q.F. Fang, X.P. Wang, Z.M. Xie, S. Miao, T. Hao, T. Zhang, Acta Mater. 110 (2016) 341–351.
[63] L.F. Zeng, C.P. You, C.M. Wang, X.H. Zhang, T.X. Liang,Mater. Lett. 261 (2020), 127020.
[64] L.F. Zeng, C.P. You, N. Hong, X.H. Zhang, T.X. Liang,Adv. Eng. Mater. (2020), 1901359.
[65] H.W. Deng, Z.M. Xie, M.M. Wang, Y. Chen, R. Liu, J.F. Yang, T. Zhang, X.P. Wang, Q.F. Fang, C.S. Liu, Y. Xiong,Mater. Sci. Eng. A 774 (2020), 138925.
[66] C. Ren, Z.Z. Fang, M. Koopman, B. Butler, J. Paramore, S. Middlemas, Int. J. Refract. Metal. Hard Mater. 75 (2018) 170–183.
[67] H. Li, S. Wurster, C. Motz, L. Romaner, C. Ambrosch-Draxl, R. Pippan, Acta Mater. 60 (2012) 748–758.
[68] P.B. Hirsch, Proceedings of the fifth international conference on crystallography, in: Proc. 5th Int. Conf. Crystallography, Cambridge University, 1960.
[69] V. Vitek Groger, Acta Mater. 56 (2008) 5401–5411.
[70] W. Cheng, W. Jian, H. Yuan, M. Tsai, Y. Zhu, J. Mater. Res. 28 (2013) 1820–1826.
[71] B. Gludovatz, S. Wurster, T. Weingartner, A. Hoffmann, R. Pippan, Philos. Mag. 91 (2011) 3006–3020.
[72] F. Funkenbusch, D. Lee, Metall. Trans. A 10 (1979) 1085.
[73] D. Joshi, Metall. Trans. A 1 (1970) 2543–2546.
[74] B. Liu, B. Shen, Acta Metal. 30 (1982) 1197–1202.
[75] H. Kurishita, S. Matsuo, H. Arakawa, T. Sakamoto, S. Kobayashi, K. Nakai, H. Okano, H. Watanabe, N. Yoshida, Y. Torikai, Y. Hatano, T. Takida, M. Kato, A. Ikegaya, Y. Ueda, M. Hatakeyama, T. Shikama,Phys. Scr. T159 (2014), 014032.
[76] K. Leitner, P.J. Felfer, D. Holec, J. Cairney, W. Knabl, A. Lorich, H. Clemens, S. Primig, Mater. Des. 135 (2017) 204.
[77] T. Watanaba, S. Tsurekawa, Acta Mater. 47 (1999) 4171.
[78] T. Zhang, Z.M. Xie, S. Miao, Q.F. Fang, C.S. Liu, Acta Metall. Sin. 54 (2018) 831.
[79] R. Liu, Z.M. Xie, X. Yao, T. Zhang, X.P. Wang, T. Hao, Q.F. Fang, C.S. Liu, Nucl. Mater. Energy 16 (2018) 191–206.
[80] Z.M. Xie, S. Miao, T. Zhang, R. Liu, X.P. Wang, Q.F. Fang, T. Hao, Z. Zhuang, C.S. Liu, Y.Y. Lian, X. Liu, L.H. Cai, J. Nucl. Mater. 501 (2018) 282–292.
[81] S. Miao, Z.M. Xie, L.F. Zeng, T. Zhang, X.P. Wang, Q.F. Fang, C.S. Liu, G.N. Luo, X. Liu, Fusion Eng. Des 125 (2017) 490–495.
[82] C. Yin, D. Terentyev, T. Pardoen, A. Bakaeva, R. Petrov, S. Antusch, M. Vilémová, J. Matějíček, T. Zhang, Int. J. Refract. Metal. Hard Mater. 75 (2018) 153–162.
[83] K.E. Rea, V. Viswanathan, A. Kruize, J.Th.M. De Hosson, S. O'Dell, T. McKechnie, S. Rajagopalan, R. Vaidyanathan, S. Seal, Mater. Sci. Eng. A 477 (2008) 350–357.
[84] Z.M. Xie, S. Miao, R. Liu, L.F. Zeng, T. Zhang, Q.F. Fang, C.S. Liu, X.P. Wang, Y.Y. Lian, X. Liu, L.H. Cai, J. Nucl. Mater. 496 (2017) 41–53.
[85] S. Miao, Z. Xie, T. Zhang, X. Wang, Q.F. Fang, C.S. Liu, G. Luo, X. Liu, Y. Lian, Mater. Sci. Eng. A 671 (2016) 87–95.
[86] S. Miao, Z. Xie, X. Yang, R. Liu, R. Gao, T. Zhang, X. Wang, Q. Fang, C. Liu, G. Luo, Int. J. Refract. Metal. Hard Mater. 56 (2016) 8–17.
[87] Y.K. Wang, Z.M. Xie, M.M. Wang, H.W. Deng, J.F. Yang, Y. Jiang, T. Zhang, X.P. Wang, Q.F. Fang, C.S. Liu, J. Refract, Metal. Hard Mater. 81 (2019) 42–48.
[88] X.D. Yang, Z.M. Xie, S. Miao, X.P. Wang, C.S. Liu, Q.F. Fang, Fusion Des. Eng. 106 (2016) 56–62.
[89] Z.M. Xie, R. Liu, Q.F. Fang, Y. Zhou, X.P. Wang, C.S. Liu, J. Nucl. Mater. 444 (2014) 175–180.
[90] R. Liu, Z.M. Xie, T. Hao, Y. Zhou, X.P. Wang, Q.F. Fang, C.S. Liu, J. Nucl. Mater. 451 (2014) 35–39.
[91] M.M. Wang, Z.M. Xie, H.W. Deng, J.F. Yang, Y.K. Wang, T. Zhang, Y. Xiong, X.P. Wang, Q.F. Fang, C.S. Liu, Mater. Sci. Eng. A 754 (2019) 216–223.
[92] L. Romaner, C. Ambrosch-Draxl, R. Pippan,Phys. Rev. Lett. 104 (2010), 195503.
[93] S. Wurster, B. Gludovatz, R. Pippan, Int. J. Refract. Metal. Hard Mater. 28 (2010) 692–697.
[94] G.D. Samolyuk, Y.N. Osetskiy, R.E. Stoller,J. Phys. Condens. Matter 25 (2) (2012), 025403.
[95] W. Setyawan, R.J. Kurtz, Scripta Mater. 66 (2012) 558.

[96] R. Tran, Z. Xu, N. Zhou, B. Radhakrishnan, J. Luo, S.P. Ong, Acta Mater. 117 (2016) 91–99.
[97] T.D. Shen, S. Feng, M. Tang, J.A. Valdez, Y. Wang, K.E. Sickafus,Appl. Phys. Lett. 90 (2007), 263115.
[98] M. Samaras, P.M. Derlet, H. Van Swygenhoven, M. Victoria, Philos. Mag. 83 (2003) 3599.
[99] J. Schiotz, T. Leffers, B.N. Singh, Radiat. Eff. Defects Solids 157 (2002) 193–200.
[100] C. Sun, M. Song, K.Y. Yu, Y. Chen, M. Kirk, M. Li, H. Wang, X. Zhang, Metall. Mater. Trans. A 44 (2013) 1966–1974.
[101] X.M. Bai, A.F. Voter, R.G. Hoagland, M. Nastasi, B.P. Ulberuaga, Science 327 (2010) 1631.
[102] G. Federici, C.H. Skinner, J.N. Brooks, J.P. Coad, C. Grisolia, A.A. Haasz, A. Hassanein, V. Phlipps, C.S. Pitcher, J. Roth, W.R. Wampler, D.G. Whyte, Nucl. Fusion 41 (2001) 1967.
[103] K. Hattar, M.J. Demkowicz, A. Misra, I.M. Robertson, R.G. Hoagland, Scr. Mater. 58 (2008) 541–544.
[104] O. El-Atwani, J.A. Hinks, G. Greaves, S. Gonderman, T. Qiu, M. Efe, J.P. Allain, Sci. Rep. 4 (2014) 4716.
[105] Q. Wei, H.T. Zhang, B.E. Schuster, K.T. Ramesh, R.Z. Valiev, L.J. Kecskes, R.J. Dowding, L. Magness, K. Cho, Acta Mater. 54 (2006) 4079–4089.
[106] Q. Wei, T. Jiao, K.T. Ramesh, E. Ma, L.J. Kecskes, L. Magness, R. Dowding, U. Kazykhanov, R.Z. Valiev, Acta Mater. 54 (2006) 77–87.
[107] T. Hao, Z.Q. Fan, T. Zhang, G.N. Luo, X.P. Wang, C.S. Liu, Q.F. Fang, J. Nucl. Mater. 455 (2014) 595–599.
[108] Z.S. Levina, X.X. Wang, M. Kaynakc, I. Karamanc, K.T. Hartwig, Int. J. Refract. Metal. Hard Mater. 80 (2019) 73–84.
[109] Z.S. Levina, A. Srivastavab, D.C. Foleyc, K.T. Hartwig, Mater. Sci. Eng. A 734 (2018) 244–254.
[110] T. Chookajorn, H.A. Murdoch, C.A. Schuh, Science 337 (2012) 24.
[111] L. Ding, D.P. Xiang, Y.Y. Li, Y.W. Zhao, J.B. Li, Mater. Des. 37 (2012) 8–12.
[112] Z.B. Jiao, C.A. Schuh, Acta Mater. 161 (2018) 194.
[113] P. Li, Q. Lin, Y.F. Zhou, K.M. Xue, Y.C. Wu, Acta Metall. Sin. 55 (2019) 521.
[114] X. Zhou, X.Y. Li, K. Lu, Science 360 (2018) 526–530.
[115] H.Y. Guo, M. Xia, Z.T. Wu, L.C. Chan, Y. Dai, K. Wang, C.C. Ge, J. Lu, J. Nucl. Mater. 480 (2016) 281.
[116] Q. Wei, T. Jiao, K.T. Ramesh, E. Ma, Scripta Mater. 50 (2004) 359.
[117] H. Kurishita, S. Kobayashi, K. Nakai, H. Arakawa, S. Matuso, T. Takida, K. Takebe, M. Kawai, Phys. Scr. T128 (2007) 76–80.
[118] H. Kurishita, Y. Amano, S. Kobayashi, K. Nakai, H. Arakawa, Y. Hiraoka, T. Takida, K. Takebe, H. Matsui, J. Nucl. Mater. 367-370 (2007) 1453–1457.
[119] Y. Ueda, N. Ohno, S. Kajita, H. Kurishita, H. Iwakiri, K. Tokunaga, N. Yoshida, Fusion Sci. Technol. 52 (2007) 513–520.
[120] H. Kurishita, S. Matsuo, H. Arakawa, S. Kobayashi, K. Nakai, T. Takida, K. Takebe, M. Kawai, Mater. Sci. Eng. A 477 (2008) 162–167.
[121] T. Chookajorn, C.A. Schuh, Acta Mater. 73 (2014) 128–138.
[122] M. Park, C.A. Schuh, Nat. Commun. 6 (2015) 6858.
[123] Mansoo Park, Tongjai Chookajorn, Christopher A. Schuh, Acta Mater. 145 (2018) 123–133.
[124] R. Wang, Z.M. Xie, Y.K. Wang, J.P. Song, Q.F. Fang, R. Liu, J.F. Yang, T. Zhang, X.P. Wang, C.S. Liu, Int. J. Refract. Metal. Hard Mater. 80 (2019) 104–113.
[125] W.Q. Hu, Z. Dong, L.M. Yu, Z.Q. Ma, Y.C. Liu, J. Mater. Sci. Technol. 36 (2020) 84–90.
[126] R. Liu, X.P. Wang, T. Hao, C.S. Liu, Q.F. Fang, J. Nucl. Mater. 450 (2014) 69–74.
[127] C. Chen, Y. Zeng, J. Nucl. Mater. 469 (2016) 1–8.
[128] C.L. Chen, Y. Zeng, Int. J. Refract. Metal. Hard Mater. 56 (2016) 104–109.
[129] Z.M. Xie, R. Liu, S. Miao, T. Zhang, X.P. Wang, Q.F. Fang, C.S. Liu, G.N. Luo, J. Nucl. Mater. 464 (2015) 193–199.
[130] S. Sefta, K.D. Hammond, N. Juslin, B.D. Wirth,Nucl. Fusion 53 (2013), 073015.
[131] Z. Chen, L.L. Niu, Z.L. Wang, L.F. Tian, L. Kecskes, K.G. Zhu, Q.M. Wei, Acta Mater. 147 (2018) 100–112.
[132] O. El-Atwani, K. Hattar, J.A. Hinks, G. Greaves, S.S. Harilal, A. Hassanein, J. Nucl. Mater. 458 (2015) 216–223.
[133] W.Q. Wei, H.W. Wang, C.M. Zou, Z.J. Zhu, Z.J. Wei, Mater. Des. 46 (2013) 1–7.
[134] R.G. Ding, I.P. Jones, Mater. Sci. Technol. 26 (2010) 323–332.
[135] K.J. Leonard, J.C. Mishurda, V.K. Vasudevan, Metall. Mater. Trans. B 31 (2000) 1305–1320.
[136] K. Zelenitsas, P. Tsakiropoulos, Mater. Sci. Eng. A 416 (2006) 269–280.
[137] M. Fujikura, A. Kasama, R. Tanaka, S. Hanada, Mater. Trans. 45 (2004) 493–501.
[138] N.A. Mara, D. Bhattacharyya, P. Dickerson, R.G. Hoagland, A. Misra,Appl. Phys. Lett. 92 (2008), 231901.
[139] W.Z. Han, A. Misra, N.A. Mara, T.C. Germann, J.K. Baldwin, T. Shimada, S.N. Luo, Philos. Mag. 91 (2011) 4172–4185.
[140] S.J. Zheng, S. Shao, J. Zhang, Y.Q. Wang, M.J. Demkowicz, I.J. Beyerlein, N.A. Mara, Sci. Rep. 5 (2015) 15428.
[141] L.F. Zeng, R. Gao, Z.M. Xie, S. Miao, Q.F. Fang, X.P. Wang, T. Zhang, C.S. Liu, Sci. Rep. 7 (2017) 40742.
[142] N. Li, M. Demkowicz, N. Mara, Y.Q. Wang, A. Misra, Mater. Res. Lett. 4 (2016) 75–82.
[143] E.G. Fu, A. Misra, H. Wang, L. Shao, X. Zhang, J. Nucl. Mater. 407 (2010) 178–188.
[144] L.F. Zeng, P. Fan, L.F. Zhang, R. Gao, Z.M. Xie, Q.F. Fang, X.P. Wang, D.Q. Yuan, T. Zhang, C.S. Liu, J. Nucl. Mater. 508 (2018) 354–360.
[145] T. Höchbauer, A. Misra, K. Hattar, R.G. Hoagl, J. Appl. Phys. 98 (2005) 123516–123524.
[146] N. Li, J.J. Carter, A. Misra, L. Shao, H. Wang, X. Zhang, Philos. Mag. Lett. 91 (2011) 18–28.
[147] Q.M. Wei, N. Li, N. Mara, M. Nastasi, A. Misra, Acta Mater. 59 (2011) 6331–6340.
[148] H.X. Zhang, F. Ren, Y.Q. Wang, M.Q. Hong, X.H. Xiao, W.J. Qin, C.Z. Jiang, J. Nucl. Mater. 467 (2015) 537–543.
[149] Y.B. Kim, J.W. Baek, S.H. Kim, S.M. Kim, S.H. Ryu, S. Jeon, S.M. Han, Sci. Rep. 6 (2016) 24785.
[150] I.J. Beyerlein, J.R. Mayeur, S. Zheng, N.A. Mara, J. Wang, A. Misra, Proc. Natl. Acad. Sci. 111 (2014) 4386–4390.
[151] E.H. Ekiz, T.G. Lach, R.S. Averback, N.A. Mara, I.J. Beyerlein, M. Pouryazdan, H. Hahn, P. Bellon, Acta Mater. 72 (2014) 178.
[152] A. Misra, X. Zhang, M.J. Demkowicz, R.G. Hoagland, M. Nastasi, MRS Online Proceedings Library Archive, 1188, 2009.
[153] N.A. Mara, I.J. Beyerlein, J. Mater. Sci. 49 (2014) 6497–6516.
[154] N.A. Mara, I.J. Beyerlein, Curr. Opin. Solid State Mater. Sci. 19 (2015) 265–276.
[155] S. Ohsaki, S. Kato, N. Tsuji, T. Ohkubo, K. Hono, Acta Mater. 55 (2007) 2885.
[156] M.Z. Quadir, M. Ferry, O. Al-Buhamad, P.R. Munroe, Acta Mater. 57 (2009) 29–40.
[157] N.V. Govindaraj, J.G. Frydendahl, B. Holmedal, Mater. Des. 52 (2013) 905–915.
[158] S. Wurster, R. Pippan, Scripta Mater. 60 (2009) 1083–1087.
[159] B.V. Cockeram, Mater. Sci. Eng. A 418 (2006) 120–136.
[160] A.J. Mueller, J.A. Shields, R.W. Buckman Jr, in: G. Kneringer, P. Rodhammer, H. Wildner (Eds.), Proceedings of the 15th International Plansee Seminar, vol. 1, Plansee Holding AG, Reutte, Austria, 2001, pp. 485–497.
[161] P.M. Cheng, G.J. Zhang, J.Y. Zhang, G. Liu, J. Sun, Mater. Sci. Eng. A 640 (2015) 320–329.
[162] P.M. Cheng, Z.J. Zhang, G.J. Zhang, J.Y. Zhang, K. Wu, G. Liu, W. Fu, J. Sun, Mater. Sci. Eng. A 707 (2017) 295–305.
[163] A.J. Mueller, R. Bianco, R.W. Buckman, Int. J. Refract. Metals Hard Mater. 18 (2000) 205–211.
[164] G.J. Zhang, Y.J. Sun, R.M. Niu, J. Sun, J.F. Wei, B.H. Zhao, L.X. Yang, Adv. Eng. Mater. 6 (2004) 943–948.
[165] B.V. Cockeram, R.W. Smith, N. Hashimoto, L.L. Snead, J. Nucl. Mater. 418 (2011) 121–136.
[166] G. Liu, G.J. Zhang, F. Jiang, X.D. Ding, Y.J. Sun, J. Sun, E. Ma, Nat. Mater. 12 (2013) 344.
[167] H. Kurishita, S. Kobayashi, K. Nakai, T. Ogawa, A. Hasegawa, K. Abe, H. Arakawa, S. Matsuo, T. Takida, K. Takebe, M. Kawai, N. Yoshida, J. Nucl. Mater. 377 (2008) 34–40.
[168] M. Rieth, B. Dafferner, J. Nucl. Mater. 342 (2005) 20–25.
[169] L. Veleva, Z. Oksiuta, U. Vogt, N. Baluc, Fusion Eng. Des. 84 (2009) 1920–1924.
[170] M.A. Yar, S. Wahlberg, H. Bergqvis, H.G. Salem, M. Johnsson, M. Muhammed, J. Nucl. Mater. 408 (2011) 129–135.
[171] J.L. Fan, Y. Han, P.F. Li, Z.Y. Sun, Q. Zhou, J. Nucl. Mater. 455 (2014) 717–723.
[172] D. Lee, M.A. Umer, H.J. Ryu, S.H. Hong, Int. J. Refract. Met. Hard Mater. 44 (2014) 49–53.
[173] Y.K. Wang, S. Miao, Z.M. Xie, R. Liu, T. Zhang, Q.F. Fang, T. Hao, X.P. Wang, C.S. Liu, X. Liu, L.H. Cai, J. Nucl. Mater. 492 (2017) 260–268.
[174] Y.C. Wu, Q.Q. Hou, L.M. Luo, X. Zan, X.Y. Zhu, P. Li, Q. Xu, J.G. Cheng, G.N. Luo, J.L. Chen, J. Alloys Compd. 779 (2019) 926–941.
[175] M. Rieth, S.L. Dudarev, S.M.G. de Vicente, J. Aktaa, T. Ahlgren, S. Antusch, D.E.J. Armstrong, M. Balden, N. Baluc, M.F. Barthe, W.W. Basuki, M. Battabyal, C.S. Becquart, D. Blagoeva, H. Boldyryeva, J. Brinkmann, M. Celino, L. Ciupinski, J.B. Correia, A. De Backer, C. Domain, E. Gaganidze, C. García-Rosales, J. Gibson, M.R. Gilbert, S. Giusepponi, B. Gludovatz, H. Greuner, K. Heinola, T. Höschen, A. Hoffmann, N. Holstein, F. Koch, W. Krauss, H. Li, S. Lindig, J. Linke, Ch. Linsmeier, P. López-Ruiz, H. Maier, J. Matejicek, T.P. Mishra, M. Muhammed, A. Muñoz, M. Muzyk, K. Nordlund, D. Nguyen-Manh, J. Opschoor, N. Ordás, T. Palacios, G. Pintsuk, R. Pippan, J. Reiser, J. Riesch, S.G. Roberts, L. Romaner, M. Rosiński, M. Sanchez, W. Schulmeyer, H. Traxler, A. Ureña, J.G. van der Laan, L. Veleva, M. S.Wahlberg, T. Walter, T. Weber, S. Weitkamp, M.A. Wurster, J.H. Yar, A. You, J. Zivelonghi, Nucl. Mater. 432 (2013) 482–500.
[176] L. Veleva, in: International Conference on Genetic Algorithms, 2011, pp. 215–233.
[177] R. Liu, Y. Zhou, T. Hao, T. Zhang, X.P. Wang, C.S. Liu, Q.F. Fang, J. Nucl. Mater. 424 (2012) 171–175.
[178] M.Y. Zhao, Z.G. Zhou, M. Zhong, J. Tan, Y.Y. Lian, X. Liu, J. Nucl. Mater. 470 (2016) 236.
[179] Y.Y. Lian, X. Liu, F. Feng, J.P. Song, B.Y. Yan, Y.M. Wang, J.B. Wang, J.M. Chen,Phys. Scr. T170 (2017), 014044.
[180] M. Battabyal, R. Schblin, P. Spatig, M. Walter, N. Baluc, J. Nucl. Mater. 442 (2013) S225–S228.
[181] L. Veleva, R. Schaeublin, M. Battabyal, T. Plociski, N. Baluc, Int. J. Refract. Metals Hard Mater. 50 (2015) 210–216.
[182] M.V. Aguirre, A. Martin, J.Y. Pastor, J. Llorca, M.A. Monge, R. Pareja, Metall. Mater. Trans. A 40 (2009) 2283–2290.
[183] R. Liu, Z.M. Xie, Q.F. Fang, T. Zhang, X.P. Wang, T. Hao, C.S. Liu, Y. Dai, J. Alloys. Compd. 657 (2016) 73–80.
[184] X.Y. Ding, L.M. Luo, H.Y. Chen, X.Y. Zhu, X. Zan, J.G. Cheng, Y.C. Wu, Materials 9 (11) (2016) 879.
[185] M.L. Zhao, L.M. Luo, J.S. Lin, X.Y. Zhu, X. Zan, J.G. Cheng, Y.C. Wu, J. Nucl. Mater. 479 (2016) 616–662.

[186] Z. Dong, N. Liu, Z.Q. Ma, C.X. Liu, Q.Y. Guo, Y.S. Yamauchi, Int. J. Refract. Metals Hard Mater. 69 (2017) 266.
[187] M.A. Yar, S. Wahlberg, H. Bergqvist, H.G. Salem, M. Johnsson, M. Muhammed, J. Nucl. Mater. 412 (2011) 227–232.
[188] Z.M. Xie, R. Liu, Q.F. Fang, T. Zhang, Y. Jiang, X.P. Wang, C.S. Liu, Plasma Sci. Technol. 17 (2015) 1066–1071.
[189] Z.M. Xie, T. Zhang, R. Liu, Q.F. Fang, S. Miao, X.P. Wang, C.S. Liu, Int. J. Refract. Metal. Hard Mater. 51 (2015) 180–187.
[190] R. Liu, Z.M. Xie, X. Yao, T. Zhang, X.P. Wang, T. Hao, Q.F. Fang, C.S. Liu, Int. J. Refract. Metal. Hard Mater. 76 (2018) 33–40.
[191] J. Qian, C.Y. Wu, H.R. Gong, J. Alloys Compd. 768 (2018) 387–391.
[192] Y. Ishijima, S. Kannari, H. Kurishita, M. hasegawa, Y. Hiraoka, T. Takida, K. Takebe, Mater. Sci. Eng. A 473 (2008) 7–15.
[193] H.Y. Guo, M. Xia, L.C. Chan, K. Wang, X.X. Zhang, Q.Z. Yan, M.C. He, J. Lu, C.C. Ge, J. Nucl. Mater. 442 (2013) S233–S236.
[194] K. Lu, L. Lu, S. Suresh, Science 324 (2009) 349–352.
[195] X. Liu, Y.Y. Lian, H. Greuner, B. Boeswirth, Y.Z. Jin, F. Feng, J.B. Wang, L. Chen, J.P. Song, Y. Yu, T. Zhang, C.S. Liu, J. Tan, D.P. Liu, X.R. Duan, Nucl. Mater. Energy 12 (2017) 1314–1318.
[196] J. Zhang, S. Ma, J.W. Zhu, K.J. Kang, G.Q. Luo, C.D. Wu, Q. Shen, L.M. Zhang, Met. Mater. Int. 25 (2019) 416–424.
[197] K.J. Kang, R. Tu, G.Q. Luo, J. Zhang, J.W. Zhu, Q. Shen, L.M. Zhang, Int. J. Refract. Metal. Hard Mater. 75 (2018) 101–106.
[198] B. Huang, J. Tang, L.Q. Chen, X.L. Yang, Y.Y. Lian, L. Chen, X. Liu, X.D. Cui, L. Gu, C.T. Liu, J. Alloys Compd. 782 (2019) 149–159.
[199] J.J. Sha, X.N. Hao, J. Li, J.X. Dai, X.L. Yang, H.K. Yoon, J. Nucl. Mater. 455 (2014) 573–577.
[200] J.J. Sha, X.N. Hao, J. Li, Z. Wang, J. Alloys. Compd. 587 (2014) 290–295.
[201] J. Du, T. Höschen, M. Rasinski, S. Wurster, W. Grosinger, J.H. You, Compos. Sci. Tech. 70 (2010) 1482–1489.
[202] B. Jasper, J.W. Coenen, J. Riesch, T. Höschen, M. Bram, C. Linsmeier, Mater. Sci. Forum 825-826 (2015) 125–133.
[203] J. Riesch, J.Y. Buffière, T. Höschen, M. di Michiel, M. Scheel, Ch. Linsmeier, J.H. You, Acta Mater. 61 (2013) 7060–7071.
[204] J. Riesch, T. Höschen, J.H. You,Phys. Scr. T159 (2014), 014031.
[205] J.W. Coenen, S. Antusch, M. Aumann, W. Biel, J. Du, J. Engels, S. Heuer, A. Houben, T. Hoeschen, B. Jasper,Phys. Scr. T167 (2016), 014002.
[206] Y. Mao, J.W. Coenen, J. Riesch, S. Sistla, J. Almanstötter, B. Jasper, A. Terra, T. Höschen, H. Gietl, Ch. Linsmeier, C. Broeckmann, Comp. Part A 107 (2018) 342–353.
[207] Y. Jiang, L.H. Zhang, Q.F. Fang, T. Zhang, X.P. Wang, T. Hao, C.S. Liu, Mater. Sci. Eng. A 690 (2017) 208–213.
[208] J. Du, T. Hochen, M. Rasinski, J.H. You, J. Nucl. Mater. 417 (2011) 472–476.
[209] J. Riesch, Y. Han, J. Almanstötter, J.W. Coenen, T. Höschen, B. Jasper, P. Zhao, Ch. Linsmeier, R. Neu, Phys. Scr. T167 (2016) 014006–014014.
[210] J. Du, J.H. You, T. Hoschen, J. Mater. Sci. 47 (2012) 4706–4715.
[211] J. Riesch, J.Y. Buffiere, T. Höschena, M. Scheelc, Ch. Linsmeiere, J.H. You, Nucl. Mater. Energy 15 (2018) 1–12.
[212] M. Avello de Lama, M. Balden, H. Greuner, T. Höschen, J. Matejicek, J.H. You, Nucl. Mater. Energy 13 (2017) 74–80.
[213] J. Riesch, M. Aumann, J.W. Coenen, H. Gietl, G. Holzner, T. Höschen, P. Huber, M. Li, C. Linsmeier, R. Neu, Nucl. Mater. Energy 9 (2016) 75–83.
[214] Ch. Linsmeier, M. Rieth, J. Aktaa, T. Chikada, A. Hoffmann, J. Hoffmann, A. Houben, H. Kurishita, X. Jin, M. Li, A. Litnovsky, S. Matsuo, A. von Müller, V. Nikolic, T. Palacios, R. Pippan, D. Qu, J. Reiser, J. Riesch, T. Shikama, R. Stieglitz, T. Weber, S. Wurster, J.H. You, Z. Zhou,Nucl. Fusion 57 (2017), 092007.
[215] C. Hou, J. Wang, H. Wang, X. Liu, S. Liang, X. Song, Z. Nie, Int. J. Refract. Metal. Hard Mater. 77 (2018) 128–131.
[216] O.N. Senkov, G.B. Wilks, D.B. Miracle, C.P. Chuang, P.K. Liaw, Intermetallics 18 (2010) 1758–1765.
[217] O.N. Senkov, G.B. Wilks, J.M. Scott, D.B. Miracle, Intermetallics 19 (2011) 698–706.
[218] O.N. Senkov, J.M. Scott, S.V. Senkova, D.B. Miracle, C.F. Woodward, J. Alloys Compd. 509 (2011) 6043–6048.
[219] O.N. Senkov, J.M. Scott, S.V. Senkova, F. Meisenkothen, D.B. Miracle, C.F. Woodward, J. Mater. Sci. 47 (2012) 4062–4074.
[220] B. Schuh, B. Völker, J. Todt, N. Schell, L. Perrière, J. Lie, J.P. Couzinié, A. Hohenwarter, Acta Mater. 142 (2018) 201–212.